

# **Optical Fiber Sensor Technologies for Efficient and Economical Oil Recovery**

## **Final Technical Report**

Reporting Period Start Date: 1 October 1998

Reporting Period End Date: 31 March 2003

Principal Investigator: Anbo Wang

Principal Report Authors: Kristie L. Cooper, Gary R. Pickrell, Anbo Wang

Report Issued: June 2003

DOE Award Number: DE-FT26-98BC15167

Submitted by: Center for Photonics Technology  
Bradley Department of Electrical and Computer Engineering  
Virginia Polytechnic Institute & State University  
Blacksburg, VA 24061-0111



Disclaimer:

This report was prepared as an account of work sponsored by an agency of the United States Government. Neither the United States Government nor any agency thereof, nor any of their employees, makes any warranty, express or implied, or assumes any legal liability or responsibility for the accuracy, completeness, or usefulness of any information, apparatus, product, or process disclosed, or represents that its use would not infringe privately owned rights. Reference herein to any specific commercial product, process, or service by trade name, trademark, manufacturer, or otherwise does not necessarily constitute or imply its endorsement, recommendation, or favoring by the United States Government or any agency thereof. The views and opinions of authors expressed herein do not necessarily state or reflect those of the United States Government or any agency thereof.

## **Abstract**

Efficient recovery of petroleum reserves from existing oil wells has been proven to be difficult due to the lack of robust instrumentation that can accurately and reliably monitor processes in the downhole environment. Commercially available sensors for measurement of pressure, temperature, and fluid flow exhibit shortened lifetimes in the harsh downhole conditions, which are characterized by high pressures (up to 20 kpsi), temperatures up to 250°C, and exposure to chemically reactive fluids. Development of robust sensors that deliver continuous, real-time data on reservoir performance and petroleum flow pathways will facilitate application of advanced recovery technologies, including horizontal and multi-lateral wells.

This is the final report for the four-year program “Optical Fiber Sensor Technologies for Efficient and Economical Oil Recovery”, funded by the National Petroleum Technology Office of the U.S. Department of Energy, and performed by the Center for Photonics Technology of the Bradley Department of Electrical and Computer Engineering at Virginia Tech from October 1, 1999 to March 31, 2003. The main objective of this research program was to develop cost-effective, reliable optical fiber sensor instrumentation for real-time monitoring of various key parameters crucial to efficient and economical oil production.

During the program, optical fiber sensors were demonstrated for the measurement of temperature, pressure, flow, and acoustic waves, including three successful field tests in the Chevron/Texaco oil fields in Coalinga, California, and at the world-class oil flow simulation facilities in Tulsa, Oklahoma. Research efforts included the design and fabrication of sensor probes, development of signal processing algorithms, construction of test systems, development and testing of strategies for the protection of optical fibers and sensors in the downhole environment, development of remote monitoring capabilities allowing real-time monitoring of the field test data from virtually anywhere in the world, and development of novel data processing techniques. Comprehensive testing was performed to systematically evaluate the performance of the fiber optic sensor systems in both lab and field environments.

# Table of Contents

Abstract.....	iii
Table of Contents .....	iv
List of Figures.....	viii
List of Tables .....	xii
Executive Summary .....	1
1.0 Introduction .....	3
2.0 Background.....	4
3.0 Specification of Technical Requirements .....	6

## EXPERIMENTAL RESULTS AND DISCUSSION

4.0 SCIIB Sensor System Overview .....	7
4.1 Principle of Operation.....	7
4.1.1 <i>Optimal Cavity Length</i> .....	9
4.1.2 <i>Linear Operating Range</i> .....	13
4.2 SCIIB Advantages.....	14
4.3 Multimode Sensor.....	15
4.4 Singlemode Sensor.....	17
4.5 Preliminary Sensor Testing.....	19
4.5.1 <i>Fiber loss compensation</i> .....	19
4.5.2 <i>Compensation for bending-induced spectral changes</i> .....	22
5.0 Instrumentation Systems .....	25
5.1 Signal Demodulation System I – SCIIB .....	25
5.1.1 <i>Design and implementation</i> .....	25
5.1.2 <i>SCIIB System Noise Analysis</i> .....	27
5.1.3 <i>Other Proposed Signal Demodulating Structures</i> .....	59
5.2 Signal Demodulation System II – White Light Interferometer.....	60
5.2.1 <i>Principle of operation</i> .....	60
5.2.2 <i>Novel data processing method</i> .....	62
5.2.3 <i>Design and implementation</i> .....	65
5.2.4 <i>Software design and program development</i> .....	65
5.2.5 <i>White light system performance</i> .....	75
5.3 Comparison Between the SCIIB System and the White Light System.....	80
5.3.1 <i>Dynamic range</i> .....	80
5.3.2 <i>Insensitivity to the change of the polarization status</i> .....	81
5.3.3 <i>Demands on the Geometrical Parameters of the FABRY-PEROT Sensor</i> .....	82
6.0 Automated Sensor Fabrication System .....	83
6.1 System Configuration .....	84
6.2 CO <sub>2</sub> Laser Sub-System.....	84
6.3 CO <sub>2</sub> Laser Sub-System.....	85

6.3.1	<i>Mechanical strength improvements</i> .....	86
6.4	White Light Fiber Optic Interferometer Sub-System.....	87
6.4.1	<i>Principle of white light interferometric air gap monitoring</i> .....	87
6.4.2	<i>Implementation of multimode and singlemode white light subsystems</i> .....	88
6.4.3	<i>Software design of white light sub-system</i> .....	91
6.5	Micropositioning Subsystem.....	93
6.6	System Testing Results .....	94
6.6.1	<i>White light subsystem performance test and results</i> .....	94
6.6.2	<i>CO<sub>2</sub> laser power calibration</i> .....	95
6.6.3	<i>PZT Stage calibration</i> .....	95
6.7	Fabrication Procedure Optimization .....	97
6.7.1	<i>CO<sub>2</sub> laser power and exposure time optimization</i> .....	97
6.7.2	<i>SCIIB sensor fabrication and results</i> .....	97
6.7.3	<i>Repeatability improvements</i> .....	98
6.8	Performance of Fabricated Sensors.....	98
6.8.1	<i>Survivability of the sensor probe</i> .....	99
6.8.2	<i>SCIIB sensor annealing</i> .....	99
6.8.3	<i>Temperature dependence of the SCIIB sensor probe</i> .....	100
<b>7.0</b>	<b>Pressure Sensors .....</b>	<b>104</b>
7.1	Pressure Sensor Design.....	104
7.2	Pressure Sensor Fabrication .....	106
7.2.1	<i>Singlemode fiber sensor</i> .....	106
7.2.2	<i>Multimode fiber sensor</i> .....	106
7.3	Carbon Coated Multimode-Singlemode Combo Fiber Sensor .....	108
7.3.1	<i>Leakage prevention</i> .....	108
7.3.2	<i>Temperature sensitivity reduction</i> .....	109
7.3.3	<i>Precise air gap control</i> .....	109
7.3.4	<i>Gauge length</i> .....	110
7.3.5	<i>Elimination of nonlinearity</i> .....	111
7.3.6	<i>System construction</i> .....	111
7.3.7	<i>Calibration procedures</i> .....	113
7.4	Experimental Results .....	115
7.4.1	<i>SCIIB pressure sensors</i> .....	115
7.4.2	<i>Multimode white light pressure sensors</i> .....	122
<b>8.0</b>	<b>Temperature Sensors .....</b>	<b>126</b>
8.1	Temperature Sensor Design .....	126
8.2	Temperature Sensor Fabrication .....	127
8.3	Pressure Cross-Sensitivity.....	128
8.4	Temperature Sensor Testing Results.....	129
8.4.1	<i>SCIIB thermal stability</i> .....	129
8.4.2	<i>SCIIB differential coefficient of thermal expansion (<math>\Delta CTE</math>)</i> .....	129
8.4.3	<i>SCIIB standard deviation</i> .....	130
8.4.4	<i>White light interferometer temperature sensor</i> .....	130
<b>9.0</b>	<b>Flow Sensors.....</b>	<b>133</b>
9.1	Flow Sensor Design .....	133
9.2	Flow Sensor Construction.....	137
9.3	Lab-Scale Experiments and Results.....	137
9.3.1	<i>Sensor calibration</i> .....	139

9.3.2	<i>Temperature compensation</i> .....	141
9.3.3	<i>Measurement results</i> .....	141
9.3.4	<i>Repeatability</i> .....	141
9.3.5	<i>Dynamic flow measurements</i> .....	142
9.3.6	<i>Resolution of flow rate measurement</i> .....	142
9.3.7	<i>Hysteresis of flow rate measurement</i> .....	142
9.3.8	<i>System stability test</i> .....	146
<b>10.0</b>	<b>Acoustic Sensors .....</b>	<b>147</b>
10.1	Principle of Operation.....	147
10.2	Sensor Frequency Response and Sensitivity Design .....	148
10.3	Acoustic Sensor Fabrication .....	151
10.3.1	<i>Epoxy-based sensor fabrication</i> .....	151
10.3.2	<i>Direct thermal bonding method</i> .....	152
10.3.3	<i>Intermediate layer thermal bonding</i> .....	153
10.4	Acoustic Testing System.....	154
10.5	Experimental Results .....	154
<b>11.0</b>	<b>Sensor Packaging Methods.....</b>	<b>157</b>
11.1	Packaging Requirements.....	157
11.2	Determination of Minimum Bend Radius.....	157
11.2.1	<i>Procedure for Minimum Bend Radius Testing</i> .....	158
11.2.2	<i>Minimum Bend Radius Results</i> .....	159
11.3	Water Effects at Elevated Temperature and Pressure .....	164
11.3.1	<i>Experimental Procedure for Fiber Testing in Water at Elevated Temperature and Pressure</i> .....	165
11.3.2	<i>Experimental Results – Optical Fiber Performance in Water at Elevated Temperature and Pressure</i> .....	165
11.4	Carbon-Coated Fiber Development .....	167
11.5	Gold-Coated Fiber.....	167
11.6	Encapsulated Fiber.....	177
11.6.1	<i>Structure of the fiber sensor protection package:</i> .....	177
11.6.2	<i>Packaging process</i> .....	178
<b>12.0</b>	<b>Field Testing of Flow Sensor System .....</b>	<b>179</b>
12.1	Indoor Flow Testing.....	179
12.1.1	<i>Variable frequency pump calibration</i> .....	181
12.1.2	<i>Sensor calibration</i> .....	181
12.1.3	<i>Measurement results and repeatability</i> .....	181
12.1.4	<i>Resolution of indoor flow testing</i> .....	182
12.1.5	<i>Hysteresis of flow sensor</i> .....	183
12.1.6	<i>Stability testing</i> .....	185
12.2	Outdoor Flow Loop Testing System and Results .....	186
12.2.1	<i>Calibration</i> .....	188
12.2.2	<i>Stability</i> .....	190
12.2.3	<i>Resolution</i> .....	190
12.2.4	<i>Repeatability</i> .....	191
12.2.5	<i>Hysteresis</i> .....	191
<b>13.0</b>	<b>Temperature and Pressure Sensor Field Testing .....</b>	<b>195</b>
13.1	First Coalinga Field Test.....	195

13.1.1 <i>Sensor deployment</i> .....	195
13.1.2 <i>Remote access and control</i> .....	195
13.1.3 <i>Long-term stability</i> .....	198
13.2 Second Coalinga Field Test .....	198

**CONCLUSIONS**

<b>14.0 Summary and Conclusions .....</b>	<b>201</b>
<b>References .....</b>	<b>203</b>
<b>List of Acronyms and Abbreviations .....</b>	<b>204</b>

## List of Figures

Figure 4.1. Illustration of the principle of SCIIB fiber optic sensor system.....	7
Figure 4.2. Illustration of the two channel outputs of the SCIIB sensor.....	8
Figure 4.3. Interference fringes of the two SCIIB channels for a source spectral width of 40nm and center wavelength of 1310nm, and a bandpass filter spectral width of 10nm, corresponding to the singlemode fiber sensor system. ....	11
Figure 4.4. Ratio of the two channel outputs shown in Figure 4.3. ....	11
Figure 4.5. Interference fringes of the two SCIIB channels for a source spectral width of 70nm and center wavelength of 850nm, and a bandpass filter spectral width of 10nm, corresponding to the multimode fiber sensor system. ....	12
Figure 4.6. Ratio of the two channel outputs shown in Figure 4.5. ....	12
Figure 4.7. Illustration of a semi-linear fringe operating range. ....	14
Figure 4.8. Multimode SCIIB sensor system, schematic (top) and photograph (bottom). ....	16
Figure 4.9. Optical spectrum of the source LED for the multimode SCIIB system (center wavelength 850 nm, spectral width 70 nm, and typical output power 120 $\mu$ W). ....	17
Figure 4.10. Singlemode SCIIB sensor system, schematic (top) and photograph (bottom). ....	18
Figure 4.11. Optical spectrum of the SLED source measured by an Ando OSA (center wavelength 1312 nm, spectral width 41.5 nm, output power 1.21mW from a 9/125 $\mu$ m pigtailed single-mode fiber). ....	19
Figure 4.12. Multimode SCIIB sensor output compensated for fiber bending loss.....	20
Figure 4.13. SCIIB output versus driving current of the optical source. ....	21
Figure 4.14. Change in SCIIB output ratio versus the normalized source power change. ....	21
Figure 4.15. Experimental setup used to evaluate for fiber bending induced spectral changes. ....	22
Figure 4.16. Bending induced spectral changes in standard singlemode telecommunications fiber. ....	23
Figure 4.17. Bending induced spectral changes in bend insensitive singlemode fiber. ....	24
Figure 5.1. DSP based SCIIB high speed sensor system. ....	25
Figure 5.2. Current-power curve of the HEF4856 LED. ....	26
Figure 5.3. Noise equivalent circuit of the transimpedance amplifier. ....	30
Figure 5.4. Normalized error induced by the wavelength drift of the filter. ....	34
Figure 5.5. Schematic illustration of non-centered filtering. ....	35
Figure 5.6. Normalized measurement error resulting from the residual interference in the reference channel and the noncentered filtering, where the initial sensor cavity length is set to be $L_0=25\mu\text{m}$ . ....	37
Figure 5.7. Bending induced spectral changes in standard telecommunications singlemode fiber. ....	38
Figure 5.8. Bending induced spectral changes in bending insensitive singlemode fiber. ....	38
Figure 5.9. Beam splitter transmission characteristics. ....	40
Figure 5.10. Both SCIIB channel outputs as SOP of the fiber changes (without the depolarizer). ....	43
Figure 5.11. Ratio of the two SCIIB channel outputs as SOP of the fiber changes (without the depolarizer). ....	43
Figure 5.12. SCIIB channel outputs as SOP of the fiber changes (with the depolarizer). ....	44
Figure 5.13. Ratio of the two SCIIB channel outputs as SOP of the fiber changes (with the depolarizer). ....	44
Figure 5.14. Normalized measurement error resulting from the dark current bias. ....	46
Figure 5.15. Experimental setup for SCIIB thermal testing. ....	47
Figure 5.16. Reference channel signal transmitting path. ....	48
Figure 5.17. Output spectrum of the SLED (Ando OSA). ....	49
Figure 5.18. Schematic of the preamplifier. ....	50
Figure 5.19. Temperature dependence of the reference channel. ....	51
Figure 5.20. Temperature dependence of the signal channel. ....	51
Figure 5.21. Temperature dependence of the SCIIB ratio (signal channel / reference channel). ....	52
Figure 5.22. Experimental setup to investigate the use of an optical switch to reduce the spectrum independent temperature dependence of the SCIIB system. ....	52
Figure 5.23. Optical switch experimental results (Green line— $R_1$ ; Blue line— $R_2$ ; Red line— $R$ ). ....	54
Figure 5.24. Light spectrum reflected from a Fabry-Perot sensor (Red line, the initial air gap of the sensor head is 12000nm); blue line, that from a polished fiber endface).....	55
Figure 5.25. Experimental results from the FABRY-PEROT sensor (Green line—Sensor Path $R_1$ ; Blue line—Reference Path $R_2$ ; Red line— $R=R_1/R_2$ ). ....	56

Figure 5.26. SCIIB system temperature experiment (The X axis is time; The unit of the output from thermal resistor is volts).....	57
Figure 5.27. Temperature dependence of the ratio R.....	58
Figure 5.28. Calibration curve of the sensor head.....	58
Figure 5.29. Proposed dual-sensor structure design.....	59
Figure 5.30. Basic structure of interferometer-based white light system.....	61
Figure 5.31. Two channel multimode white light system.....	66
Figure 5.32. Single channel multimode white light system.....	67
Figure 5.33. Block diagram of demodulation program.....	68
Figure 5.34. The interference spectrum after pre-processing.....	70
Figure 5.35. The interference spectrum after smoothing.....	70
Figure 5.36. Normalized interference spectrum.....	71
Figure 5.37. Simulated result for small window width ( $w=5$ ).....	72
Figure 5.38. Simulated result for large window width ( $w=80$ ).....	73
Figure 5.39. Measured result when a large window width was used.....	73
Figure 5.40. The mass-centroid method.....	74
Figure 5.41. Testing results from the FABRY-PEROT temperature sensor.....	75
Figure 5.42. Short term fluctuation of the white light system.....	76
Figure 5.43 Simulated normalized spectrum.....	78
Figure 5.44. Measurement results of the normalized spectrum at 45°C.....	78
Figure 5.45. Relationship between center wavelength of the LED and temperature.....	79
Figure 6.1. Schematic of the automated sensor fabrication system.....	84
Figure 6.2. Automated SCIIB sensor fabrication system.....	85
Figure 6.3. Block diagram of the CO <sub>2</sub> laser control subsystem.....	86
Figure 6.4. Schematic of the copper mirror set in sensor fabrication system.....	86
Figure 6.5. Basic principle of the white light interferometric air gap monitoring system.....	87
Figure 6.6. Configuration of the multimode white light air gap monitoring system.....	89
Figure 6.7. Picture of the multimode white light air gap monitoring system.....	89
Figure 6.8. Configuration of the singlemode white light air gap monitoring system.....	90
Figure 6.9. Picture of the singlemode white light air gap monitoring system.....	90
Figure 6.10. Block diagram of air gap monitoring software.....	91
Figure 6.11. White light air gap monitoring software under operation.....	92
Figure 6.12. Computer controlled micro-motion fiber and tube positioning system.....	93
Figure 6.13. Micropositioning stage system.....	94
Figure 6.14. CO <sub>2</sub> laser output power calibration results.....	96
Figure 6.15. PZT stage movement calibration results.....	96
Figure 6.16. CO <sub>2</sub> laser power level and exposure time.....	97
Figure 6.17. Micrograph of the SCIIB sensor probe (Gauge length: 1.5mm, initial cavity length: 25.74μm).....	99
Figure 6.18. Multimode SCIIB sensor temperature sensitivity test result.....	101
Figure 6.19 Temperature sensitivity test results of singlemode sensor probes.....	102
Figure 7.1. Geometry of SCIIB pressure sensor head.....	104
Figure 7.2. Relationship between the sensor geometric parameters and the maximum pressure.....	105
Figure 7.3. Singlemode white light monitoring window.....	107
Figure 7.4. Multimode white light monitoring window.....	107
Figure 7.5. Schematic of carbon-coated fiber.....	108
Figure 7.6. Polyimide removal from carbon-coated fiber using a blade.....	108
Figure 7.7. Schematic of three-point bonding.....	109
Figure 7.8. Combo structure sensor head to reduce temperature sensitivity.....	109
Figure 7.9. Air gap control by laser bonding power.....	110
Figure 7.10. APP pressure sensor test system.....	112
Figure 7.11. PSI 9035 based high accuracy pressure testing system configuration.....	113
Figure 7.12. Applied pressure recorded during sensor calibration.....	114
Figure 7.13. SCIIB output ratio recorded during sensor calibration.....	114
Figure 7.14. SCIIB pressure sensor calibration curve.....	115
Figure 7.15. SCIIB pressure sensor system calibration lines.....	116
Figure 7.16. Nonlinearity of the SCIIB pressure sensor system.....	116

Figure 7.17. Hysteresis of the SCIIB pressure sensor. ....	117
Figure 7.18. Standard deviation measurement of the SCIIB pressure sensor. ....	118
Figure 7.19. Repeatability of the pressure measurement. ....	118
Figure 7.20. Deviation of the measured pressure with respect to the calibration data. ....	119
Figure 7.21. System stability over 24 hours. ....	119
Figure 7.22. Temperature cross sensitivity of the SCIIB pressure sensor. ....	120
Figure 7.23. Pressure measurement errors resulting from the temperature dependence. ....	121
Figure 7.24. Overpressure test results of the multimode SCIIB sensor. ....	121
Figure 7.25. Sensor deviation of the overpressure tests. ....	122
Figure 7.26. Dynamic pressure measurement results for the multimode sensor. ....	123
Figure 7.27. Dynamic pressure measurement results for the singlemode sensor. ....	123
Figure 7.28. Testing results of a pressure sensor under different temperatures. ....	124
Figure 7.29. Resolution of pressure system. ....	124
Figure 7.30. 48-hour stability testing of the pressure sensor. ....	125
Figure 8.1. Geometry of FABRY-PEROT temperature sensor. ....	126
Figure 8.2. Relationship between sensor gauge length and temperature measurement range. ....	127
Figure 8.3. Pressure isolating tube of the temperature sensor. ....	128
Figure 8.4. SCIIB temperature sensor survivability and stability test results. ....	129
Figure 8.5. Test result used to calculate the $\Delta$ CTE of the SCIIB sensor. ....	130
Figure 8.6. SCIIB temperature sensor standard deviation test results. ....	131
Figure 8.7. Calibration curve of white light temperature sensor. ....	131
Figure 8.8. Hysteresis effect in temperature measurement. ....	132
Figure 9.1. Fiber optic flow sensor system. ....	134
Figure 9.2. Simulation of flow sensor self-compensation. ....	136
Figure 9.3. Fabrication of flow sensor. ....	138
Figure 9.4. Lab-scale flow testing system setup. ....	138
Figure 9.5. Flow sensor testing setup in Center for Photonics Technology, Virginia Tech. ....	139
Figure 9.6. Relationship between flow rate and flow sensor air gaps. ....	140
Figure 9.7. Flow sensor calibration curve. ....	140
Figure 9.8. Fiber optic flow sensor self-compensation result. ....	141
Figure 9.9. Flow sensor system calibration lines. ....	142
Figure 9.10. Flow measurement repeatability test results. ....	143
Figure 9.11. Dynamic response of flow sensor. ....	144
Figure 9.12. Resolution of flow sensor system. ....	144
Figure 9.13. Hysteresis of flow sensor in lab-scale testing. ....	145
Figure 9.14. Flow sensor system stability test over 12 hours at 7.2 GPM. ....	146
Figure 10.1. Illustration of the principle of the diaphragm-based fiber optic acoustic sensor. ....	147
Figure 10.2. Illustration of a linear operating range of the sensor response curve. ....	148
Figure 10.3. Structure model for diaphragm-based acoustic sensor. ....	149
Figure 10.4. Predicted frequency response of the sensor at $R=1$ mm. ....	150
Figure 10.5. Theoretical sensor response ( $\mu$ m/ psi) versus diaphragm thickness at $R=1$ mm. ....	151
Figure 10.6. Direct thermal bonding diaphragm-based acoustic sensor fabrication system. ....	152
Figure 10.7. Acoustic sensor fabrication system using intermediate layer bonding method. ....	153
Figure 10.8. Photograph of acoustic testing system. ....	154
Figure 10.9. Acoustic sensor testing system configuration. ....	155
Figure 10.10. Pressure sensitivity of fiber optical acoustic sensor. ....	155
Figure 10.11. Comparison of acoustic signal from acoustic actuator (yellow) and acoustic sensor (green). The bottom graph is an enlargement of the acoustic signal from the LeCroy 505 oscilloscope. ....	156
Figure 11.1. Apparatus used for minimum bend radius and time to failure testing. ....	158
Figure 11.2. Minimum bend diameter versus exposure time at 200°C. ....	159
Figure 11.3. Time to failure versus bend diameter for Corning SMF. ....	161
Figure 11.4. Time to failure versus bend diameter. ....	161
Figure 11.5. Time to failure versus reciprocal stress for Corning SMF. ....	162
Figure 11.6. Average time to failure for optical fiber versus bend diameter. ....	162
Figure 11.7. Time to failure versus time after exposure. ....	163
Figure 11.8. Calculated minimum bend radius versus coating thickness for various coating materials. ....	164

Figure 11.9. OH absorption versus time for fibers immersed in water at 200°C.....	166
Figure 11.10. SEM micrograph of the fracture surface of an optical fiber coated with carbon by laser ablation .....	168
Figure 11.11. Results of stability testing of signal processing system – gold coated sensor held at 205°C. ....	168
Figure 11.12. Measured pressure versus applied pressure as a function of exposure time for an uncoated sensor. .....	169
Figure 11.13. Measured pressure versus applied pressure as a function of exposure time for an uncoated sensor (continued). ....	170
Figure 11.14. Measured pressure versus applied pressure as a function of exposure time for an gold coated sensor. ....	170
Figure 11.15. Measured pressure versus applied pressure as a function of exposure time for a gold-coated sensor. ....	171
Figure 11.16. Pressure calibration difference between first and following days versus date for a gold coated and an uncoated sensor. ....	172
Figure 11.17. Measured pressure versus applied pressure as a function of exposure time for an uncoated sensor .....	172
Figure 11.18. Measured pressure versus applied pressure as a function of exposure time for an uncoated sensor (continued). ....	173
Figure 11.19. Measured pressure versus applied pressure as a function of exposure time for an uncoated sensor. .....	173
Figure 11.20. Measured pressure versus applied pressure as a function of exposure time for an uncoated sensor (continued). ....	174
Figure 11.21. Pressure calibration difference between first and following days versus date for a gold coated and an uncoated sensor. ....	174
Figure 11.22. SCIIB output versus applied pressure and as a function of different fiber pigtail polarization states.....	175
Figure 11.23. Effect of fusion splice loss on the SCIIB output. ....	175
Figure 11.24. SCIIB output versus applied pressure and as a function of different fiber pigtail polarization states for improved system.....	176
Figure 11.25. Effect of fusion splice loss on the SCIIB output for improved system. ....	176
Figure 11.26. Schematic of the protection packaging assembly.....	177
Figure 12.1. Indoor flow testing system in University of Tulsa , OK. ....	180
Figure 12.2. Variable frequency pump calibration curve using FT-24NENW flow meter.....	181
Figure 12.3. Flow sensor calibration curve for indoor flow testing in Tulsa, OK. ....	182
Figure 12.4. Resolution of flow sensor system, indoor flow testing. ....	182
Figure 12.5. Measurement results from fiber flow sensor in indoor testing loop. ....	183
Figure 12.6. Flow sensor hysteresis measurement. ....	184
Figure 12.7. Flow system stability test over approximately 2 hours. ....	185
Figure 12.8. Outdoor flow testing facility in Tulsa University, OK.....	187
Figure 12.9. Fiber optic flow sensor deployment in outdoor flow loops of Tulsa University, OK. ....	188
Figure 12.10. Fiber optic flow sensor control system for outdoor flow testing. ....	188
Figure 12.11. Flow sensor calibration for outdoor flow testing. ....	189
Figure 12.12. Flow sensor stability during outdoor flow testing. ....	190
Figure 12.13. Resolution of fiber flow sensor during outdoor flow testing.....	191
Figure 12.14. Measurement results and repeatability testing in outdoor flow testing. ....	192
Figure 12.15. Hysteresis testing in outdoor flow testing. ....	193
Figure 13.1. Nortel Extranet Access Client Software. ....	196
Figure 13.2. pcAnywhere Manager Window. ....	197
Figure 13.3. Pressure Measurement Window.....	197
Figure 13.4. Ninety day testing result in oil site.....	199
Figure 13.5. Pressure sensor output from 6/3/2002 - 10/31/2002.....	199
Figure 13.6. Temperature sensor output from 8/7/2002 – 10/31/2002.....	200

## List of Tables

Table 3-1. Initial sensor specifications. ....	6
Table 5.1. Optical loss mechanisms in singlemode fiber SCIIB system. ....	31
Table 5.2. SNR calculation of the singlemode fiber SCIIB electronics ....	32
Table 5.3. Typical electronic and optical noise for the SCIIB sensor system. ....	41
Table 5.4. Key features of the Ocean Optics USB2000 fiber spectrometer. ....	66
Table 6.1. Sensor cavity length change before and after annealing. ....	100
Table 9.1. Parameters of fiber optic flow sensor used for lab scale testing. ....	139
Table 12.1. Parameters of fiber optic flow sensor used for indoor flow testing in Tulsa. ....	179
Table 12.2. Fiber optic flow sensor parameters for outdoor flow testing in Tulsa, OK. ....	186
Table 12.3 Summary of the performance evaluation results for fiber optic sensor systems. ....	194

## Executive Summary

This report summarizes the successful achievements during the four and a half-year program “Optical Fiber Sensor Technologies for Efficient and Economical Oil Recovery”, funded by the National Petroleum Technology Office of the U.S. Department of Energy, and performed by the Center for Photonics Technology (CPT) of the Bradley Department of Electrical and Computer Engineering at Virginia Tech. The objective was the development and demonstration of cost-effective, reliable optical fiber sensors for the measurement of temperature, pressure, flow, and acoustic waves in downhole environments. Sensors were successfully demonstrated for the measurement of all four target parameters, including three successful field tests in the Chevron/Texaco oil fields in Coalinga, California and at the world class oil flow loop facility in Tulsa, Oklahoma.

In the first program year, solid research progress was made in specification of the technical requirements, design and fabrication of the SCIIB sensor probes, development of the sensor systems, development of DSP-based signal processing techniques, and construction of the test systems.

During the second year, research efforts were directed towards improvement of the fabrication processes for SCIIB sensors, evaluation and improvement of the performance of the SCIIB optoelectronic signal conditioning system, and development and testing of strategies for the protection of optical fibers and sensors in the downhole environment.

Building upon the demonstrated success in the first two years, the sensor system performance was improved dramatically during the third year:

- By selecting suitable materials for the glass tube and optical fiber, the cross-sensitivity of the pressure and temperature sensors was minimized.
- A metal foil based sensor packaging technique was developed for both mechanical protection and a waterproof isolation medium.
- Most of the important noise sources in the SCIIB signal demodulation system were analyzed and identified by both theoretical analysis and experiment. Several compensating structures were designed which improved the system stability.
- To satisfy the strict performance requirements for the pressure and temperature sensors, a spectrometer based white light signal demodulation system was developed. By using a novel data processing method invented at CPT, the stability of this system is better than 0.5psi with a 6000psi dynamic range. The resolution of the white light system has been shown to be 0.03nm corresponding to 0.03 psi for the pressure sensor system.
- During the first field test, the sensor was successfully deployed using Chevron’s hydraulic deployment method into a test well in Coalinga, California, the remote data access through internet was realized allowing real-time data monitoring from virtually anywhere in the world and the long-term stability of the sensor head in downhole environment verified.

During the fourth year, research efforts were focused on the development and evaluation of the fiber optic flow sensor system, flow sensor field testing in Tulsa, OK and the second, more extensive, field testing of the pressure and temperature sensors in Coalinga, CA.

- The feasibility of a self-compensating fiber optic flow sensor based on a cantilever beam and interferometer for real-time flow rate measurements in the fluid filled pipes of oil field was clearly demonstrated.
- Prototype flow sensors were fabricated based on the fabrication experience of hundreds of test sensors.
- A lab-scale flow testing system was constructed and used for prototype sensor evaluation.
- Field-testing was performed in both the indoor and outdoor flow testing facility at the University of Tulsa, OK.
- Testing of a white light pressure and temperature sensor system continued in the oil fields of the Chevron/Texaco Company in Coalinga CA

## 1.0 Introduction

This is the final report for the Virginia Tech Center for Photonics Technology (VTCPT) research project “Optical Fiber Sensor Technologies for Efficient and Economical Oil Recovery.” The main objective for this four and one-half year program has been the development and demonstration of cost-effective, reliable optical fiber sensors for the measurement of temperature, pressure, flow, and acoustic waves in downhole environments for use in oil recovery.

The sensors developed under this program are based on the Self-Calibrated Interferometric/Intensity-Based (SCIIB) and white light interferometer fiber optic sensor configurations invented at the Center for Photonics Technology. The SCIIB design measures displacement (elongation or contraction) of a small Fabry-Perot interferometer cavity constructed in an optical fiber. The Fabry-Perot assembly is typically cylindrical, and generally has dimensions on the order of 0.1 mm in diameter and 5 mm long. By proper mechanical design of the assembly, physical parameters such as pressure, temperature, flow, and acoustic waves can be made to induce a displacement in the Fabry-Perot assembly, which may then be measured by the SCIIB system. In the SCIIB configuration, the Fabry-Perot assembly is designed so that the output of the cavity over the sensor’s dynamic range is limited to the quasi-linear region of the interference signal output of the cavity. In this way, interpretation of the nonlinear output of typical interferometers is avoided, simplifying the signal processing.

The SCIIB system uses optical filtering to process the optical signal output so that two signals are produced: one which contains information about the cavity displacement, and another that contains information regarding undesired effects in the first signal, such as fluctuations in the optical source power, or changes in optical fiber loss. The second signal is used as a reference to eliminate these undesired effects, and provide self-calibration functions in the sensor.

In the third year of the program a new white light interferometry-based signal demodulation system was developed. Both the SCIIB system and the white light system have their own specific advantages. The white light system was developed to provide extremely high resolution measurements at moderate frequencies. The SCIIB system provides very high frequency response high resolution measurements. The white light system was employed in the field tests for pressure, temperature and flow measurement.

This report describes in detail the development of the automated sensor fabrication system; two separate instrumentation systems – SCIIB and white light; temperature, pressure, flow and acoustic sensors; sensor packaging methods; and results of the successful field testing in Tulsa, OK and Coalinga, CA.

## 2.0 Background

Data published by the U.S. Department of Energy [1] indicate that approximately two-thirds of the oil discovered in the U.S. remains in the ground after the primary, secondary and tertiary recovery operations have been completed. This is largely due to the limited availability of information concerning reservoirs, well operation and well-to-well interrelations. Real-time, on-line measurement and monitoring of some key physical parameters as well as their temporal and spatial variations in reservoirs and wells is therefore vitally important. Significant improvements in the capability, cost-effectiveness and reliability of instrumentation for oil recovery can lead to reductions in development cost, lower operating costs and higher recovery factors.

Real-time monitoring of temperature in wells is important in the monitoring and management of steam floods in heavy oil reservoirs, detecting inflows in horizontal wells, and in optimizing the performance of electrical submersible and progressive cavity pumps. Continuous reliable downhole pressure measurements from wells will provide key data that will permit better, faster reservoir characterization and improved forecasting of reservoir capability, thereby permitting operators to optimize the economic recovery of reserves. Measurement of oil flow at various critical locations in a reservoir would provide important information about reservoir architecture, geometrical dimensions, zonal performance, and well-to-well interactions, and further contribute to reservoir optimization and reserves recovery. Acoustic wave detection would provide 4D geophysical data, sand influx data, hydrate or wax detection, and completion/infrastructure monitoring. This would provide an excellent view of reservoir depletion as well as permit the optimization of production infrastructure.

Although the measurement of these physical parameters is highly desirable in the oil industry, the hostile environment involved in wells and reservoirs, the strict technical requirements on measurements, and the unavailability of reliable sensors has unfortunately made obtaining the needed data impractical. Some of the major measurement difficulties include 1) remote operation, 2) immunity to electromagnetic interference (EMI), 3) high temperature and pressure environments, 4) strict requirements on measurement resolution and accuracy, 5) small size, and 6) multi-year reliability. Moreover, due to the increasing application of offshore drilling and horizontal wells, some of the measurement difficulties described above are further increased. These combined difficulties render conventional electrical and electronic sensors and measurement devices very difficult to apply and incapable of meeting the current and future oil industry's needs. This situation suggests that innovative sensors be developed to support the industrial efforts for more efficient and economical oil recovery, which benefits the entire nation.

Optical fiber-based sensing instrumentation has been demonstrated to be especially attractive for the measurement of a wide variety of physical and chemical parameters because of such inherent advantages as 1) an immunity to EMI, 2) avoidance of ground loops, 3) capability to

respond to a wide variety of measurands, 4) avoidance of electric sparks, 5) resistance to harsh environments, 6) remote operation, 7) capability of multiplexing, and 8) ease of integration into large-scale fiber networking and communication systems. Because of these inherent advantages, fiber sensors are attractive to the oil industry.

Most of the fiber sensors developed to date may be classified into two groups: interferometers in which optical phase is affected, and intensity-based devices in which optical intensity is modulated. In general, interferometric sensors have the advantages of ultra-high resolution, accuracy and configurational versatility. However, they have the disadvantages of relative measurement, costly signal processing and low frequency response. In contrast, the intensity-based devices have the advantages of simple signal demodulation, absolute measurement, and high frequency response. Because of the advantages of these two types of fiber sensors, tremendous efforts have been made to combine the two sensor types into a single sensor design to obtain all the major advantages at the same time. Due to significant difficulties encountered by the researchers, however, limited progress was made.

The Center for Photonics Technology at Virginia Tech developed an optical fiber-based sensor technology, the Self-Calibrated Interferometric/Intensity-Based (SCIIB) fiber sensor [2]. To our knowledge, this was the first time to successfully realize the combination of fiber interferometry and intensity-modulated sensing in a single sensor element. In addition to the generic advantages of optical fiber sensors, the new technology has also been shown to have all the distinct advantages of interferometric and intensity-based sensors, while their disadvantages are eliminated or significantly minimized.

The purpose of this four and a half -year program was to expand the basic breakthrough fiber optics telemetry technology to develop cost-effective, reliable fiber sensors optimized for downhole applications in the oil industry, to meet the increasing needs for innovative sensors that allow significant improvement in oil recovery. The program involved active participation from Chevron and the University of Tulsa.

### 3.0 Specification of Technical Requirements

In the first year of this program, CPT personnel worked closely with the engineers from Baker Hughes and Chevron to specify the technical requirements for the downhole measurements. The specifications for sensor performance shown in Table 3-1 were adopted based on input from Baker Hughes and used as guidelines for sensor design and fabrication.

**Table 3-1. Initial sensor specifications.**

Sensor	Specification	Value
Temperature	range	-40 to +200°C
	accuracy	± 1.0°C
	resolution	0.01°C
	pressure	To 20,000 psia
Pressure	ranges	0 to 5,000 psia 0 to 10,000 psia 0 to 16,000 psia 0 to 20,000 psia
	accuracy	± 0.03% F.S.
	resolution	0.01 psia
	temperature	-55 to +250°C
Flow	range	0 to 100,000 barrels/day
	accuracy	10% F.S.
	resolution	0.1% F.S.
	temperature	0 to 177°C
	pressure	0 to 16,000 psia

## 4.0 SCIIB Sensor System Overview

The self-calibrated interferometric/intensity-based (SCIIB) fiber optic sensor successfully combines the advantages of both the interferometric and the intensity-based fiber sensors in a single system. Through proper sensor design, the SCIIB technology can provide absolute measurement of various parameters with the full self-compensation capability for source power fluctuation and changes in fiber loss. Starting with a review of fiber optic Fabry-Perot sensing techniques, this chapter presents the SCIIB system configuration, followed by a detailed discussion of the unique signal processing method and the results of the preliminary sensor performance testing.

### 4.1 Principle of Operation

The basic SCIIB configuration is shown in Figure 4.1. The light from a broadband optical source is launched into a two-by-two fiber coupler and propagates along the optical fiber to the sensor head. For the multimode SCIIB system (which is suitable for short distance application), the light source is an 850nm LED. In the single mode system, a 1310nm SLED is used. As shown in the inset of Figure 4.1, the input fiber and a reflector are thermally fused to a hollow glass tube with a predetermined air gap separation. By thermally fusing the glass capillary tube to the glass fibers, the use of organic adhesives such as epoxy is avoided, eliminating the temperature limits, temperature-dependent mechanical properties and hysteresis of those adhesives. The incident light is first partially reflected at the endface of the input fiber ( $R_1$  in Figure 4.1). The remainder of the light propagates across the air gap to the reflector surface where a second reflection ( $R_2$ ) is generated. The two reflections travel

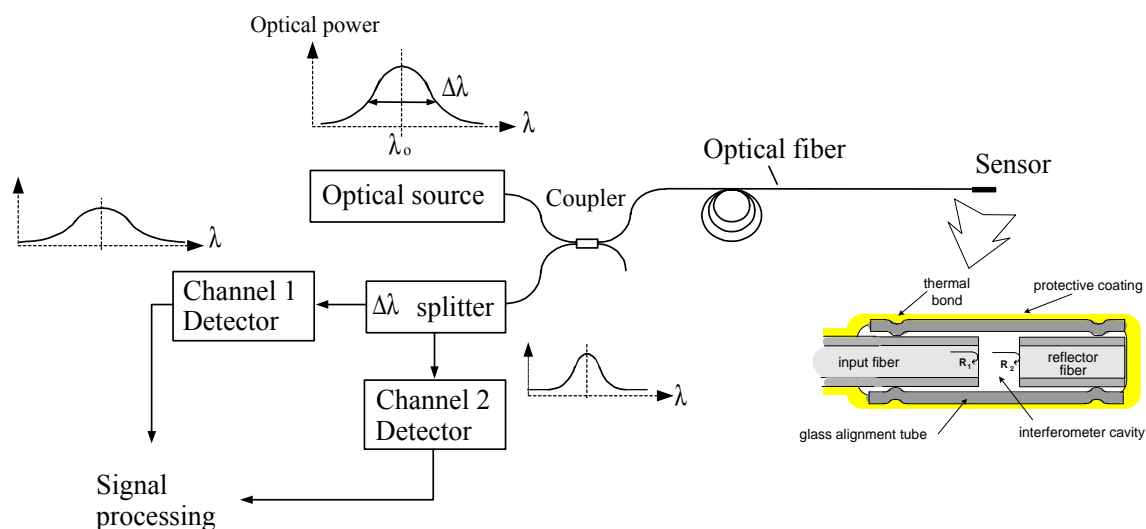


**Figure 4.1. Illustration of the principle of SCIIB fiber optic sensor system.**

back along the same input fiber through the same coupler to the photodetection end. The signal-processing portion of the SCIIB system extracts the information about the Fabry-Perot cavity length, which is related to various measurands governed by different physical laws.

In order to overcome problems associated with conventional fiber interferometric sensors, such as relative measurement, low frequency response, and complexity in signal demodulation, a special optoelectronic signal demodulation method is employed that allows self-calibrating absolute measurement with high frequency response. When the source coherence length is longer than the path length difference of the two legs in an interferometer, interference is observed when the two reflections are combined; when it is less than the path length difference, interference does not occur, and the combination of the two beams results in the sum of their intensities. In the SCIIB system, the coherence length of the sensor channel (Channel 2 in Figure 4.1) is engineered to exceed the path length difference in the Fabry-Perot cavity (twice the gap length), resulting in interference fringes as the gap length is changed by the measurand of interest. The coherence length of the reference channel (Channel 1 in Figure 4.1) is adjusted to be much shorter than the path length difference in the Fabry-Perot cavity. Therefore, no interference occurs and the power output of the reference channel is simply the sum of the optical power of the two reflections R1 and R2. Both channels are affected by changes in fiber loss, bending, connector loss and fluctuations in source power, while only the sensor channel exhibits changes due to the effect of the desired measurand, e.g. temperature or pressure, on the gap length.

As shown in Figure 4.2, when the cavity length changes, one photodetector exhibits an interference signal output while the other is relatively unchanged because the initial air-gap length is larger than the coherence length of the original source. The undesired fluctuations can be canceled out by taking the ratio of the two channels. To simplify the processing and interpretation of the sensor output, the sensor probe is designed so that the optical intensity of the output over the expected full range of the measurand remains within the quasi-linear

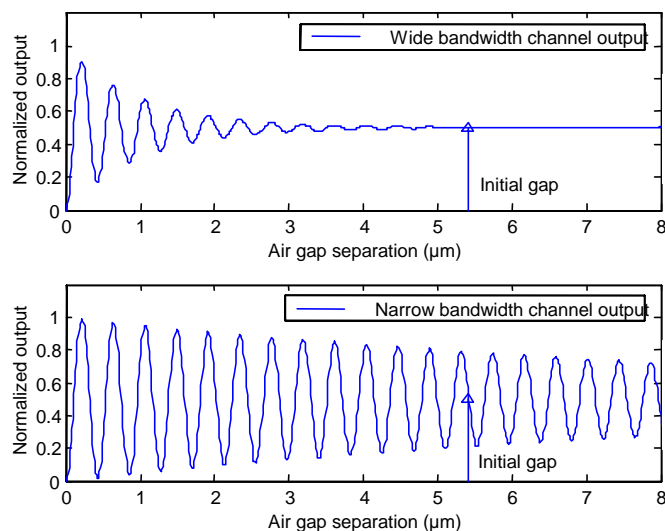


**Figure 4.2. Illustration of the two channel outputs of the SCIIB sensor.**

portion of the interferometric output. This is accomplished by controlling the length, diameter, wall thickness, and the modulus of elasticity of the capillary alignment tube during sensor fabrication. In this way, complicated signal processing involving fringe counting or spectral decomposition can be avoided, and a simple photodetector used.

The SCIIB fiber optic sensor system can be used to measure different physical parameters, for instance, temperature, pressure, strain and acoustic waves. The sensor head can be specially designed to be only sensitive to the parameter of interest. In general, the measurand interacts with the sensor head and causes a change of the air gap. The SCIIB sensor system relates the air gap change to the measurand according to the physical principles governing the interaction, and directly gives the measuring results.

#### 4.1.1 Optimal Cavity Length

The coherence length of a source is inversely proportional to its spectral width. The coherence length  $L_c$  can be estimated by

$$L_c \approx \frac{\lambda_c^2}{\Delta\lambda}, \quad (4-1)$$

where  $\lambda_c$  is the central wavelength of the source and  $\Delta\lambda$  is the spectral width of the source. Assuming that the spectral characteristics of the original source spectrum and the optical bandpass filter can be approximated as Gaussian profiles with a spectral width of  $\Delta\lambda_1$  and  $\Delta\lambda_2$ , the output spectra of the two SCIIB channels can thus be expressed by

$$I_{s1,s2}(\lambda) = \frac{2I_{10,20}}{\sqrt{\pi}\Delta\lambda_{1,2}} \exp\left(-\frac{(\lambda - \lambda_c)^2}{\Delta\lambda_{1,2}^2}\right), \quad (4-2)$$

where  $I_{10,20}$  are the optical powers of the two channels respectively, and  $\lambda_c$  is the central wavelength for both channels (here, we assume that the two channels have the same central wavelength). The interference signals resulting from the spectra of the two channels can thus be written as

$$I_{1,2} = R \cdot \int_{-\infty}^{\infty} I_{s1,s2}(\lambda) [1 + \eta^2(1 - R)^2 - 2\eta(1 - R) \cos(\frac{4\pi}{\lambda} L)] d\lambda, \quad (4-3)$$

where

$I_{s1,s2}$  are the spectral power density distribution of the two channels respectively,

$R$  is the reflectance at the boundary of the air and the fiber endface,

$L$  is the cavity length, and

$\eta$  is the coupling coefficient of the Fabry-Perot cavity. It is a function of the cavity length  $L$ , the lateral offset, and the angular offset. Because the initial cavity length usually is chosen to be very small, the optical loss of the cavity is very small. Therefore,  $\eta$  can be approximated as 100%.

The reflectance  $R$  can be calculated by

$$R = \left[ \frac{(n - n')}{(n + n')} \right]^2, \quad (4-4)$$

where  $n$  is the refractive index of the fiber core, and  $n'$  is the refractive index of the medium forming the cavity between two fibers, which in our case is the air. The reflectance at the fiber endfaces is thus about 4% of the total incident optical power.

Notice that since the reflectance is relatively small, the interference signals given by Eq. 4-3 can thus be approximated by

$$I_{1,2} \approx 2R \cdot \int_0^{\infty} I_{s1,s2}(\lambda) \left[ 1 - \cos\left(\frac{4\pi}{\lambda} L\right) \right] d\lambda, \quad (4-5)$$

Eq. 4-5 indicates that the interference signal is the superposition of interference contribution of all the spectral components, assuming that the photodetectors have a flat response over the source emission spectrum. By taking the ratio of the two channels outputs, the SCIIB output is then given by

$$s = \frac{I_2}{I_1} \approx \frac{\int_{-\infty}^{\infty} I_{s2}(\lambda) \left[ 1 - \cos\left(\frac{4\pi}{\lambda} L\right) \right] d\lambda}{\int_{-\infty}^{\infty} I_{s2}(\lambda) \left[ 1 - \cos\left(\frac{4\pi}{\lambda} L\right) \right] d\lambda}. \quad (4-6)$$

The output signals from the two SCIIB channels and the ratio given by Eq. 4-6 are plotted as a function of the sensor cavity length in Figure 4.3 and Figure 4.4 for the singlemode fiber sensor case, corresponding to a source spectral width of 40nm and bandpass filter spectral width of 10nm, and in Figure 4.5 and Figure 4.6 for the multimode fiber sensor system, corresponding to a source spectral width of 70nm and bandpass filter spectral width of 10nm. If the sensor probe is fabricated such that it has an initial cavity length larger than the coherence length of Channel 1 but smaller than the coherence length of Channel 2, then, as shown in Figure 4.3 and Figure 4.4, Channel 1 becomes an intensity channel with its output relatively unchanged, while Channel 2 retains its highly visible interference fringes as the cavity length changes. The output from Channel 1 (non-interference channel) and Channel 2 (interference channel) of the SCIIB sensor can then be expressed as

$$I_1 \approx 2RI_{10}, \quad (4-7)$$

and

$$I_2 = 2R \cdot I_{10} \cdot \alpha \cdot \left[ 1 - \gamma \cos\left(\frac{4\pi}{\lambda} L\right) \right], \quad (4-8)$$

where,  $\alpha$  is the power loss of the optical filter in Channel 2, given by

$$\alpha = \frac{I_{20}}{I_{10}}, \quad (4-9)$$

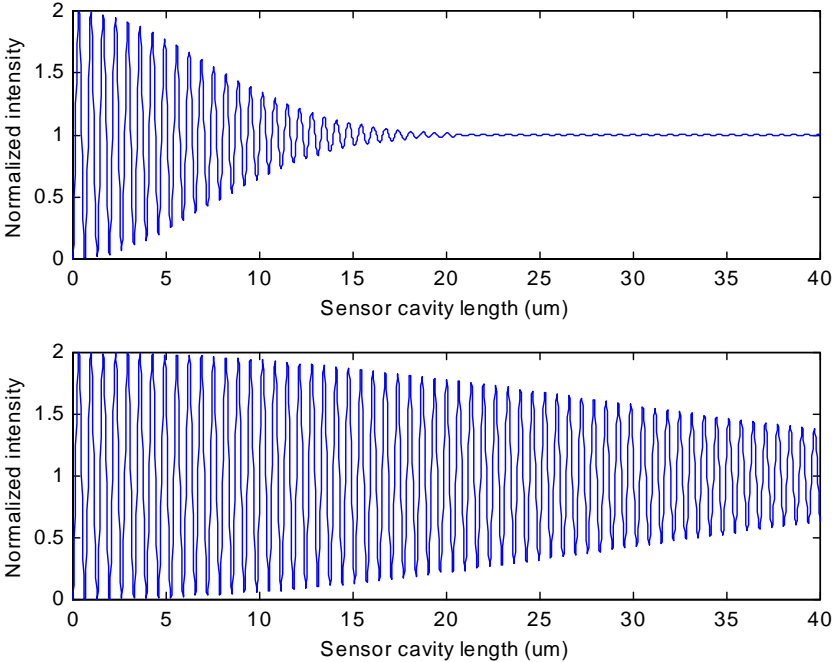


**Figure 4.3. Interference fringes of the two SCIIB channels for a source spectral width of 40nm and center wavelength of 1310nm, and a bandpass filter spectral width of 10nm, corresponding to the singlemode fiber sensor system.**

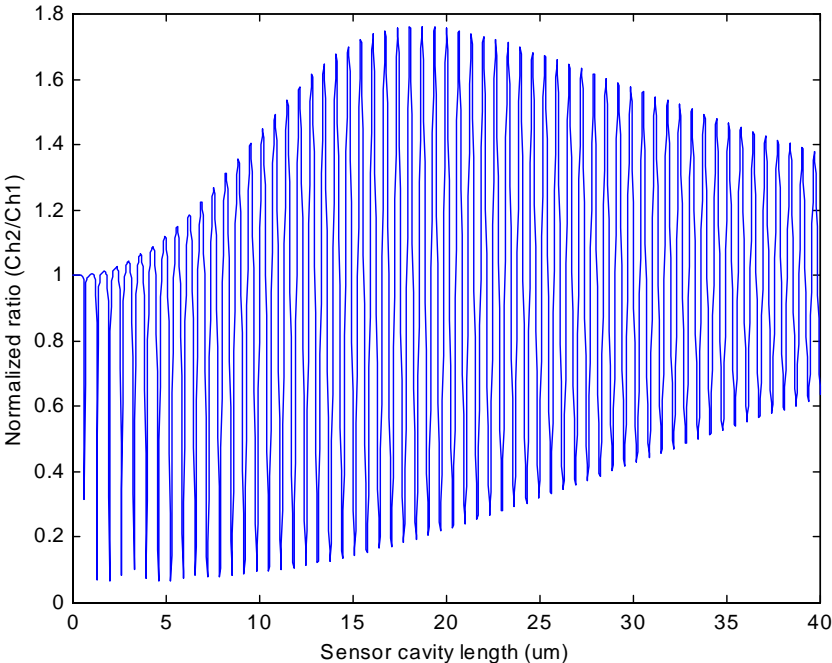


**Figure 4.4. Ratio of the two channel outputs shown in Figure 4.3.**

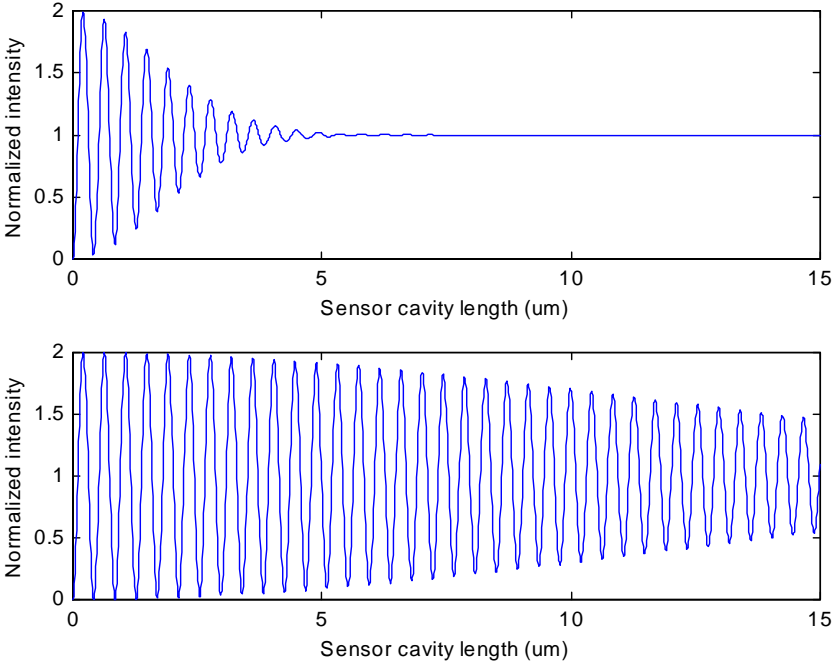


**Figure 4.5. Interference fringes of the two SCIIB channels for a source spectral width of 70nm and center wavelength of 850nm, and a bandpass filter spectral width of 10nm, corresponding to the multimode fiber sensor system.**

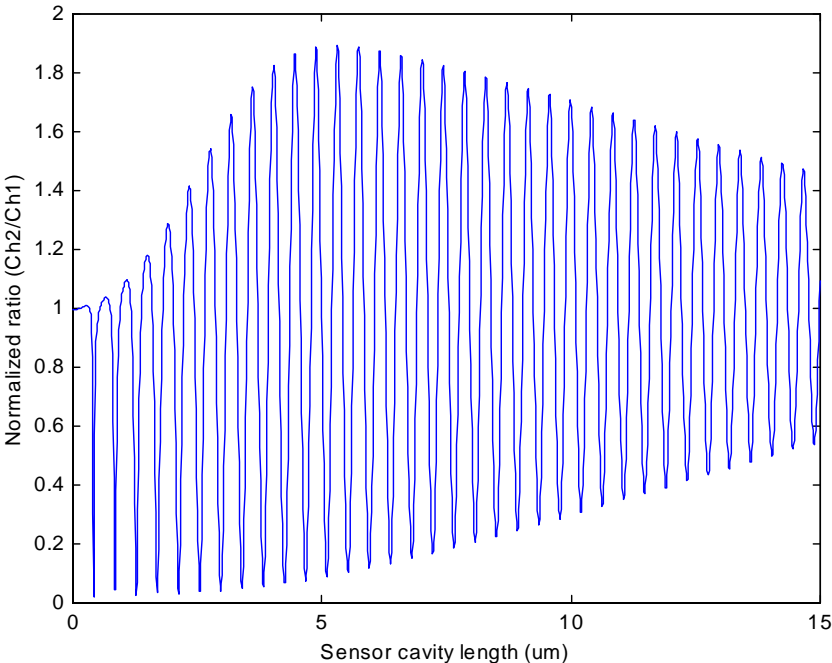


**Figure 4.6. Ratio of the two channel outputs shown in Figure 4.5.**

and  $\gamma$  is the fringe visibility of the Channel 2 signal, defined by

$$\gamma = \frac{I_{\max} - I_{\min}}{I_{\max} + I_{\min}}, \quad (4-10)$$

where,  $I_{\max}$  and  $I_{\min}$  is the maximum and minimum intensity of the optical interference respectively. The fringe visibility in our case is a function of  $\eta$ ,  $R$ , and  $\Delta\lambda_2$ .

In principle, continuously tracking the phase change of the interference fringes in Channel 2 would permit measurement of the change of the cavity length of the sensor head, and similar to the output of a regular interferometer, the measurement will have ultra-high sensitivity. One period of fringe variation corresponds to an air gap change of one-half of the optical wavelength. However, fiber loss variations and laser power drift can introduce errors in the amplitude of the interference signal and result in poor measurement accuracy. To avoid these two adverse effects, Channel 1 is used as a reference signal, and the SCIIB sensor output is evaluated as the ratio of the two signals of the two channels, given by

$$\begin{aligned} s = \frac{I_2}{I_1} &\approx \frac{2RI_{10}\alpha[1 - \gamma \cos(\frac{4\pi}{\lambda}L)]}{2RI_{10}} \\ &= \alpha[1 - \gamma \cos(\frac{4\pi}{\lambda}L)] \end{aligned} \quad (4-11)$$

This ratio is only a function of the Fabry-Perot cavity length, eliminating these two sources of error from the final measurement result.

To assure proper self-referencing of the SCIIB sensor system, it is important to choose an optimal initial sensor cavity length that gives the signal channel maximum fringe visibility and at the same time suppresses the interference of the reference channel to minimum. The choice of the optimal initial cavity length will mainly depend on the spectral widths of the two SCIIB channels. For example, in the case shown in Figure 4.3 and Figure 4.4, the initial cavity length can be chosen between 20 and 30 $\mu\text{m}$ . For the case shown in Figure 4.5 and Figure 4.6, the initial cavity length can be somewhere between 7 and 12 $\mu\text{m}$ . Other considerations in determining an optimal initial cavity length will be discussed in greater detail in the sections below .

#### **4.1.2 Linear Operating Range**

Regular interferometric sensors suffer from the disadvantages of sensitivity reduction and fringe direction ambiguity when the sensor output reaches the peak or valley of an interference fringe. Sensitivity is reduced since at the fringe peak or valley the change in optical intensity is zero for a small change in the sensor cavity length. Fringe direction ambiguity refers to the difficulty in determining from the optical intensity whether the sensor cavity is increasing or decreasing. To avoid these two problems, the SCIIB sensor head is designed and fabricated to operate only over the semi-linear range of a half fringe, as shown in Figure 4.7, so that a one-to-one quantitative relation between output intensity and the sensor cavity length is obtained.

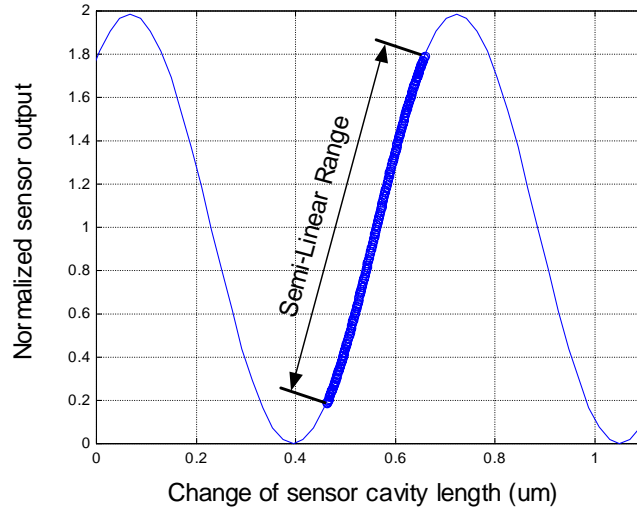


**Figure 4.7. Illustration of a semi-linear fringe operating range.**

The operating range of the SCIIB sensor is defined based on its sensitivity. From Eq.4-11, the sensitivity of the SCIIB sensor can be calculated as

$$Sensitivity = abs\left(\frac{ds}{dL}\right) = abs\left(\alpha\gamma \frac{4\pi}{\lambda} \sin\left(\frac{4\pi}{\lambda} L\right)\right). \quad (4-12)$$

The maximum sensitivity, given by

$$Maximum \ Sensitivity = \alpha\gamma \frac{4\pi}{\lambda}, \quad (4-13)$$

is obtained at the quadrature (Q)-points of the interference fringes. Correspondingly, we define the operating range of the SCIIB sensor as the range where its sensitivity remains within 60% of the maximum sensitivity:

$$\{Operating \ Range\} = Solution\left\{abs\left(\alpha\gamma \frac{4\pi}{\lambda} \sin\left(\frac{4\pi}{\lambda} L\right)\right) \leq \gamma \frac{4\pi}{\lambda} \cdot 60\%\right\}, \quad (4-14)$$

which results in the maximum change in the signal level  $\Delta s$ , given by

$$\Delta s_{max} = 1.6\alpha\gamma. \quad (4-15)$$

## 4.2 SCIIB Advantages

In addition to the generic fiber sensor advantages such as small size, lightweight, remote operation, immunity to EMI, electrically non-conducting, and chemically inert, the unique SCIIB signal processing method combines the advantages of both interferometric and intensity-based sensors providing a number of other major advantages as summarized as below.

**Ultra-high sensitivity**

The SCIIB fiber optic sensor can offer very high resolution since the essence of the signal processing is based on interferometry.

**Absolute measurement**

The operating range of the SCIIB sensor is limited to the semi-linear range of half of an interference fringe; therefore the sensor output is a unique and almost linear function of the change of the cavity length. This one-to-one relation between the sensor output and the cavity length makes it possible to measure the absolute value of the sensor cavity length after the initial cavity length is chosen and fixed. Not only is the direction ambiguity problem resolved, but the sensitivity of the sensor is also kept relatively constant over the entire operating range.

**Minimized complexity in signal processing**

Because the signal processing of the SCIIB sensor only involves optical power detection and a simple ratio operation of the two output signals, the complexity of the system is kept to a minimum.

**Self-compensation capability**

Since the original broadband source spectrum is used as a reference signal, the drift of source power and fluctuations in fiber attenuation are thus fully compensated by the SCIIB signal processing.

**High frequency response**

Because very simple signal processing is used, the SCIIB sensor has a very high frequency response, which may be used to detect very high-speed signals such as acoustic waves or aerodynamic forces.

**Geometric flexibility**

The Fabry-Perot sensor head structure offers great design flexibility to accommodate the requirements of different applications.

**4.3 Multimode Fiber Sensor**

Two SCIIB sensor systems were designed and fabricated; multimode fiber was used for short distance applications, and singlemode for long distance applications. Since multimode fibers have a larger core diameter than singlemode fibers, optical power can be coupled from the source into the fiber more efficiently. However, because of the relatively high loss of multimode fibers at the operating wavelength, the system is primarily designed for low cost, short distance applications, typically less than one kilometer from the actual sensing region to the signal processing unit. The multimode system was designed to operate at a center wavelength of 850 nm and uses 62.5 $\mu$ m/125 $\mu$ m standard telecommunication fibers. A schematic and photograph of the multimode SCIIB sensor system are shown in Figure 4.8. The spectrum of the LED source (Honeywell, HEF 4854-014) is shown in Figure 4.9, with its central wavelength of 850 nm, spectral width of 70 nm, and the typical output power of 120

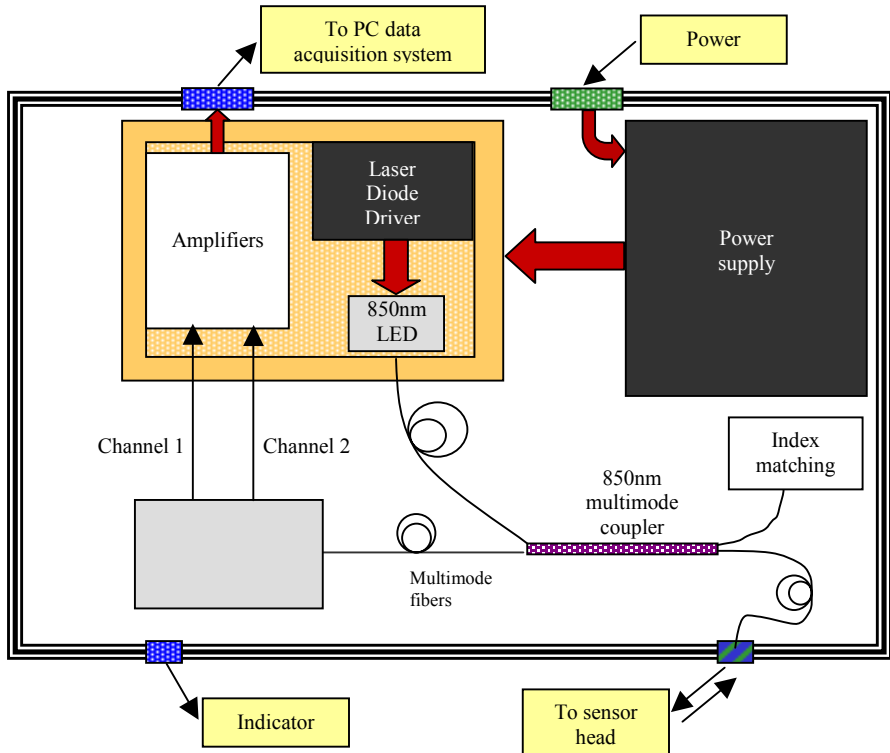
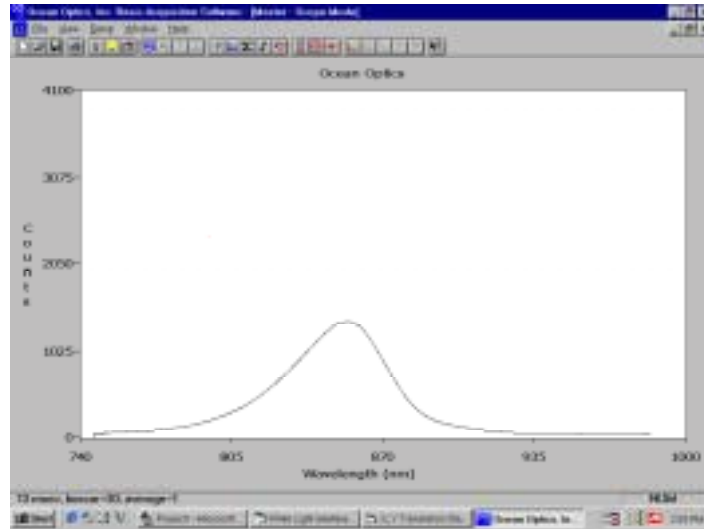


Figure 4.8. Multimode fiber SCIIB sensor system, schematic (top) and photograph (bottom).



**Figure 4.9. Optical spectrum of the source LED for the multimode SCIIB system (center wavelength 850 nm, spectral width 70 nm, and typical output power 120  $\mu$ W).**

$\mu$ W. In the multimode fiber system, a polarization insensitive cubic beam splitter with a splitting ratio of 50:50 is used to split the light from the sensor head into two channels. One portion of the light from the beam splitter passes through an optical bandpass filter with a center wavelength of 850 nm and a full width at the half maximum (FWHM) of 10 nm. Two silicon detectors with large effective areas (31 mm<sup>2</sup>) are used to receive the signals of the channels. Following the two transimpedance amplifiers, the signals from the two channels are sampled and converted to digital data by a high-precision A/D converter. The ratio of the two channel signals is then calculated by the host computer.

#### 4.4 Singlemode Fiber Sensor

Singlemode fibers have very low optical attenuation, typically about 0.3dB/km at 1300nm and 0.2dB/km at 1550nm. Therefore, light can be transmitted for very long distances. However, due to the small core diameter of singlemode fibers, it is relatively difficult to efficiently couple light from optical sources into the fiber. Also, low-noise detection of the light at 1300nm or 1550nm requires expensive InGaAs photodetectors. Therefore, the cost of singlemode fiber-based sensor systems is much higher compared to multimode systems. The singlemode fiber-based SCIIB sensor system is primarily designed for long distance applications, typically longer than one kilometer from the actual sensing region to the signal processing unit.

The singlemode SCIIB system (Figure 4.10) is designed to operate at a center wavelength of 1310 nm using a single-mode fiber to transmit optical signals between the sensor probe and the signal processing unit. The source is a high power superluminescent light emitting diode (SLED) provided by Anritsu Corp. (AS3B281FX), with a center wavelength of 1312 nm, a spectral width of 41.5 nm, and output power of 1.21mW from a 9/125 $\mu$ m pigtailed single-mode fiber. Figure 4.11 shows the source spectrum measured by an Ando Optical Spectrum

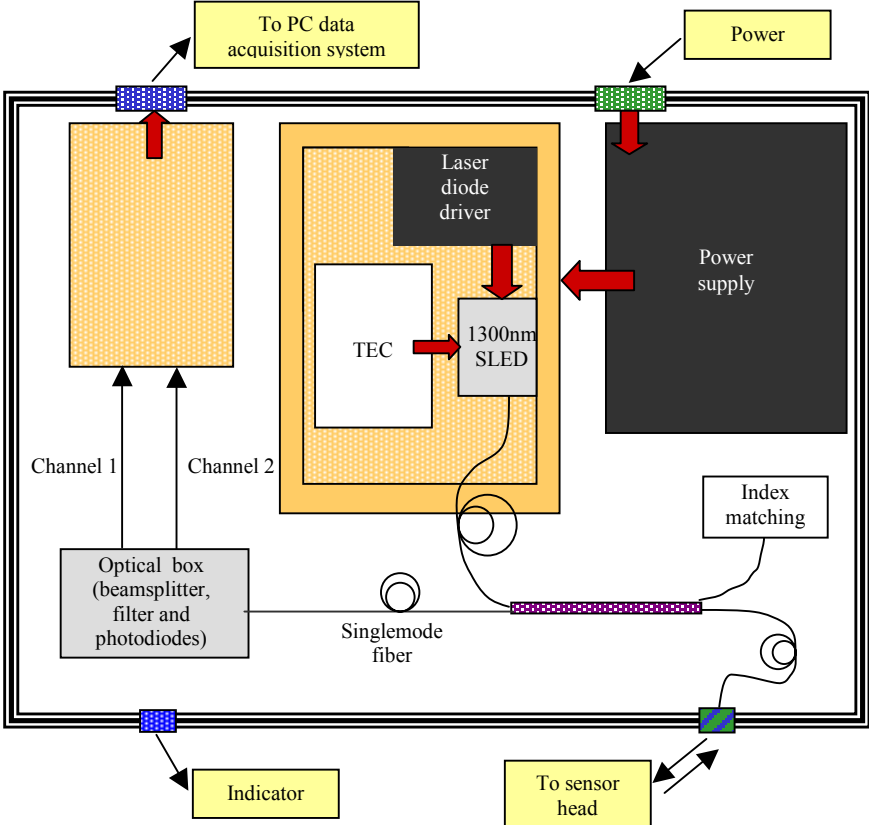
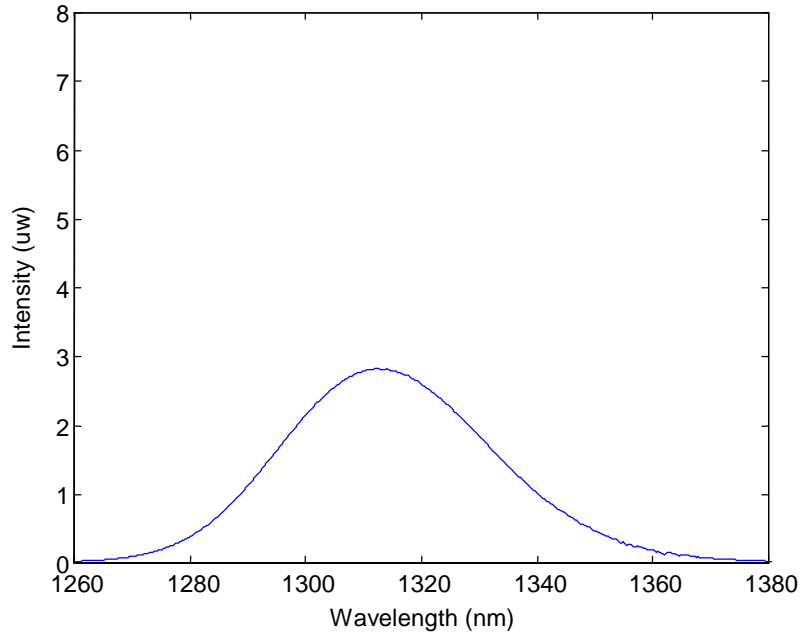


Figure 4.10. Singlemode fiber SCIIB sensor system, schematic (top) and photograph (bottom).



**Figure 4.11. Optical spectrum of the SLED source measured by an Ando OSA (center wavelength 1312 nm, spectral width 41.5 nm, output power 1.21mW from a 9/125 $\mu$ m pigtailed single-mode fiber).**

Analyzer (OSA). A polarization insensitive beam splitter with a splitting ratio of 50:50 at 1310nm is used to split the light signal from the sensor head into two channels. In one channel, the light passes through an optically neutral density filter in order to balance the two channels in terms of the optical power, and is detected by a large effective area InGaAs photo-detector and amplified to produce the reference signal. The light in the other channel passes through an optical bandpass filter with a center wavelength of 1310 nm and a FWHM spectral width of 10 nm. Because the spectral width of this channel is much narrower, an interferometric signal as the function of the sensor cavity length can thus be obtained after the photodetection. Similar to the multimode fiber-based system, the two channels' outputs are sampled and converted to digital signals and input to a host computer where the ratio and linearization can be performed easily.

## 4.5 Preliminary Sensor Testing

The self-compensating capability of the SCIIB systems were evaluated during the first two years of the program for source drift, fiber bending-induced loss, and spectral changes, which are unavoidable in actual fiber deployment.

### 4.5.1 Fiber loss compensation

An important advantage of the SCIIB sensor is its capability to self-compensate for fiber loss variation or source output power drift by using two channels with different coherence lengths. The self-compensation results from the fact that the optical power received at these two channels originates from the same source and experiences the same transmission path.

For instance, when fiber loss changes, it impacts both channel outputs, and by referencing one channel output to the other, we can eliminate this fluctuation.

Figure 4.12 shows experimental results from the fiber loss compensation test of the multimode fiber-based SCIIB system. The fiber used in the test was a standard telecom 62.5/125 $\mu\text{m}$  graded index multimode fiber, and the source was an LED with a center wavelength of 851.3 nm and a spectral width of 71.4 nm, provided by Honeywell (HEF4854-014). We introduced power loss to the system by manually bending the fiber to various diameters without changing the sensor cavity length. Two multimeters were used to record the output voltages from each channel. As expected, although the outputs of the two channels changed due to the increasing power loss, the ratio of the two channel outputs remained the same. The sensor output ratio varied less than 1% over the full testing range (up to 50% of the total power loss), which indicated that the implemented multimode fiber-based SCIIB system had an excellent self-calibration capability to compensate for variations in fiber loss.

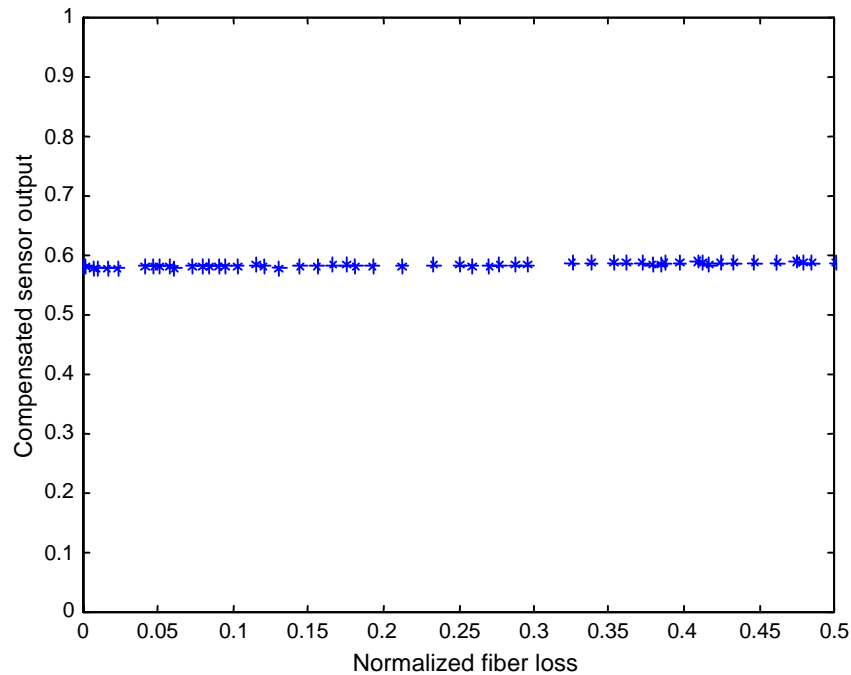


**Figure 4.12. Multimode fiber SCIIB sensor output compensated for fiber bending loss.**

The singlemode fiber SCIIB instrumentation was also evaluated. Without connecting to the sensor probe, the output power of the source (SLED) was varied by changing the driving current of the source chip. With the endface of the lead-out fiber well cleaved, the SCIIB instrumentation system should output a constant ratio, although each channel's output could change when the total optical power was changed. Two multimeters were used to record the two channels' output voltages and the ratio of the two channel was calculated. Figure 6-1 plots the recorded output from the two channels, as well as their ratio with respect to the driving current of the light source. Figure 4.14 magnifies the change in the SCIIB ratio as a

function of the normalized optical power of the source. The ratio of the two channels only changes by about 0.3% as the total optical power changes up to 50%.

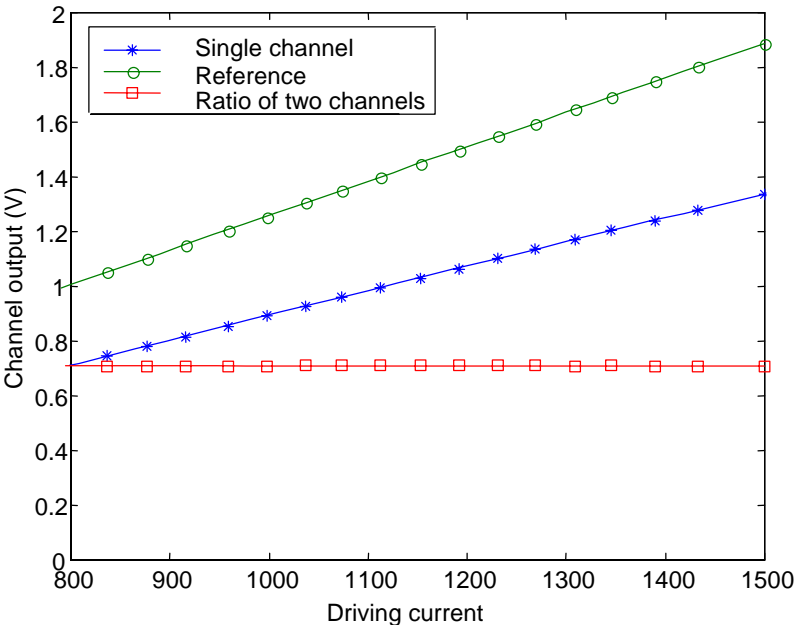


Figure 4.13. SCIIB output versus driving current of the optical source.

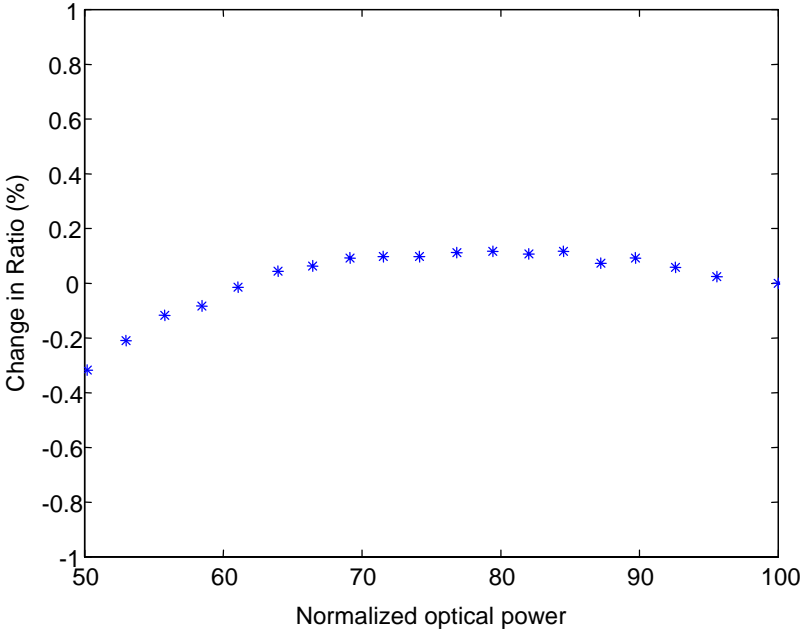


Figure 4.14. Change in SCIIB output ratio versus the normalized source power change.

Theoretically, changing the driving current of a semiconductor optical source would also change the spectrum in addition to the optical power change. The distortion of the source spectrum would also introduce error to the measurement result through the non-centered filtering effect; the measurement error is proportional to the offset between the center of the

optical bandpass filter and that of the source spectrum. Therefore, the error shown in Figure 4.14 also indicates the contribution from the source spectrum distortion. Nevertheless, the experimental results reveal that the SCIIB signal processing has a good self-compensation capability as expected.

#### 4.5.2 Compensation for bending-induced spectral changes

In the singlemode case, changes in the optical spectrum are also induced by fiber bending. To investigate the measurement error induced by this spectral change, we conducted an experiment to study singlemode fiber bending. The schematic of the experimental setup is shown in Figure 4.15. A SLED made by Anritsu Corp. (AS3B281FX) with a center wavelength of 1310 nm, spectral width of 40 nm, and output power of 1.21mW was used as the source. The output from the source was transmitted through a section of testing fiber, and its spectrum was studied using an optical spectrum analyzer (OSA). By manually bending the fiber to certain radii, we were able to study the bending induced spectrum changes.

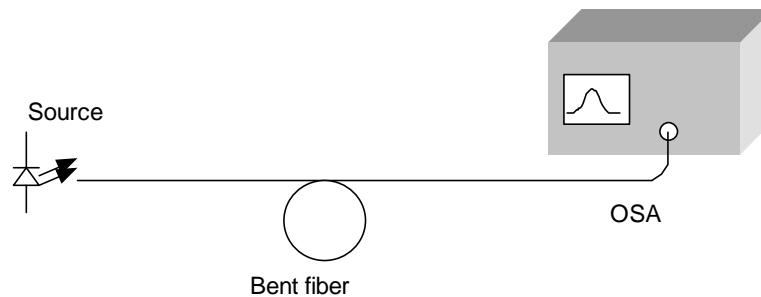


**Figure 4.15. Experimental setup used to evaluate for fiber bending induced spectral changes.**

In the first experiment, a section of standard telecom singlemode fiber was used. The fiber was bent to successively smaller radii of 12 mm, 5 mm, 4 mm, and 3 mm, respectively. The recorded spectra at these bending radii are plotted in Figure 4.16. The results indicate that the spectrum transmitted in standard telecom singlemode fiber can easily be distorted by bending the fiber. Within the spectral range of interest (1300 nm-1320 nm), the spectral fluctuation can reach a few dB under severe bending, which can easily introduce measurement errors to the SCIIB system.

Spectral fluctuation in telecommunications fibers is mainly due to the large mode field diameter of the waveguide. To eliminate these fluctuations, we can use bending insensitive fiber, which has a much smaller field diameter. In the second experiment, we used a section of bending insensitive single-mode fiber to repeat the above test. The fiber was purchased from Spectran Communication Fiber Technologies, Inc., and was designed for operation at the wavelength of 1300 nm. The test results are shown in Figure 4.17. Spectral fluctuations in the bending insensitive fiber are much smaller compared with that of the standard telecom fiber. Even under severe bending, the transmitted spectrum does not exhibit spectral fluctuations. Therefore, the experiment results suggest that the bending induced measurement errors can be minimized by applying bending insensitive fiber to the SCIIB system.

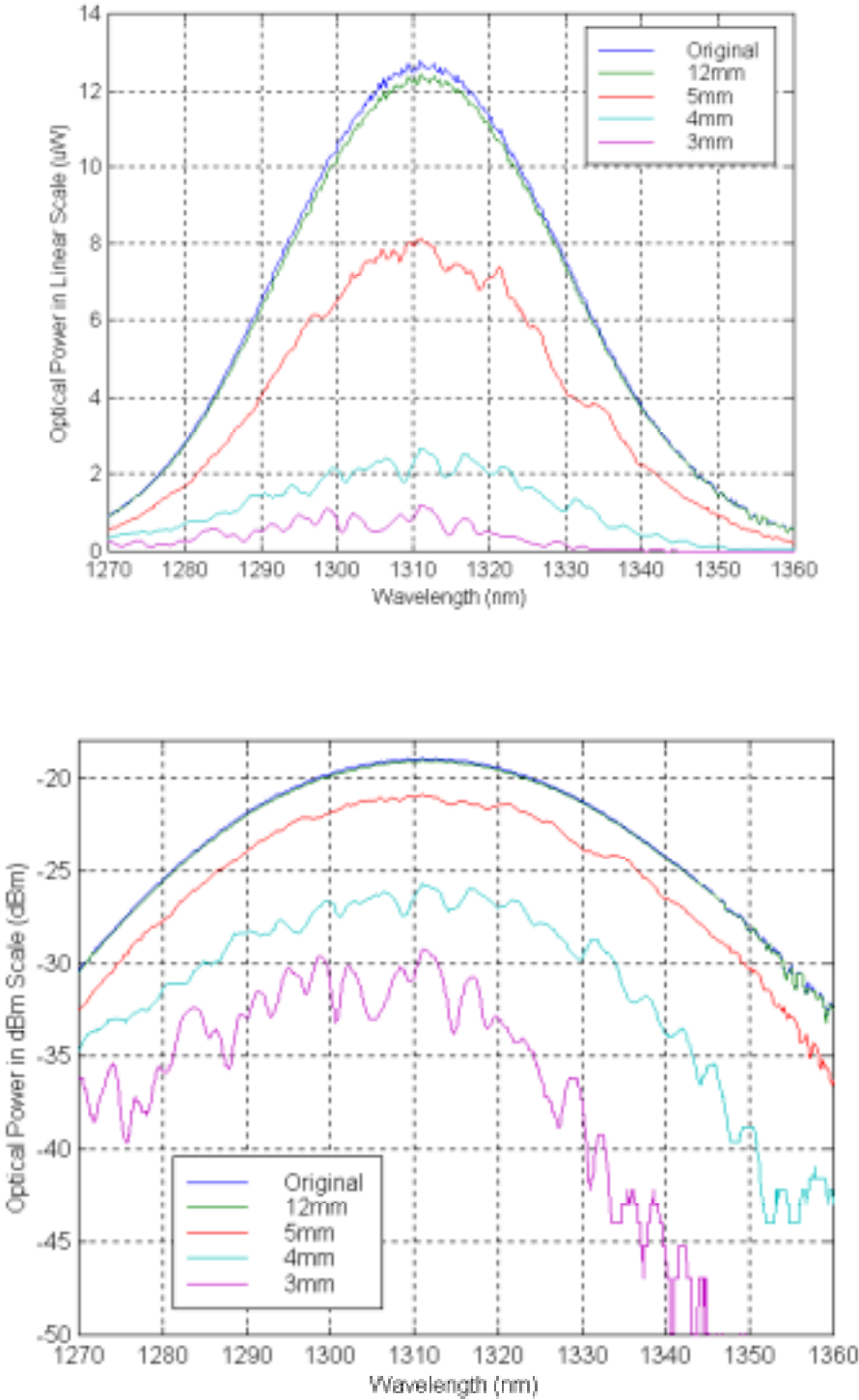


**Figure 4.16. Bending induced spectral changes in standard singlemode telecommunications fiber.**

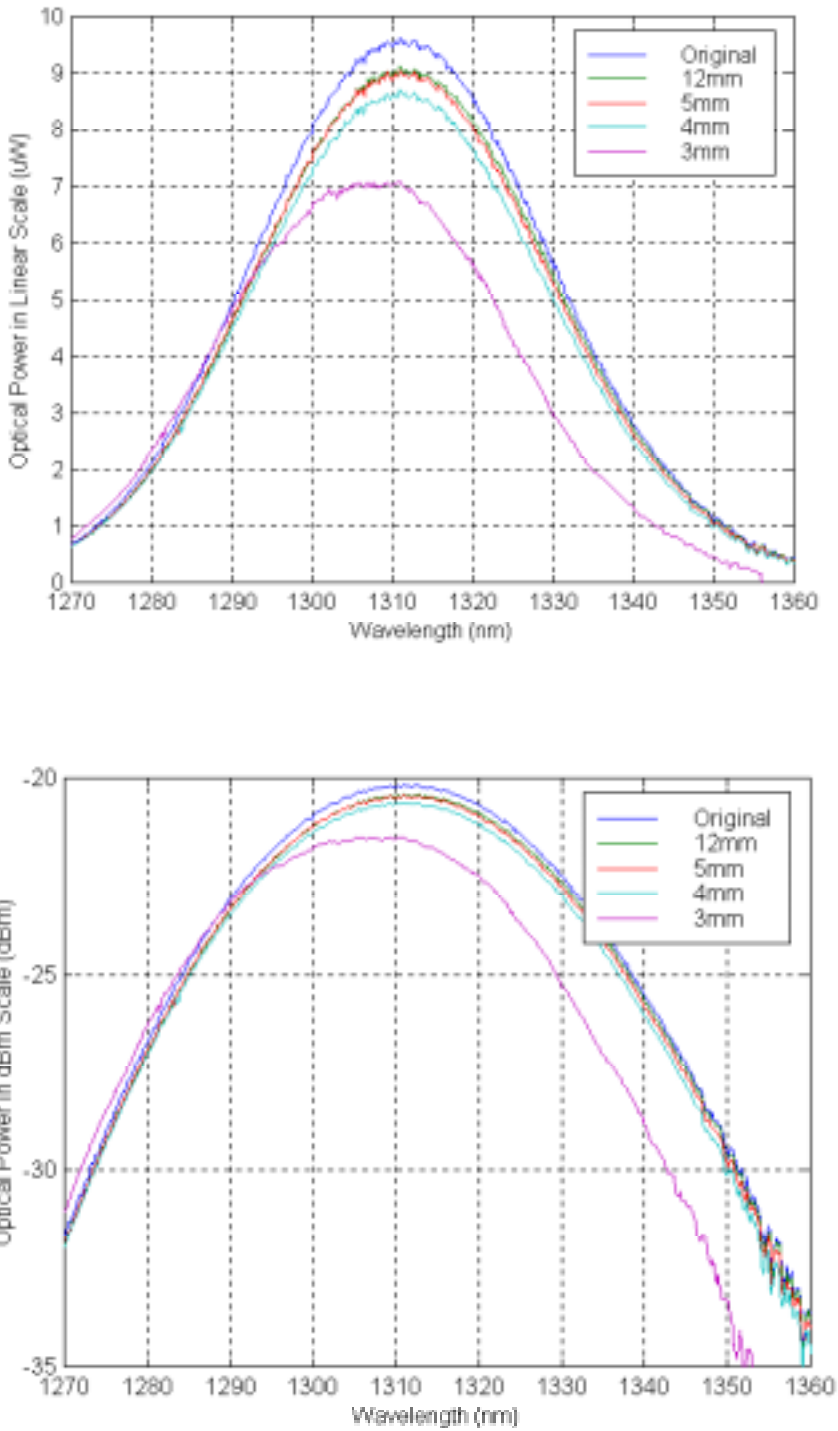


Figure 4.17. Bending induced spectral changes in bend insensitive singlemode fiber.

## 5.0 Instrumentation Systems

The first two years of the program were focused on the development of the SCIIB instrumentation. In the third year, a breakthrough in sensor fabrication monitoring led to the parallel development of the white light interferometer instrumentation system, which was ultimately shown to be the optimal system for high resolution, low speed applications. This chapter describes both of these efforts.

### 5.1 Signal Demodulation System I – SCIIB

In order to achieve high frequency response for the measurement of acoustic signals or flow, it was necessary to develop a high speed signal processing method for the SCIIB output. This section describes the design and implementation of advanced DSP-based signal processing techniques for the SCIIB sensor system.

#### 5.1.1 Design and implementation

A schematic of the DSP-based SCIIB system, including a SCIIB sensor optical system, a DSP development platform, and an analog daughter module with A/D and D/A converters, is shown in Figure 5.1. Two important features are unique in this system. First, the output signals from the two channels of the SCIIB system are processed in the digital domain using a DSP chip. Second, in order to improve the system signal-to-noise ratio (SNR), the light source is modulated at a high frequency, and synchronously demodulated at the receiving end. These two features enable low noise detection and demodulation of the weak optical signal at a very high speed. In the multimode case, a 2 MHz sweep function generator

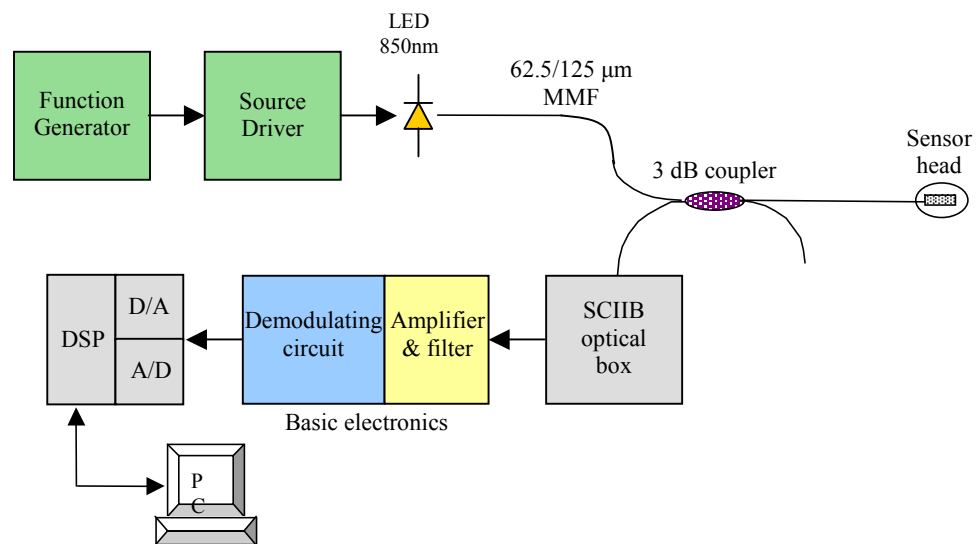


**Figure 5.1. DSP based SCIIB high speed sensor system.**

(TENMA, Inc.) is used to modulate an 850 nm high power fiber optic LED (HFE4854, Honeywell) through a laser diode driver (Newport Corp). As discussed above, the modulated LED light is coupled to a 62.5/125 $\mu\text{m}$  multimode 3-dB 2x2 fiber coupler. One output leg of the coupler is connected to a SCIIB fiber sensor head, and the other output is inserted into index matching gel to eliminate reflections from the fiber tip. The signal output from the sensor head is transmitted back to the SCIIB optical box through the same fiber coupler. The SCIIB optics box splits the input signal into a reference channel (without bandpass filter) and a signal channel (with bandpass filter). Two photodetectors are used to convert the two channel signals to electrical signals. The detected signals are amplified, filtered and demodulated by means of the basic electronics, then sampled by an A/D module (ADCA Corp.) and processed in the DSP platform.

An optimal operating modulation scheme had to be developed to support the noise-reducing amplitude modulation of the source. In order to ensure that the HFE4856 LED operated in its linear region during modulation, the current-power (I-P) curve of the LED was plotted, as shown in Figure 5.2. Based on this result, we chose an operating point of 50 mA with the modulation region from 10 mA to 90 mA. The modulating frequency was chosen to be 100 kHz.

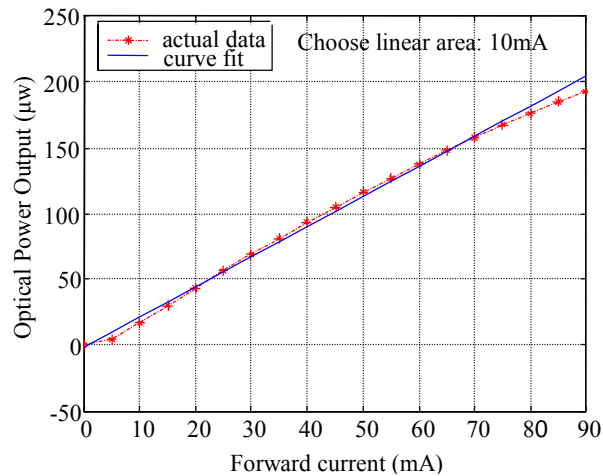


**Figure 5.2. Current-power curve of the HEF4856 LED.**

#### 5.1.1.1 Basic electronics design

The basic electronics involved in the system include the high frequency preamplifier circuit, the narrow bandpass filter circuit and the amplitude demodulation circuit. The specifications of the designed basic electronics include:

<b>Modulation frequency:</b>	100 kHz
<b>Signal bandwidth:</b>	10 kHz
<b>Current gain for reference channel:</b>	$\times 108$ A/V
<b>Gain for signal channel:</b>	$\times 109$ A/V
<b>Signal to noise ratio:</b>	>60dB

#### 5.1.1.2 *A/D converter design*

An A/D converter is necessary to convert the amplified and demodulated signal to the digital domain so that the DSP hardware can further process the signal and improve the measurement accuracy. Three factors were considered in A/D module selection: high accuracy, high throughput and ease of interface with the DSP hardware. After investigating products from a number of companies, we chose the DSP data acquisition board 5404DHR-V manufactured by ADAC, Inc. The 5404DHR-V board provides a 16-bit A/D with a maximum throughput of 100K samples/s, two 16-bit D/A voltage output channels, 8 multiplexed analog input channels and 4 C40 Comm ports to communicate with TM320C40 DSP chips.

#### 5.1.1.3 *DSP hardware design*

TM320C4X series DSP chips made by Texas Instruments have successfully been used in various engineering applications. The TMS320C40 is the original member of the 'C4x family. It features a power CPU that can deliver up to 30 MIPS/60 MFLOPS, 6 built-in communication ports allowing high speed data exchange, the capability of parallel processing by group several DSP chips together, and well-developed supporting software.

We selected the SMT320 DSP system manufactured by Sundance, Inc. as the main DSP development platform for the system. The platform consists of a SMT320 PCI carrier board with 4 TIM-40 module slots and a SMT302 TIM-40 module. The advantage of this structure is ease in extension to more C40s for parallel processing. The high-speed communication between the DSP platform and the A/D module is realized by using the Comm-ports of the DSP.

#### 5.1.1.4 *Software design*

The development of the supporting software for the DSP system is the most critical part of the entire system design. The software will have a significant influence on the final system performance. It is based on the mixed programming of C language and the 3L DSP function library. The main functions of the DSP supporting software include data acquisition, data transferring, digital filtering, signal demodulation, and data output.

### 5.1.2 *SCIIB System Noise Analysis*

As an optoelectronic measurement system, the performance of the SCIIB sensor is limited by the noise associated with each individual electronic and optical component and their combined effects. A detailed analysis of these noise effects on the system performance is a critical design step since it provides a guideline for achieving an optimal system performance. This section provides a detailed analysis of the noise performance of the single mode fiber (SMF) SCIIB sensor system, including both the electronic noise and the optical noise. Based on the results of the analysis, performance improvement measures are proposed.

#### 5.1.2.1 *Electronic Noise of the SMF SCIIB System*

Usually, the ultimate performance limit of an optoelectronic sensor system is associated with the receiving electronics used to interrogate the sensor. This can be further decomposed into

two parts: 1) the fundamental photon noise limit (shot noise) of the photodetector, and 2) thermal noise of the electronics. In addition to the noise associated with the receiving electronics, the noise of the optical source, such as the optical power fluctuation and the source wavelength drift, can also cause measurement errors to the sensor system. Here the optical power fluctuation of the source is no longer a concern because as discussed above, the SCIIB sensor system can self-compensate for the source power fluctuation. The error caused by the optical wavelength drift of the source will be discussed in the next section as it is categorized as part of the optical noise.

#### Photodetector Noise:

Shot noise: Photodetector shot noise is a manifestation of the fact that the electric current consists of a stream of electrons that are generated at random times. It was first studied by Schottky in 1918 and has been thoroughly investigated since then. The photodiode current generated in response to a constant optical signal can be written as

$$I(t) = I_p + i_s(t), \quad (5-1)$$

where  $I_p = RP_{in}$  is the average current and  $i_s(t)$  is a current fluctuation related to shot noise.  $P_{in}$  is the input optical power to the photodetector and  $R$  is the responsivity of the photodetector.

Mathematically,  $i_s(t)$  is a stationary random process with Poisson statistics which in practice can be approximated by the Gaussian statistics. The autocorrelation function of  $i_s(t)$  is related to the spectral density  $S_s(f)$  by the Wiener-Khinchin theorem

$$\langle i_s(t)i_s(t + \tau) \rangle = \int_{-\infty}^{\infty} S_s(f) \exp(2\pi if\tau) df. \quad (5-2)$$

The spectral density of shot noise is constant and is given by  $S_s(f) = qI_p$  (shot noise is called white for this reason).  $q$  is the charge on an electron ( $1.6 \times 10^{-19}$  C). Note that  $S_s(f)$  is a two-sided spectral density, as negative frequencies are also included in (5-2). If only positive frequencies are considered by changing the lower limit of integration to zero, the one-sided spectral density becomes  $2qI_p$ . The noise variance is obtained by setting  $\tau=0$  in (5-2) and is given by

$$\sigma_s^2 = \langle i_s^2(t) \rangle = 2qI_p \Delta f, \quad (5-3)$$

where  $\Delta f$  is the effective noise bandwidth of the receiver. The actual value of  $\Delta f$  depends on where the noise is measured and it usually corresponds to the bandwidth of the amplifying circuits.

Dark current: All photodetectors generate some current noise even in the absence of an optical signal because of stray light or thermal generation of electron-hole pairs. This residual current is referred to as the dark current. Since the dark current  $I_d$  also generates shot noise, its contribution is included in the following equation

$$\sigma_s^2 = 2q(I_p + I_d)\Delta f. \quad (5-4)$$

Thermal noise: At a finite temperature, electrons in any conductor move randomly. Random thermal motion of electrons in a resistor manifests as a fluctuating current even in the absence of an applied voltage. The load resistor in the front end of an optical receiver adds such fluctuations to the current generated by the photodiode. This additional noise component is referred to as thermal noise. It is also called Johnson noise or Nyquist noise after the two scientists who first studied it experimentally and theoretically. Thermal noise can be defined as the current fluctuation  $i_T(t)$ . Mathematically,  $i_T(t)$  is modeled as a stationary Gaussian random process with a spectral density that is frequency independent up to 1Thz (nearly white noise) and is given by [3]

$$S_T(f) = \frac{2k_B T}{R_L}, \quad (5-5)$$

where  $k_B$  is the Boltzmann constant ( $1.38 \times 10^{-23} \text{J/}^\circ\text{K}$ ),  $T$  is the absolute temperature, and  $R_L$  is the load resistor. As mentioned before,  $S_T(f)$  is also the two-sided spectral density. The autocorrelation function of  $i_T(t)$  is given by

$$\langle i_T(t) i_T(t + \tau) \rangle = \int_{-\infty}^{\infty} S_T(f) \exp(2\pi i f \tau) df. \quad (5-6)$$

Therefore, the noise variance is obtained by setting  $\tau=0$  and becomes

$$\sigma_s^2 = \langle i_s^2(t) \rangle = \int_{-\infty}^{\infty} S_T(f) df = \frac{4k_B T}{R_L} \Delta f, \quad (5-7)$$

where  $\Delta f$  is the effective noise bandwidth which is defined the same as for the shot noise case.

#### Noise assumption at the transimpedance amplifier:

The developed SCIIB system uses two transimpedance amplifiers to convert the optical current signals to the voltage outputs of the two channels. It is thus worthwhile to describe the noise performance of the transimpedance amplifier as it converges the shot noise and the thermal noise, and also introduce other noises to the final sensor output.

The noise equivalent circuit of the transimpedance amplifier is given in Figure 5.3. The bandwidth of the transimpedance amplifier is RC limit and given by

$$\Delta f = \frac{1}{2\pi R_f C_f}, \quad (5-8)$$

where  $R_f$  is the feedback resistance, and  $C_f$  is the feedback capacitance. The output voltage ( $e_o$ ) from the transimpedance amplifier can be calculated by

$$e_o = e_s + e_{no} = I_p R_f + e_{no}, \quad (5-9)$$

where  $e_s$  is the signal voltage of the amplifier,  $I_p$  is the signal generated photocurrent from the photodetector, and  $e_{no}$  is the voltage noise of the amplifier which includes the shot noise of the detector generated a noise voltage, the thermal noise of the feedback resistor ( $e_{noR}$ ), the amplifier's input current noise ( $e_{noi}$ ), and the amplifier's input voltage noise ( $e_{noe}$ ).

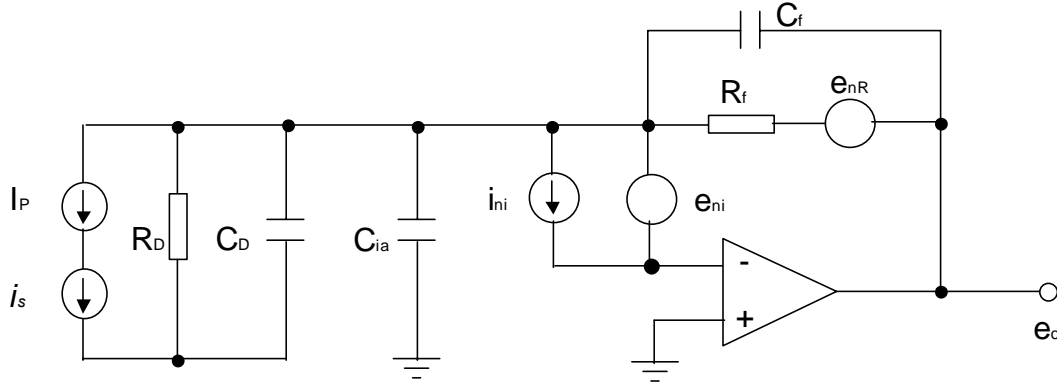


**Figure 5.3. Noise equivalent circuit of the transimpedance amplifier.**

PD shot noise: The shot noise generated at the photodetector ( $i_s$ ) will be amplified by the feedback resistor and gives the corresponding voltage noise ( $e_{nos}$ ) given by

$$e_{nos} = i_s R_f = \sqrt{2q(I_p + I_d)\Delta f} R_f. \quad (5-10)$$

Thermal noise: The thermal noise of the feedback resistor generates a voltage noise  $e_{noR}$  that can be expressed by

$$e_{noR} = \sqrt{4k_B T R_f \Delta f}. \quad (5-11)$$

Amplifier input current noise:  $e_{noi}$  is the output noise components produced by the amplifier's input current noise ( $i_{ni} = \sqrt{2qI_{B-}\Delta f}$ ) which is a shot noise produced by the input bias current  $I_{B-}$ . This noise current flows directly through the feedback resistor, producing a noise voltage of

$$e_{noi} = R_f \sqrt{2qI_{B-}\Delta f}. \quad (5-12)$$

Choosing a FET-input operational amplifier with an  $I_{B-}$  in the picoampere range generally makes this noise component negligible for practical levels of feedback resistance. For the AD795 operational amplifier, the input current noise is  $I_{B-} = 13fA$ .

Amplifier input voltage noise:  $e_{noe}$  represents output noise components produced by the amplifier's input voltage noise  $e_{ni}$ . Within the response boundary of the op amp, this noise can be calculated by

$$e_{noe} = \frac{1 + R_f C_i s}{1 + R_f C_f s} e_{ni}. \quad (5-13)$$

This will be a high frequency noise when the capacitors dominate the noise gain. For the AD795 amplifier,  $e_{ni} = 3\mu V$  below 10Hz.

Total voltage noise: The total voltage noise ( $e_{no}$ ) can be obtained by adding the contributions of all the above noises. Since these noises are independent random processes which can be approximately modeled by Gaussian statistics, the total variance of voltage fluctuation at the output of the transimpedance amplifier can be obtained by adding individual variances. Therefore, the combined output voltage noise of all components is given by

$$e_{no} = \sqrt{e_{nos}^2 + e_{noR}^2 + e_{noi}^2 + e_{noe}^2} . \quad (5-14)$$

In consideration of the power budget of the developed SCIIB system: Assume that the maximum output power from the SLED source is 1.6 mW. The coupler introduces a loss of 6dB (75%) because of the double passes. The Fresnel reflection of the fiber endface is 4%. If counting for the two reflections at the sensor head, the total average reflected power will be 8% of the incident power. There are other losses associated with the SCIIB system. For example, the coupling loss of the fiber to the GRIN lens is about 0.2dB (4.5%). The beamsplitter splits the light into the two channels with a ratio of 50:50, which introduces another 50% power loss to each channel. The power seen by the narrow band channel will only be 25% of the original power of the full spectrum because the bandpass filter only slices a portion (10nm spectral width) of the original source bandwidth (40nm). The bandpass filter used in the system also introduces an optical loss of 60%. The maximum operating distance for the single mode fiber sensor is 10km, which will introduce a fiber loss of  $2 \times 0.3\text{dB/km} \times 10\text{km} = 6\text{dB}$  (74.88%) because of the double pass of the light, where 0.3dB/km is the assumed loss at  $\lambda = 1310\text{nm}$  of the singlemode fiber used in connecting the sensor to the signal processing unit. Finally, it is wise to allow a loss margin of 10dB (90%) power loss for the fiber deployment. The loss items with their estimated values are listed in Table 5.1.

**Table 5.1. Optical loss mechanisms in singlemode fiber SCIIB system.**

Optical loss mechanisms	Value
Coupler loss ( $L_c$ ):	75%
Average Fresnel reflection of the fiber ends ( $r_f$ ):	8%
GRIN lens pigtail loss ( $L_{GRIN}$ ):	0.2dB (or 4.5%)
Beamsplitter loss ( $L_{BS}$ ):	50%
Filtering loss ( $L_f$ ):	75%
Bandpass filter loss ( $\eta_{BP}$ ):	60%
Fiber attenuation loss ( $L_f$ ):	$10\text{km} \times 0.3\text{dB/km} \times 2 = 6\text{dB}$ (or 74.88%)
Loss margin for fiber deployment ( $L_{Mrg}$ ):	10dB (90%)

Therefore the optical power seen by the photodetector at the signal channel can be estimated to be

$$P_{in} = P_s \times (1 - L_c) \times r_f \times (1 - L_{GRIN}) \times (1 - L_{BS}) \times (1 - L_f) \times \eta_{BP} \times (1 - L_f) \times (1 - L_{Mrg}) \quad (5-15)$$

$$= 57.6\text{nW}$$

Signal-to-noise ratio estimation of SCIIB electronics:

Based on the above analysis and the estimated optical power seen by the photodetectors of the SCIIB signal channel, we can calculate the estimated signal-to-noise ratio (SNR) of the developed SCIIB system, where SNR is defined as

$$SNR = 10 \log\left(\frac{\text{average signal power}}{\text{noise power}}\right) = 20 \log\left(\frac{\text{average signal voltage}}{\text{noise voltage}}\right) \quad (5-16)$$

$$= 20 \log\left(\frac{e_s}{e_{no}}\right) = 20 \log\left(\frac{I_p R_f}{\sqrt{e_{nos}^2 + e_{noR}^2 + e_{noi}^2 + e_{noe}^2}}\right)$$

where we used the fact that electrical power varies as square of the voltage.

Therefore, the signal-to-noise ratio (SNR) of the electronics of the singlemode fiber SCIIB sensor system can be calculated as shown in Table 5.2, where the noise terms are listed separately. From the table, we can see that the theoretical signal-to-noise ratio of the receiving electronics of the singlemode fiber SCIIB system is about 98.8dB (equivalent to a normalized noise level of  $1.148 \times 10^{-5}$ ). This is, however, by no means the actual SNR of the entire system. As we will see in the analyses of next section, the optical noise will dominate the performance characteristics of the system.

**Table 5.2. SNR calculation of the singlemode fiber SCIIB electronics**

	<b>Value</b>
<b>Shot noise generated voltage noise (<math>e_{nos}</math>):</b>	5.28 ( $\mu$ V)
<b>Thermal noise of the feedback resistor (<math>e_{noR}</math>):</b>	1.62 ( $\mu$ V)
<b>Amplifier's input current noise (<math>e_{noi}</math>):</b>	2.57 (nV)
<b>Amplifier's input voltage noise (<math>e_{noe}</math>):</b>	3 ( $\mu$ V)
<b>Total noise voltage (<math>e_{no}</math>):</b>	6.28 ( $\mu$ V)
<b>Average signal current (<math>I_p</math>):</b>	$57.6\text{nW} \times 0.95\text{A/W} = 54.7$ (nA)
<b>Dark current of the photodetector (<math>I_D</math>):</b>	15 (pA)
<b>Average signal voltage (<math>e_s</math>):</b>	$547 \text{ nA} \times 10^7 \Omega = 0.547$ (V)
<b>Signal-to-noise ratio (SNR):</b>	98.8 (dB)
<b>Equivalent normalized noise level:</b>	$1.148 \times 10^{-5}$

### 5.1.2.2 Optical Noise of the SMF SCIIB System

As discussed previously, the basic optical components in the SMF SCIIB sensor system include the optical source (SLED), fiber coupler, optical fibers, GRIN lens, beamsplitter, and optical bandpass filter. In order to achieve the desired sensor system performance, it is necessary for those optical components to perform their functions accurately. Unfortunately, environmental perturbations, such as temperature changes and mechanical vibrations, can easily introduce noises to the system through the interaction between the optical components

and the outside medium. These noises may deviate the optical components from their desired functions and result in measurement errors. Therefore, it is the purpose of this section to examine the noise performance of the optical system to ensure a reliable optical design.

The interaction between the optical components and the environment disturbance could affect the optical performance of the component in four different aspects: intensity, phase, wavelength, and state of polarization (SOP). The resultant noise from these four aspects is system and component dependent. The SCIIB system is immune to the intensity noise since it has the full capability of self-compensation for the intensity fluctuation by taking the ratio of the two channels' outputs. The phase fluctuation of the optical components will not affect the system performance because the phase of the interference signal from the Fabry-Perot cavity purely depends on the sensor probe itself. The phase shift of the optical components only adds the same amount of phase change to both of the interference components. This common phase shift will be eliminated from the final interference signal of interest. The analysis can thus be narrowed down to the effects of wavelength drifts and changes of the state of polarization.

#### Wavelength Drift Induced Noise:

The SCIIB system measures the pressure signal by monitoring the sensor cavity length change resulting from the applied pressure. Although the sensor cavity length change is read directly from the intensity change, the generation of the signal is based on the basic principle of optical interference. The interference of two optical waves is a sinusoidal function of the phase difference between these two waves, which is inversely proportional to the optical wavelength of the source. It can be imagined that wavelength drifts will introduce a change to the interference signal and result in measurement errors. Usually, the wavelength drift induced error can be analyzed directly from the interference equation. However, the case for the SCIIB system is somewhat different because it is the spectral characteristic of the optical filter that determines the interference signal. Therefore, a detailed investigation of the wavelength drift induced error needs more careful consideration.

Considering the spectral change of the optical bandpass filter: Without any doubt, a spectral change after the optical bandpass filter will directly shift the interference signal. A careful examination of the system reveals that the wavelength drift before the optical bandpass filter can also cause an error through the non-centered filtering and the residual interference fringe in the reference channels.

The optical bandpass filter used in the SCIIB signal channel is a Fabry-Perot type multilayer thin film filter. The spectrum characteristics of the filter are dependent on the thickness and the refractive index of the multilayer thin film, which will change with the ambient temperature because of the thermal expansion effect and the temperature dependence of the refractive index. Assuming that the center wavelength of the filter has a temperature sensitivity of  $0.001\text{nm}/^\circ\text{C}$ , a temperature change of  $70^\circ\text{C}$  (from  $-15^\circ\text{C}$  to  $55^\circ\text{C}$ ) will cause a maximum change of  $0.07\text{nm}$  in the center wavelength.

Taking the derivative of both sides of Eq. (4-1) with respect to  $\lambda$ , we have

$$\frac{ds}{d\lambda} = -\gamma \frac{4\pi L}{\lambda^2} \sin\left(\frac{4\pi}{\lambda} L\right). \quad (5-17)$$

The wavelength drift induced error can thus be calculated by

$$\delta s = abs\left\{\gamma \frac{4\pi L}{\lambda^2} \sin\left(\frac{4\pi}{\lambda} L\right) \delta\lambda\right\}, \quad (5-18)$$

which reaches a maximum at the quadrature points where the sinusoidal function gives its maximum values of  $\pm 1$ , whereas,

$$\delta s_{\max} = \gamma \frac{4\pi L}{\lambda^2} \delta\lambda, \quad (5-19)$$

We have defined the operating range of the SCIIB system in Eq. (4-14). Therefore, the normalized error can be calculated by

$$\frac{\delta s_{\max}}{\Delta s_{\max}} = \frac{\gamma \frac{4\pi L}{\lambda^2} \delta\lambda}{1.6\gamma} = \frac{4\pi L}{1.6\lambda^2} \delta\lambda. \quad (5-20)$$

The normalized error resulting from the wavelength drift of the optical filter is plotted in Figure 5.4 as a function of the initial cavity length of the sensor probe, where the wavelength drift of the filter is assumed to be 0.07nm for the operating temperature range from -15°C to 55°C. As indicated in the figure, the error is proportional to the initial cavity length. For an initial cavity length of 25 $\mu$ m, the normalized error is about 0.8% of the full scale of measurement.

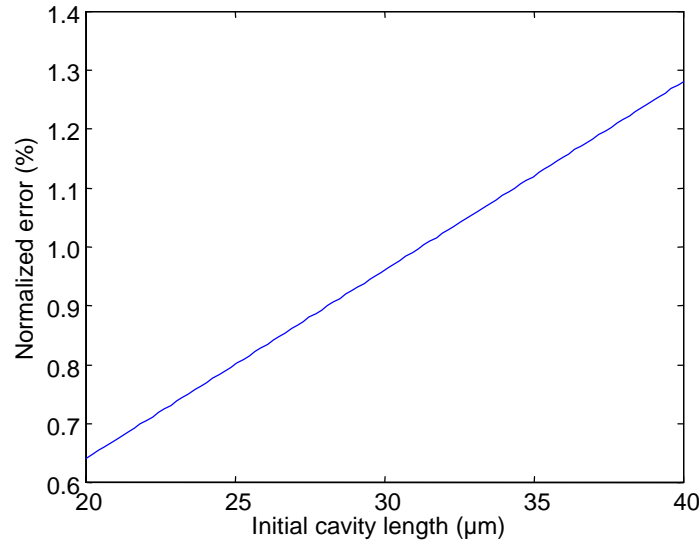


**Figure 5.4. Normalized error induced by the wavelength drift of the filter.**

In order to reduce the error induced by the wavelength drift of the optical filter, and also to ensure good fringe visibility of the signal channel, the initial sensor cavity length needs to be as small as possible. On the other hand, reducing the initial cavity length would generate an

optical interference in the reference channel. This residual interference in the reference channel can cause an error in the measurement results as demonstrated by the following discussion.

Assuming that the residual interference in the reference channel has a fringe visibility of  $\gamma_r$ , the output from the reference channel can be written as

$$I_1' = 2RI_0 \left[ 1 - \gamma_r \cos\left(\frac{4\pi}{\lambda} L\right) \right]. \quad (5-21)$$

The output of the SCIIB system is then

$$\begin{aligned} s' = \frac{I_2}{I_1'} &= \alpha \cdot \frac{1 - \gamma_s \cos\left(\frac{4\pi}{\lambda} L\right)}{1 - \gamma_r \cos\left(\frac{4\pi}{\lambda} L\right)}, \\ &\approx s \left[ 1 + \frac{\gamma_r}{2} \cos\left(\frac{4\pi}{\lambda} L\right) \right] \end{aligned} \quad (5-22)$$

where  $s$  is the original SCIIB output as given by Eq. (4-11).

Both the SLED source and the optical bandpass filter used in the SCIIB system have a center wavelength of 1310nm. However, the actual center wavelength of the source is 3.1nm off from its nominal center wavelength. As schematically shown in Figure 5.5, this will have two effects on the output of the SCIIB system: 1) the center wavelength used to calculate the output of the reference channel in Eq. (5-21) is no longer the same as the signal channel, and 2) the intensity of the signal channel will deviate from the original level of  $\alpha I$ .

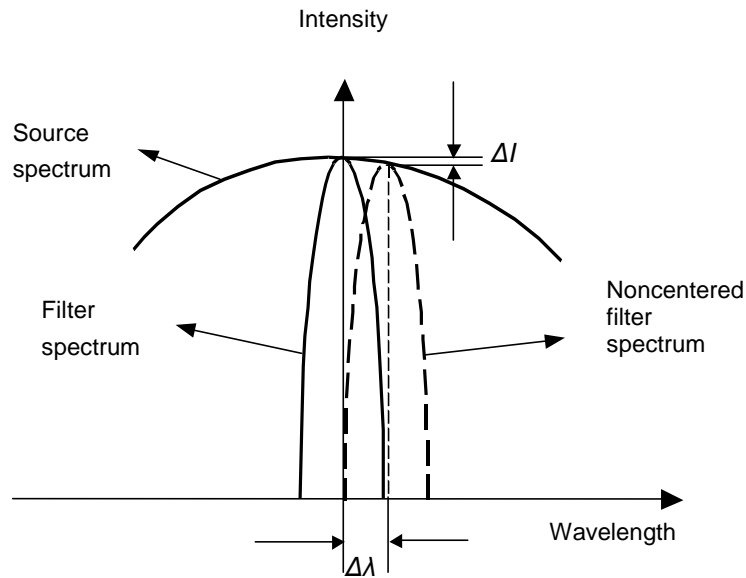


**Figure 5.5. Schematic illustration of non-centered filtering.**

Therefore, Eq. (5-22) can be modified to give the new output of the SCIIB system, given by

$$s' \approx s \left(1 - \frac{\Delta I}{I_0}\right) \left[1 + \frac{\gamma_r}{2} \cos\left(\frac{4\pi}{\lambda - \Delta\lambda} L\right)\right], \quad (5-23)$$

where  $\Delta I$  is the intensity change, and  $\Delta\lambda$  is the center wavelength offset. Both the residual interference in the reference channel and the non-centered filtering themselves will not cause measurement errors directly because once the system is calibrated these deviations are fixed. However, if the wavelength of the light drifts from the original spectrum, for example, because of the temperature induced drift of the source wavelength and the fiber bending induced spectral distortion, there will be errors resulting from these changes.

From Eq. (5-23), the normalized measurement error resulting from the wavelength drift  $\delta\lambda$  can thus be calculated by

$$\left. \frac{\delta s}{s} \right|_{\max} \approx \left\{ \text{abs} \left( \frac{1}{I_0} \frac{dI}{d\lambda} \right) + \frac{\gamma_r}{2} \cdot \frac{4\pi L}{\lambda^2} \right\} \Bigg|_{\lambda - \Delta\lambda} \cdot \delta\lambda, \quad (5-24)$$

where  $I$  is the normalized spectrum of the optical source, which can be modeled by the following Gaussian function

$$I(\lambda) = \frac{2I_0}{\sqrt{\pi}\Delta\lambda_0} \exp\left(-\frac{(\lambda - \lambda_c)^2}{\Delta\lambda_0^2}\right), \quad (5-25)$$

where  $I_0$  is the total optical power,  $\Delta\lambda_0$  is the  $e^{-1}$  half spectral width, and  $\lambda_0$  is the central wavelength. Therefore, we have

$$\frac{1}{I_0} \frac{dI(\lambda)}{d\lambda} = -\frac{2(\lambda - \lambda_c)}{\sqrt{\pi}\Delta\lambda_0^3} \exp\left(-\frac{(\lambda - \lambda_c)^2}{\Delta\lambda_0^2}\right), \quad (5-26)$$

Figure 5.6 shows the calculated results of the normalized measurement error as a function of the wavelength drift given by Eq. (5-24).

The spectrum of a semiconductor optical source is temperature dependent. A change in temperature will cause changes to both the index of refraction of the active medium and the dimensions of the resonant cavity, and hence change the spectrum of the emitting light. To reduce the spectral fluctuation of the source, a thermo-resistor and a thermal electrical controller (TEC) are usually installed very close to the source chip. These two together with the external controlling circuits form a feedback loop that helps to keep the chip temperature unchanged. With the help of the automatic thermal electrical cooling mechanism, the wavelength drift of the optical source can thus be minimized to the level of about 0.2nm.

The spectrum of the light waves transmitted in a fiber will change when the fiber is bent. The fiber bending induced spectrum change (or the fiber bending loss spectrum) is a very complicated phenomenon. Although theoretical modeling of this process is possible, it will be easier and more direct to investigate this phenomenon experimentally. The experimental setup was the same as that described in Section 4.5 and shown in Figure 4.15. As discussed

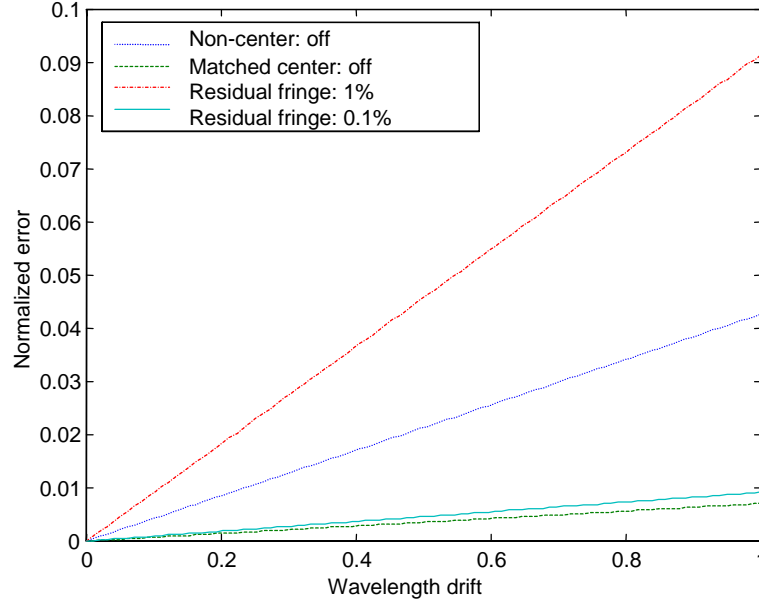


**Figure 5.6. Normalized measurement error resulting from the residual interference in the reference channel and the noncentered filtering, where the initial sensor cavity length is set to be  $L_0=25\mu\text{m}$ .**

above, two types of singlemode fibers were evaluated. In the first experiment, a section of standard telecom singlemode fiber (SMF28<sup>TM</sup> fiber made by Corning Inc.) was used to run the test. The fiber was bent to a series of radii from 12mm to 3mm. The smallest bend that might be encountered when the sensor is deployed in an oil well is about 12mm. The typical spectra of light transmitted in the original and the bent fiber are repeated in Figure 5.7 for convenience. Similar tests were also conducted using a section of bending insensitive singlemode fiber at 1300nm (purchased from Spectran Communication Fiber Technologies, Inc.), with the recorded spectra repeated in Figure 5.8. For the purpose of evaluating the spectral distortion induced phase shift to the interference signal, the change of the effective central wavelength can be calculated from the recorded spectrum data. The calculated typical effective center wavelength change for regular singlemode fiber is about 0.3nm, and that of the bending insensitive fiber is about 0.2nm.

From fiber optic theory, the mode field radius  $w(\lambda)$  of a step-index singlemode fiber can be approximated by [3]

$$w(\lambda) = a \left( 0.65 + \frac{1.619}{V^{3/2}} + \frac{2.879}{V^6} \right), \quad (5-27)$$

where the electric field of the guided mode is assumed to have a Gaussian distribution in shape, and  $V$  is the normalized frequency of the fiber, defined as

$$V = \frac{2\pi}{\lambda} a \sqrt{n_1^2 - n_2^2}. \quad (5-28)$$

Here,  $a$  is the core radius,  $n_1$  and  $n_2$  are the refractive indices of the core and cladding respectively.

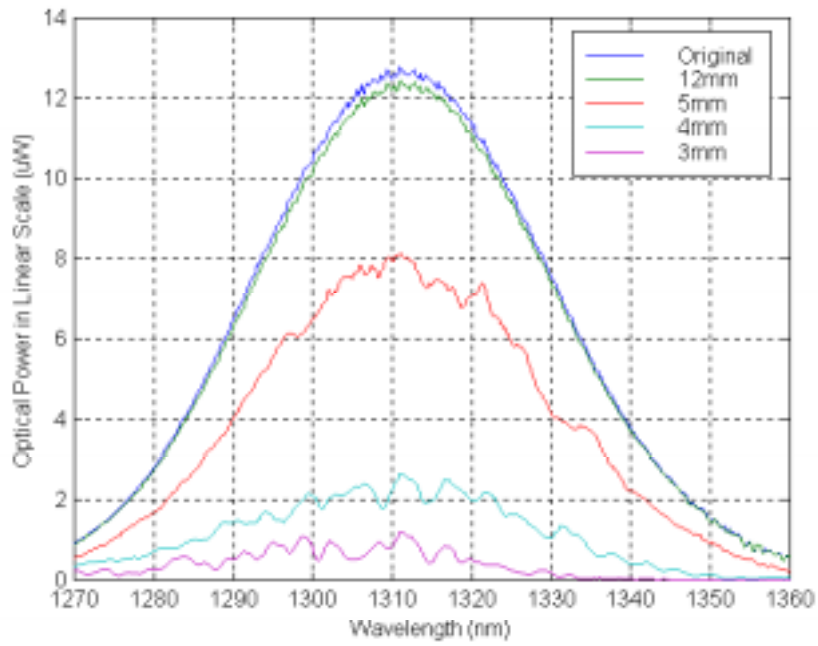


**Figure 5.7.** Bending induced spectral changes in standard telecommunications singlemode fiber.

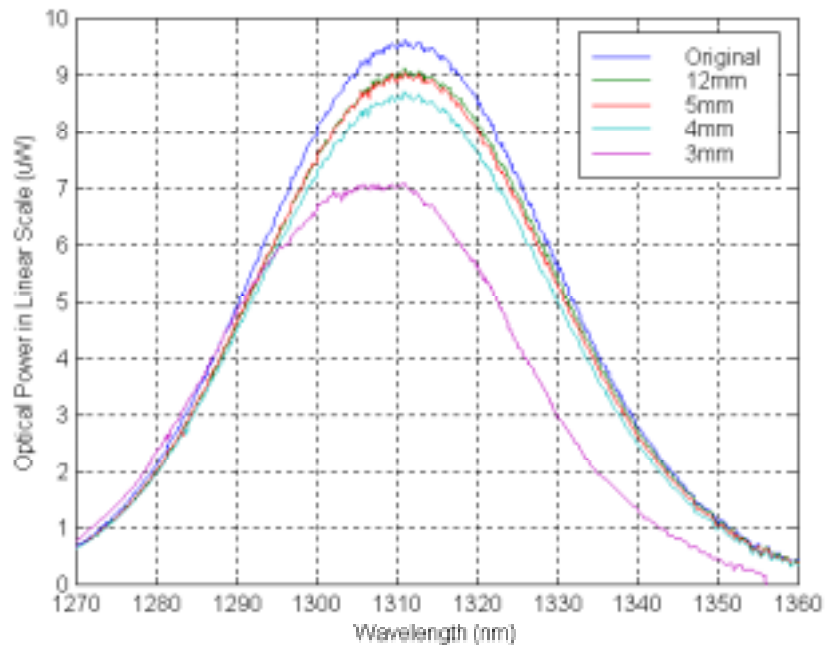


**Figure 5.8.** Bending induced spectral changes in bending insensitive singlemode fiber.

Examining Eq. (5-27) and (5-28) reveals that the mode field diameter of a step-index singlemode fiber is proportional to the wavelength of the light. Longer wavelength light will have a larger mode field diameter when it is transmitted in the fiber. Intuitively, the larger the mode field diameter, the higher the loss when the fiber is bent because the optical energy is less confined inside the waveguide. This explains qualitatively why the long wavelength end of the spectra suffers larger loss compared to the short wavelength end. Because the mode field diameter of the regular telecommunication fiber is larger than that of the bending insensitive fiber, the loss of the regular fiber is higher than that of the bending insensitive fiber.

Bending a singlemode fiber can also cause the coupling between the guided mode and the cladding modes. The coupling between modes results in the transfer of energy between these modes, which is both wavelength and bending radius dependent. Within the spectral range of the source, the coupling can be more favorable to some wavelengths than to others depending on the status of bending. This explains the ripples exhibited in the transmitted spectrum when the fiber was bent.

In general, comparing the experimental results shown in Figure 5.7 and Figure 5.8, the distortions of the spectrum in the bending insensitive fiber are smaller than that of the regular telecom fiber with the same bending radius. Even under severe bending, the transmitted spectrum of the bending insensitive fiber still does not exhibit spectral ripples. The larger distortion of the spectrum in regular telecom fibers is mainly due to the large mode field diameter of the waveguide. However, the difference is small for a relatively large bending radius (>12mm).

#### SOP Induced Noise

The SLED used in the SCIIB system outputs almost linearly polarized light. As the light propagates inside the SMF, the state of polarization will be changed due to both intrinsic and extrinsic birefringence. Although the fiber Fabry-Perot sensor probe is polarization insensitive, the receiving optics of the SCIIB system are polarization dependent. This is largely due to the residual polarization dependence of the optical beamsplitter.

Residual polarization sensitivity of the beamsplitter: The SCIIB receiving optics use a low polarizing cubic beamsplitter (made by OptoSigma Inc.) with a central operating wavelength of 1310nm to separate the signal and reference channels. As shown in Figure 5.9, the beamsplitter has a residual polarization dependence of about 10% in the wavelength range 1250nm-1350nm. This will result in a nonconstant splitting ratio that is dependent on the state of polarization of the input light.

Assuming that the splitting ratio of the beamsplitter as a function of the input SOP is given by

$$r(SOP) = \frac{I_1(SOP)}{I_2(SOP)} \neq 1:1, \quad (5-29)$$

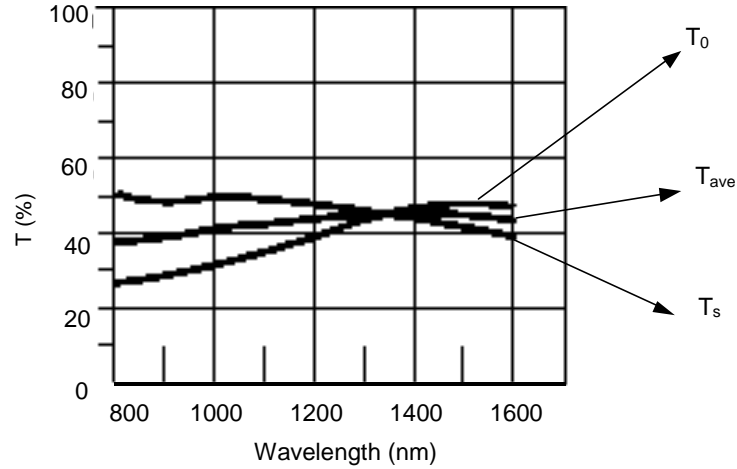


**Figure 5.9. Beam splitter transmission characteristics.**

the SCIIB output thus becomes

$$\begin{aligned} s' &= r(SOP)s \\ &= r(SOP)\alpha\left[1 - \gamma \cos\left(\frac{4\pi}{\lambda}L\right)\right] \end{aligned} \quad (5-30)$$

As indicated in Eq. (5-30), the change in SOP will directly cause a normalized measurement error which can be calculated as

$$\frac{\Delta s}{s} = r(SOP) - 1. \quad (5-31)$$

From Figure 5.9, the maximum deviation of  $r(SOP)$  from its desired value (1:1) can reach 10% if the SOP of the light input to the beamsplitter changes from one polarization ( $p$ ) to another ( $s$ ). Therefore, the change of SOP can potentially introduce a normalized measurement error as large as 10%.

**Polarization of single-mode fibers:** If the fiber is perfectly circular with a circularly symmetric refractive index distribution, the two  $LP_{01}$  (or  $HE_{11}$ ) modes will perfectly degenerate, *i.e.* both x-polarized ( $E_y=0$ ) and y-polarized ( $E_x=0$ )  $LP_{01}$  modes will have the same propagation constant. However, actual fibers generally exhibit some ellipticity of the core and/or some anisotropy in the refractive index distribution due to anisotropic stresses. This results in two different propagation constants for the x-polarized ( $\beta_x$ ) and y-polarized ( $\beta_y$ )  $LP_{01}$  modes, leading to perturbations of the state of polarization of the light transmitted by the fiber. The birefringence of the fiber ( $\Delta\beta$ ) is usually defined as

$$\Delta\beta = \beta_y - \beta_x. \quad (5-32)$$

Singlemode fiber in a bent configuration can be viewed as a wave plate with its phase delay unknown due to the random number of bends and the random value of bending radius when the fiber is deployed into an oil well. For a linearly polarized input light, the SOP of the output light can thus be arbitrary (linearly polarized in any possible direction, circularly

polarized, or elliptically polarized). To be conservative, the maximum estimated error of 10% as given by Eq. (5-31) is valid for the entire case.

### 5.1.2.3 Noise Summary

In the two previous sections, the electronic and the optical noise sources of the SCIIB sensor system were studied in detail. Typical values for the induced error are summarized in Table 5.3 for comparison. The electronic noise is very small compared to the optical noise. Therefore, the emphasis of system optimization was placed on improvement of the optical system. Among the 4 categories of optical noise, change in SOP has the most significant effect on the system performance. Noise resulting from residual interference in the reference channel and noncentered filtering can also be reduced by the proper system design. However, temperature dependence of the optical bandpass filter is an almost fixed error for which little can be done due to the limited commercial availability of the components.

**Table 5.3. Typical electronic and optical noise for the SCIIB sensor system.**

Noise sources	Typical Values
<b>Electronic noise</b>	0.00115%
<b>Optical noise</b>	
1. Spectral drift of the optical bandpass filter	0.8% (from -15°C to 55°C @ $L_0 = 25\mu\text{m}$ )
2. Residual interference in the reference channel	0.0458% (0.5nm wavelength drift @ $L_0 = 25\mu\text{m}$ )
3. Noncentered filtering	0.0213% (0.5nm wavelength drift)
4. Change of SOP	10%

### 5.1.2.4 Optical System Optimization

#### Residual interference in the reference channel

As indicated in Eq. (5-22), the measurement error resulting from the residual interference in the reference channel is proportional to the fringe visibility of the residual interference ( $\gamma_r$ ), which is inversely proportional to the initial sensor cavity length. Therefore, increasing the initial sensor cavity length will help to reduce the residual fringe visibility in the reference channel and hence reduce the corresponding measurement error.

On the other hand, Eq. (5-22) reveals that the measurement error is also proportional to the initial cavity length ( $L_0$ ). The longer the initial sensor cavity, the larger the measurement error. Therefore, the smallest measurement error will result from the balance between these two effects. In order to find an optimal initial sensor cavity length, several sensors with different cavity lengths were made. The experimental results and the theoretical simulation as shown in Figure 4.3 through Figure 4.7 indicate that the visibility of the residual interference in the reference channel decreases very quickly as the cavity length increases before it reaches  $20\mu\text{m}$ . However, after  $25\mu\text{m}$ , the visibility decreases very slowly as the sensor cavity length increases. Therefore, a sensor cavity length of  $25\mu\text{m}$  was selected.

### Reduction of the non-centered filtering induced error

As shown in Figure 5.6, the measurement error is proportional to the offset between the center of the optical bandpass filter and that of the source spectrum. A closer match of the two center wavelengths will reduce the measurement error. The optical bandpass filter was rotated by an angle of about  $10^\circ$  from the normal incidence in which it was installed in order to reduce the mismatch between the two center wavelengths to within 0.5nm. The corresponding measurement error was estimated to be reduced from 0.0213% to 0.0035%.

### Reduction of the change of SOP induced error

A change in SOP can cause a large measurement error mainly through the residual polarization sensitivity of the beamsplitter used in the SCIIB system. Due to the limitation of the technology used in making the beamsplitter, it is difficult to find a beamsplitter with a splitting ratio purely independent of the state of polarization of the input light. However, if the input light is totally unpolarized natural light, even using a polarization-sensitive beamsplitter, the splitting ratio can be maintained constant and the polarization issue will not be a concern at all. This led us to use a depolarizer to minimize the SOP induced error.

By definition, a depolarizer is an optical device that transforms polarized (or partially polarized) light into naturally unpolarized or depolarized light. The Loyt depolarizer is made of two optical crystals ( $L_1$  and  $L_2$ ) cut from the same material. The neutral lines of crystal  $L_2$  are aligned perfectly with the bisectors of the neutral lines of  $L_1$ . These two optical crystals can be characterized by the optical phase delays  $\delta_1$  and  $\delta_2$ . If the optical conditions of the two crystals satisfy 1) the phase lag of the first crystal is larger than the coherence length  $L_c$  of the light, and 2) the second crystal ( $L_2$ ) is more than twice as thick as the first one ( $L_1$ ). If these two conditions are satisfied, the light emerging from the Loyt depolarizer will be effectively unpolarized when it is seen by a wide-spectrum detector.

All the above discussions suggest that if a Loyt depolarizer can be installed immediately preceding the beamsplitter, so that the beamsplitter and the photodetectors behind effectively see unpolarized light emerging from the depolarizer no matter how the state of polarization changes in front of the depolarizer. Thereafter the splitting ratio of the beamsplitter becomes insensitive to the polarization disturbance associated with the fiber bending or other causes. In our system, an optical fiber-based Loyt depolarizer, which has two polarization maintaining fibers replacing the two optical crystals described above, was used. The optical fiber Loyt depolarizer, made by the Noah Industries, Inc., has an extinction ratio of 20dB (100:1). The change of SOP induced measurement error was estimated to be reduced from 10% to 0.1% by.

To evaluate the effectiveness of the depolarizer, the SCIIB instrumentation was first tested without the depolarizer. Again, the system was tested without the sensor probe and the signal was directly from the reflection of the fiber endface. To change the SOP, we bent the fiber into a circle of different radii and flipped the fiber circle to different orientations. The two SCIIB channel outputs were recorded using an oscilloscope as shown in Figure 5.10. The ratio of these two outputs are plotted in Figure 5.11. It was evident that the two channel outputs were sensitive to the change of SOP, and moreover, they did not follow each other

due to the polarization effect. The peak-to-peak variation in this case was about 5% of the average ratio.

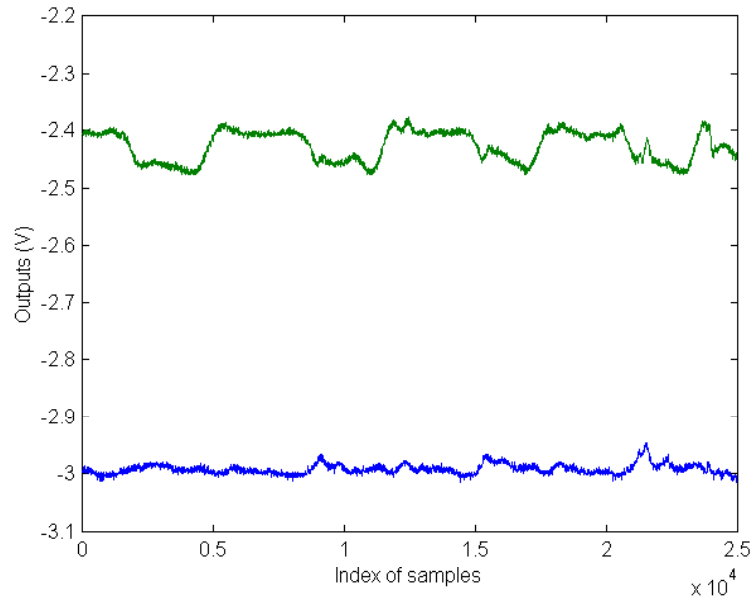


**Figure 5.10. Both SCIIB channel outputs as SOP of the fiber changes (without the depolarizer).**

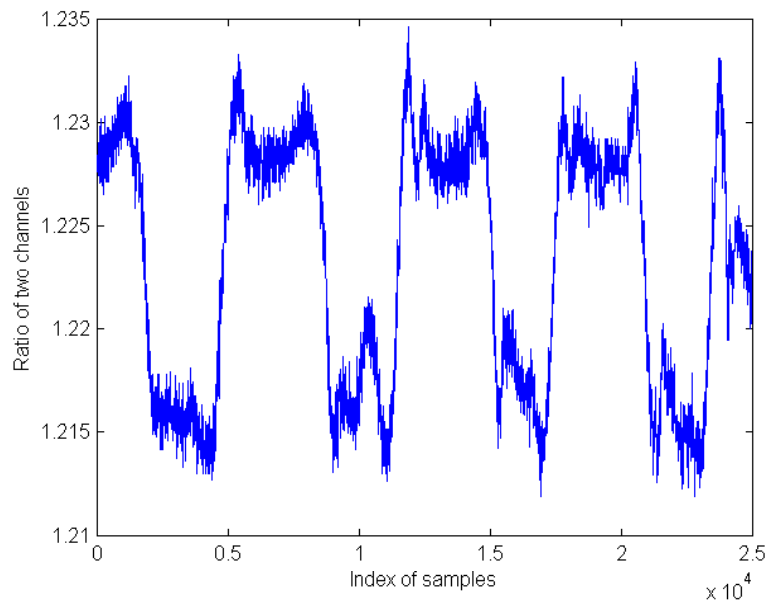


**Figure 5.11. Ratio of the two SCIIB channel outputs as SOP of the fiber changes (without the depolarizer).**

The experiment was repeated with the depolarizer connected to the system. Both channel outputs are shown in Figure 5.12, and their ratio in Figure 5.13. With the fiber optic depolarizer, the two outputs followed each other very closely. The maximum variation of the ratio was reduced to about 0.5%, showing an improvement of one order of magnitude. However, the experiment also indicated that the dependence of the SCIIB ratio was still large compared to the analytical prediction. The fiber optic Lyot depolarizer purchased from Noah

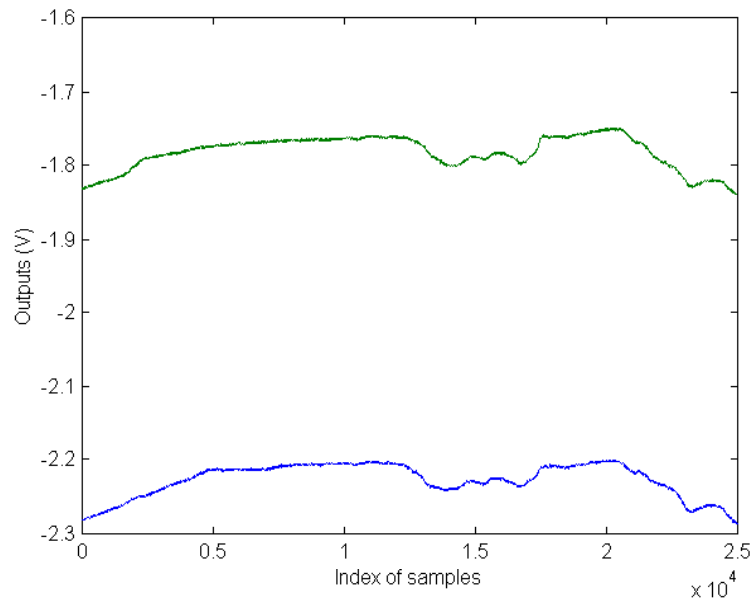


**Figure 5.12. SCIIB channel outputs as SOP of the fiber changes (with the depolarizer).**

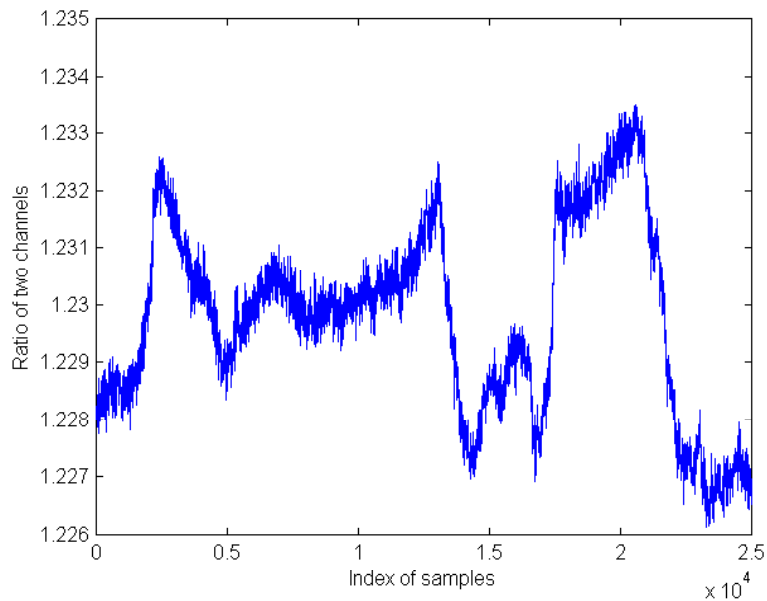


**Figure 5.13. Ratio of the two SCIIB channel outputs as SOP of the fiber changes (with the depolarizer).**

Industries, Inc. was then tested using a wide-spectrum light source. The optical bandpass filter used in the system had a spectral width of 10nm, which was narrower than the spectral width of the light source that had been used to test the depolarizer. The specified 20dB extinction ratio of polarization suppression might not be true for the signal channel. Therefore, we would expect to have larger polarization dependence of the SCIIB output ratio than the analytical prediction.

#### 5.1.2.5 Other System Optimization Measures

In addition to the electronic and optical noise sources discussed in Sections 5.1.2.1 and 5.1.2.2, other sources of errors could potentially affect the system performance. These include the dark current induced bias and the nonlinearity caused by the unmatched electronic amplifiers. Methods to minimize the errors resultant from these two are presented in this section.

#### Correction for the dark current induced bias

The dark current of the photodetector will add a constant bias to the photocurrent of interest. Although the dark current of the InGaAs detector used in the SCIIB system is very small (on the order of 15 pA), the resultant bias can affect the measurement result to some extent due to the relatively low optical power reflected from the sensor probe. To investigate the dark current induced error, let's assume that the signal currents of the two channels are  $I_{p1}$  and  $I_{p2}$  with the corresponding the dark currents of  $I_{d1}$  and  $I_{d2}$  respectively. The SCIIB ratio can thus be written as

$$s' = \frac{I_{p1} + I_{d1}}{I_{p2} + I_{d1}} = \frac{I_{p1}}{I_{p2}} + \frac{I_{d1}}{I_{p2}} + O^2, \quad (5-33)$$

where  $O^2$  is the second or higher order terms of  $I_{d1}$  and  $I_{d2}$ , which will be neglected from the analysis. The corresponding deviation from the ideal output ratio is

$$\Delta s = s' - s \approx \frac{I_{d1}}{I_{p2}}. \quad (5-34)$$

Therefore, the normalized error resulting from the dark current bias within the linear range of operation becomes

$$\frac{\Delta s}{s} = \frac{I_{d1}/I_{p2}}{I_{p1}/I_{p2}} = \frac{I_{d1}}{I_{p1}}, \quad (5-35)$$

where,  $I_{p1}$  should be confined in the linear operating range of the system.

The normalized error is plotted as a function of the normalized signal level in Figure 5.14, where the average signal current is assumed to be 54.7nA and the dark current is 15pA. As shown in the figure, the measurement error resulting from the dark current bias can reach 0.07% when the signal level is low (close to the valley of the interference fringe).

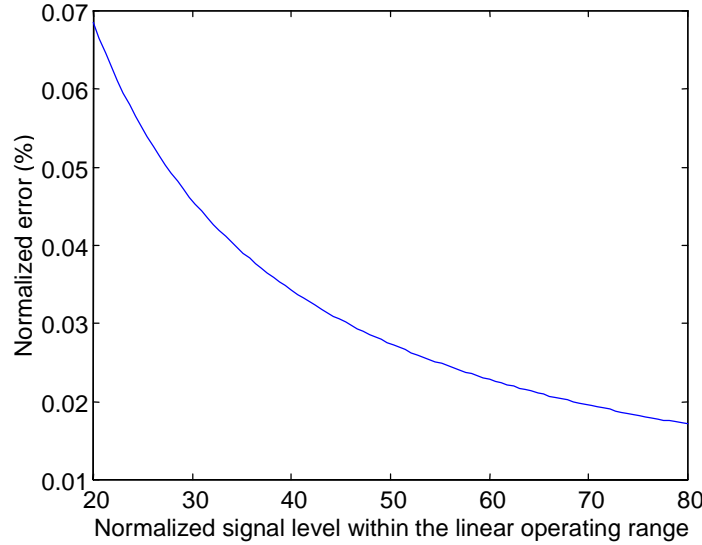


**Figure 5.14.** Normalized measurement error resulting from the dark current bias.

Because the final ratio function is performed digitally by the host computer, the correction of the dark current bias becomes relatively easy. We can record in advance the output voltage of the two SCIIB channels when the optical source is turned off. The dark current is almost a constant when the photodetector is chosen. Therefore, the dark current bias can be eliminated from the final ratio using

$$s = \frac{V_1 - V_{d1}}{V_2 - V_{d2}}, \quad (5-36)$$

where  $V_1$  and  $V_2$  are the output signal voltages, and  $V_{d1}$  and  $V_{d2}$  are the recorded dark-current voltages of the two channels respectively.

#### Balancing the optical power of the two channels

Because of the very large amplification factors of the transimpedance amplifiers used in the SCIIB system, the nonlinearity of the amplifiers could be a concern. However, the nonlinearity of the amplifiers can be compensated if the two amplifiers are exactly the same. Another reason to match these two amplifiers is the temperature dependence consideration. The resistance of the feedback resistors used in the transimpedance amplifiers will change as the environmental temperature fluctuates. If they change in the same direction and in the same amount, by taking the ratio of the two outputs, the temperature fluctuation will have very little effects on the system output.

To be able to match the two transimpedance amplifiers, we need to balance the optical power input to the two photodetectors. Because an optical bandpass filter is used in the signal channel to increase the coherence length, the signal channel will see less optical power than the reference channel. In order to balance the two channels in terms of the optical power, an optical neutral density filter can be inserted into the reference channel with a flat spectral response within the spectral range of interest, which introduces additional attenuation to the optical intensity of the reference channel.

### 5.1.2.6 Thermal dependence of the SCIIB instrumentation

The most important environmental disturbance to the measurement system is the temperature fluctuation. Changes in the environmental temperature could have multiple effects on the SCIIB instrumentation system. The spectrum of the light source, the spectral characteristics of the optical bandpass filter, the beamsplitter, the amplifiers and the photodetectors are all temperature dependent. However, if the thermal characteristics of the entire system are repeatable, they can be compensated for by using a temperature sensor. In this section, both a theoretical analysis and experiment results for the SCIIB system thermal characteristics are presented.

The experimental setup is shown in Figure 5.15 was used in the temperature experiments. The entire SCIIB system, except the FABRY-PEROT sensor head and connecting fiber, was placed inside a resistance heated electrical furnace (Blue M inc. Type 60406). In this way, the temperature dependence of FABRY-PEROT sensor head and the temperature dependence of the SCIIB system could be studied separately. Although the electrical furnace itself has a temperature output, to realize a high-resolution measurement, a thermocouple was put inside the electrical box of the SCIIB system. The outputs from the thermocouple and the SCIIB system were sampled by a 22 1/2 bit A/D converter. A notebook computer was used to store and analyze the experimental results. The optical spectrum reflected from the endface of a bare fiber is far different from that reflected from a Fabry-Perot sensor. In the case of a bare fiber, the reflected spectrum will be same as that of the light source, which approximates a Gaussian profile. When connected with a Fabry-Perot sensor, a reflected interference spectrum is expected. To obtain more useful information, the temperature experiments were conducted under two different conditions: 1) only a bare fiber was connected with the SCIIB system, and the end-face of the fiber was cut by a cleaver to obtain a 4% reflection; 2) a Fabry-Perot sensor was connected to the SCIIB system.

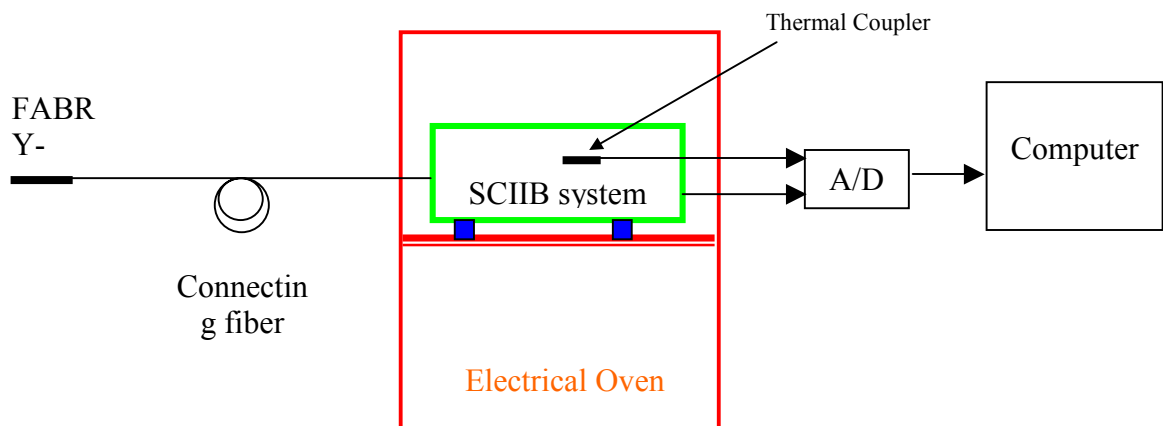


**Figure 5.15. Experimental setup for SCIIB thermal testing.**

Condition one: (no sensor connected)

The temperature of a recirculating drying oven (with the SCIIB system inside) was increased to about 40°C. To ensure that a uniform temperature distribution inside the whole system was achieved, the oven was maintained at 40°C for about one hour. Then the power was shut off to the oven, and the SCIIB system was allowed to cool down very slowly. Both the output from the SCIIB system and that from the thermocouple were sampled during this period. The signal transmitting path is shown in Figure 5.16 to assist in the analysis of the temperature characteristics of reference channel

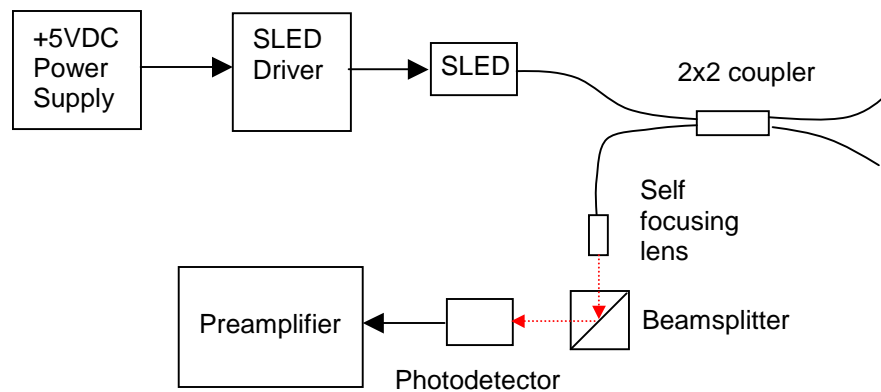


**Figure 5.16. Reference channel signal transmitting path.**

The temperature dependence of each component is described as follows.

- a. Power supply: A +5V regulated power source (AAK Corporation) was used in the SCIIB system as the power supply for both the amplifier and the SLED driver. The temperature coefficient of this product is about 0.015% per °C. Because both the SLED driver and amplifier have a large compliance voltage range, the temperature dependence of the power supply can be neglected.
- b. SLED driver: A PLD-200 laser diode driver (Wavelength Electronics Inc.) was used to supply a very stable current for the light source. The temperature coefficient of the driver is about 0.01% per °C. The drift of the output power of light source can be eliminated when the ratio of two channels is calculated.
- c. Light source: The light source used in the singlemode fiber-based SCIIB system is a high power superluminescent light emitting diode (SLED) provided by Anritsu Corp. (AS3B281FX), with a center wavelength of 1312 nm, a spectral width of 41.5 nm, and a maximum output power of 1.21mW from a 9/125 $\mu$ m pigtailed singlemode fiber. Figure 5.17 shows the source spectrum measured by an Ando Optical Spectrum Analyzer (OSA). The center wavelength shifts with temperature changes. In general, the temperature-induced drift

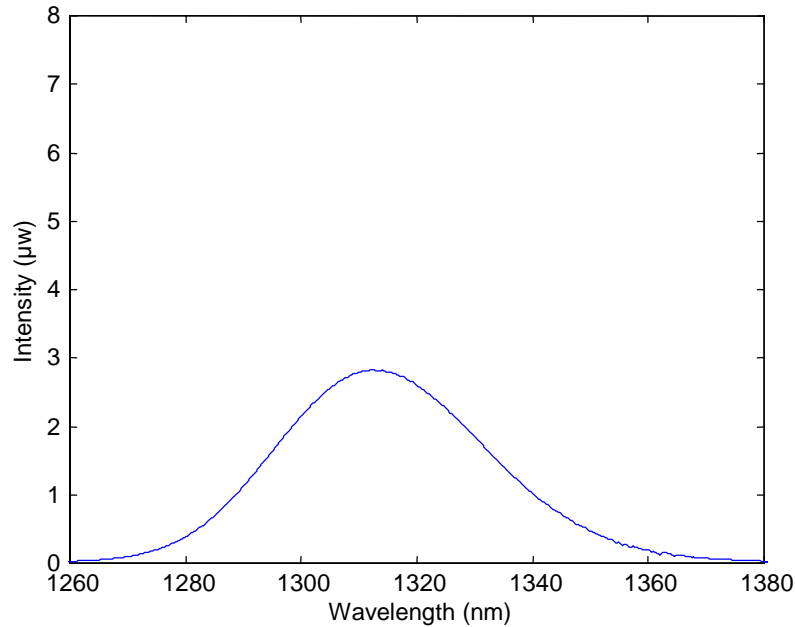


**Figure 5.17. Output spectrum of the SLED (Ando OSA).**

is about 0.2-0.3nm per °C. This will obviously induce errors in the interferometric-based measurement system. To increase the stability of the whole system, a TEC was used to control the temperature of the SLED.

d. Optical alignment: The received light signal will be collimated by a self-focusing lens, pass through a beam splitter and then be coupled into a TO-packaged large area photodetector. All optical components are installed inside a small aluminum box. The total length from the self-focusing lens to the active area of the photodetector is about 20mm. When the temperature changes, the status of alignment will change slightly, which will induce errors in the measurement results. However, it is difficult to predict how the status of the alignment changes with temperature, or if the self-calibration can work or not. All these had to be resolved based on the experimental results.

e. Photodetector: The singlemode SCIIB system works at 1300nm. A large effective area InGaAs photo-detector was used to provide a high response in this spectral range. Again, both the dark current and the responsivity of the InGaAs detector are functions of temperature. The compensating technique works only when two channels have exactly the same temperature dependence, which is almost impossible in reality.

f. Preamplifier: The electronics for the preamplifier are very simple: a transimpedance amplifier was employed to convert the photocurrent from the photo detector to a voltage output. The schematic of the circuit is shown in Figure 5.18. The stability of this amplifier is mainly decided by the feedback resistor R1 and the operational amplifier AD795. The feedback resistor is type MK lead precision power resistor (CADDOCK). Its temperature coefficient is about 0.008% /°C. The AD795 is a low noise, precision, FET input operational amplifier. It offers both the low voltage noise and low offset drift of a bipolar input op amp

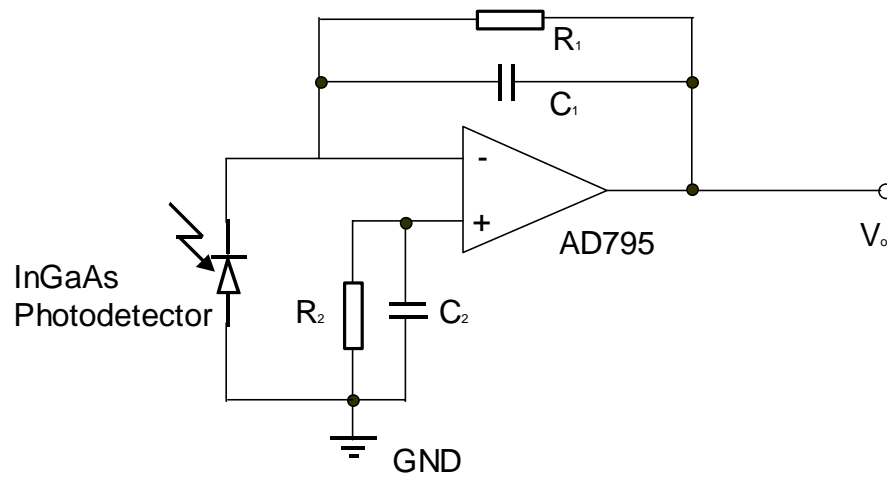


**Figure 5.18. Schematic of the preamplifier.**

and the very low bias current of a FET-input device. The  $1014\Omega$  common-mode impedance insures that the input bias current is essentially independent of common-mode voltage and supply voltage variations.

The experimental temperature dependence of the broadband channel, the narrow band channel and the ratio  $R$  are shown in Figure 5.19-Figure 5.21. Both the reference channel and the signal channel have large temperature dependence (in the temperature range of  $26-30\text{ }^{\circ}\text{C}$ , the drift is about  $0.5\%/^{\circ}\text{C}$ ), which can't be explained by the temperature characteristics of the separate components (most are on the order of  $0.01\%/^{\circ}\text{C}$ ). This maybe induced by the change in optical alignment. The curves in Figure 5.19 and Figure 5.20 are similar, which means part of the temperature dependence can be eliminated by calculating the ratio of the two channels. Figure 5.21 shows a monotonic decreasing relationship between the ratio  $R$  and temperature. The temperature dependence of the ratio  $R$  is due to the asymmetry between the two channels. The most important difference between the signal channel and the reference channel is the narrowband optical filter used in the signal channel. Other differences include: a different photodetector, different amplifier, and different optical path. The error induced by the optical filter is dependent on the spectrum of the receiving light signal, while the errors induced by other factors are insensitive to the spectrum. According to the experimental results described later, the temperature dependence of the SCIIB system is primarily due to the optical filter.

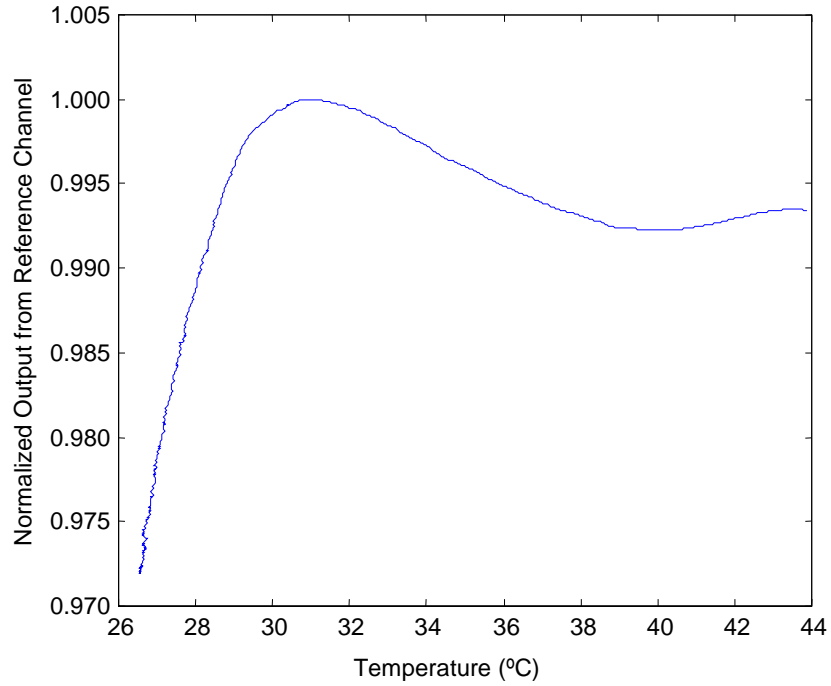


**Figure 5.19. Temperature dependence of the reference channel.**

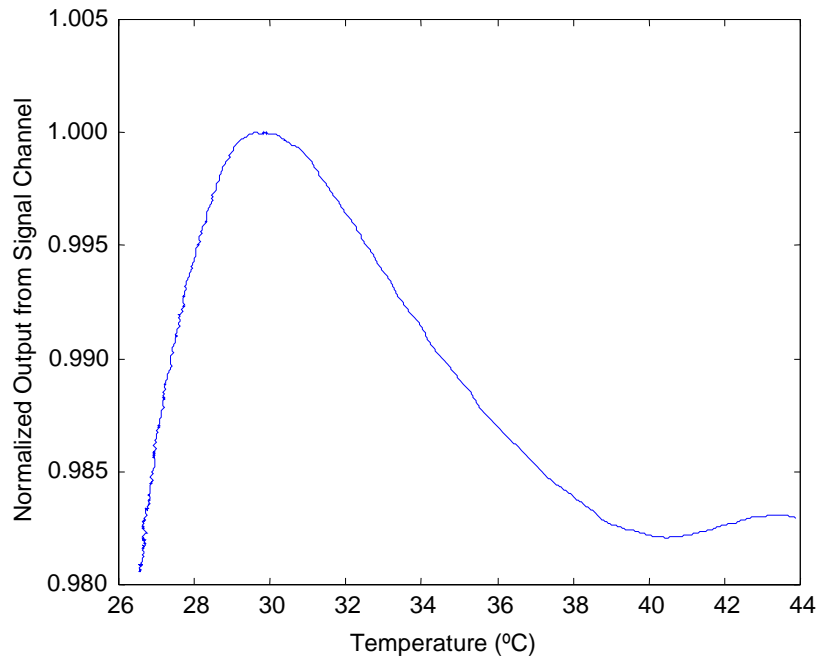


**Figure 5.20. Temperature dependence of the signal channel.**

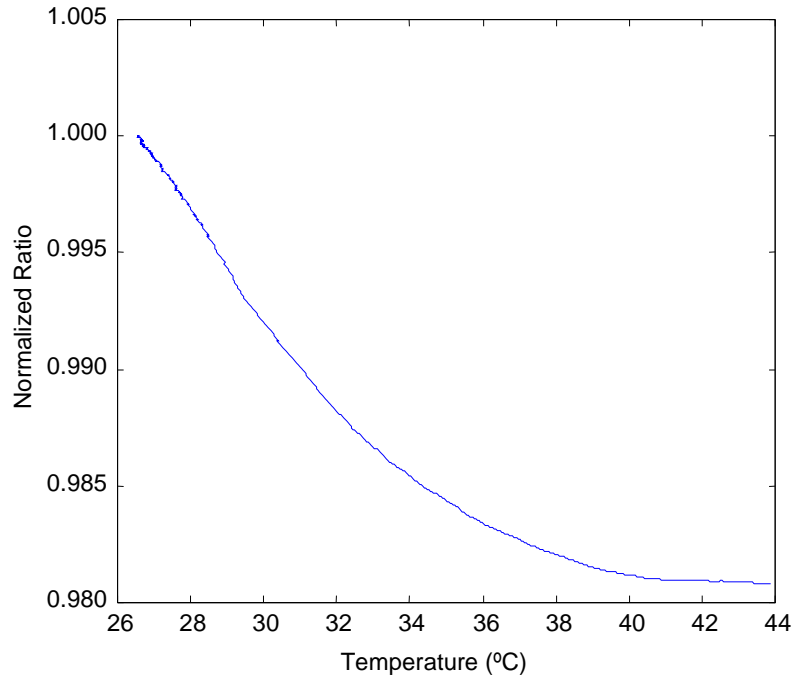


**Figure 5.21. Temperature dependence of the SCIIB ratio (signal channel / reference channel).**

As discussed above, the temperature dependence of the SCIIB system includes two parts: the first part is spectrum dependent; the second part is insensitive to the spectrum. The second part can be eliminated easily by using an optical switch in the system. Figure 5.22 shows the experimental setup of optical switch. A 1x2 optical switch (Ligtech fiber optics Inc.) was used in this experiment to eliminate errors induced by the asymmetry between Channel 1 and Channel 2. For spectrum-insensitive components like the photodetector (the bandwidth of the light source is only 60nm; in this range, the response of the detector can be treated as a constant.), amplifier, etc., this method works well. However, for spectrum sensitive components, like the optical narrowband filter, this method is of almost no use.

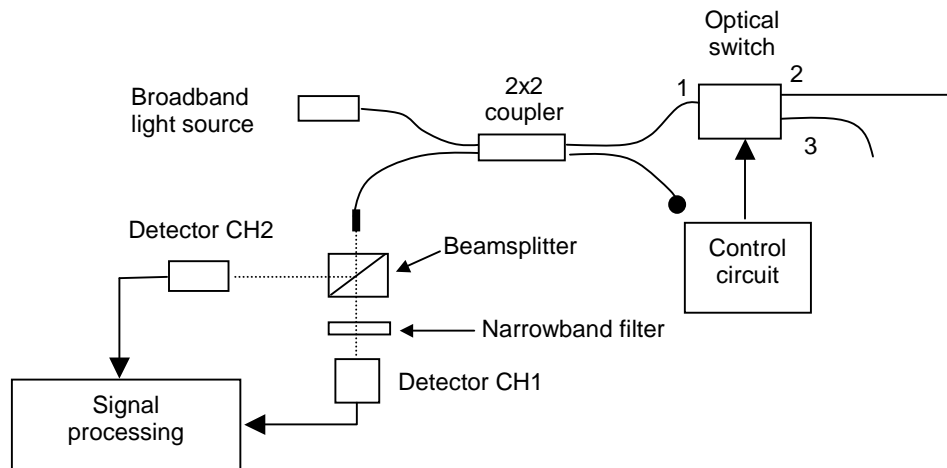


**Figure 5.22. Experimental setup to investigate the use of an optical switch to reduce the spectrum independent temperature dependence of the SCIIB system.**

In the first experiment, no FABRY-PEROT sensor head was connected in the system. Both Port 2 and Port 3 of the optical switch are connected to a standard 4% reflector (a polished fiber endface). Because the spectra of the reflected light from these two fiber endfaces are identical (same as the spectrum of the light source), all the errors induced by the asymmetry can be viewed as light spectrum insensitive. Under PC control, the optical switch is alternated between two status:  $1 \leftrightarrow 2$  or  $1 \leftrightarrow 3$ . The process can be described as follows.

The optical switch was first set at position one,  $S_{12}$ ; the received Channel 1 signal is

$$I_{s1} = K_1 L_1 I_{01}, \quad (5-37)$$

where  $I_{01}$  is the output power from the light source at the time when the data is sampled;  $L_1$  includes the effect of the reflector and the fiber loss;  $K_1$  includes the effect of the optical alignment loss, the photodetector and the amplifier in Channel 1.

Similarly, the received signal in Channel 2 can be described as

$$I_{s2} = K_2 L_1 I_{01}. \quad (5-38)$$

Therefore, in this situation, the ratio  $R_1$  is

$$R_1 = \frac{I_{s1}}{I_{s2}} = \frac{K_1}{K_2}. \quad (5-39)$$

If the two channels in the SCIIB system are matched perfectly, then  $K_1=K_2$ ,  $R_1=1$ , meaning the ratio will not change with temperature. Yet, based on the experimental results described above, this requirement cannot be satisfied.

The optical switch was then set at position two,  $S_{13}$ , the two received signals and their ratio can be expressed as

$$I_{R1} = K_1 L_2 I_{02}. \quad (5-40)$$

$$I_{R2} = K_2 L_2 I_{02}. \quad (5-41)$$

$$R_2 = \frac{I_{R1}}{I_{R2}} = \frac{K_1}{K_2}. \quad (5-42)$$

To eliminate the error induced by the asymmetry between  $K_1$  and  $K_2$ , the ratio of  $R_1$  and  $R_2$  must be calculated:  $R=R_1/R_2$ . The optical switch experiment results are shown in Figure 5.23. The  $R_1$  and  $R_2$  curves match each other almost perfectly, and the final ratio  $R$  shows almost no change, and therefore, is insensitive to temperature. Therefore by introducing an optical switch into the SCIIB system, a portion of the temperature dependence can be eliminated.

#### Condition two: (with sensor connected)

The optical switch works well when no sensors are connected with the system; however, when the SCIIB system is connected to a Fabry-Perot sensor head, the situation is much different. The critical component is the narrowband optical filter. Because the light spectrum reflected from a Fabry-Perot sensor is much different from that reflected from a reflector, the

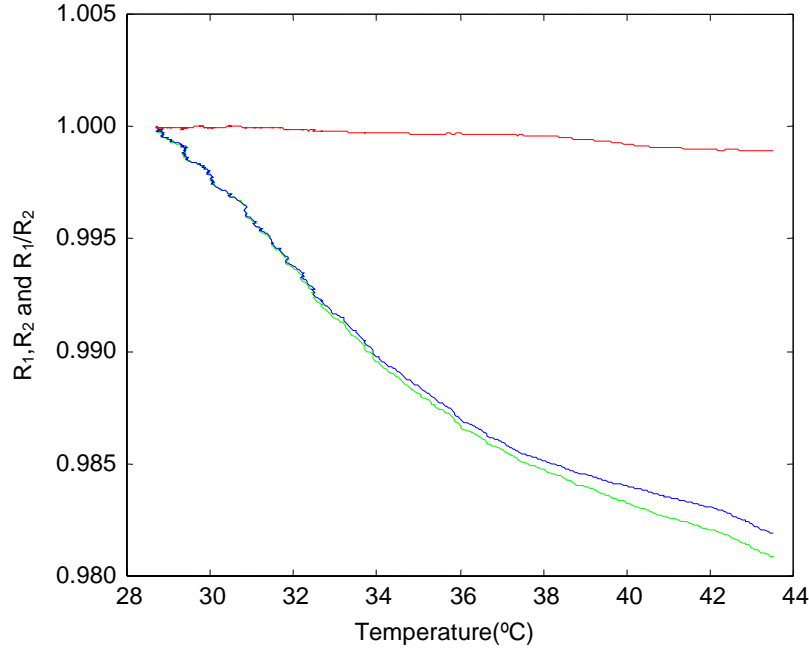


**Figure 5.23. Optical switch experimental results (Green line— $R_1$ ; Blue line— $R_2$ ; Red line— $R$ ).**

errors induced by the optical filter are different in these two conditions. It's difficult to use the signal from the fiber endface to compensate the signal from a sensor head.

Figure 5.24 shows the normalized spectrum from a Fabry-Perot sensor and from a polished fiber endface. The dashed black line indicates the operating point of the SCIIB system (the ideal center wavelength of the optical filter). When temperature increases, the center wavelength of the optical filter will move to longer wavelengths due to the thermal expansion. These two curves describe how the output of the SCIIB system changes when the center wavelength of the optical filter drifts. Because the slopes of the two curves are very different near the operating point, the induced output errors are also different. In fact, if the center wavelengths of the optical filter and the light source are matched perfectly, the slope of the Gaussian function near the operating point is almost zero, which means only slight errors are produced when a fiber endface is used as the reflector. On the other hand, when a Fabry-Perot sensor is connected in the system, the slope of the received spectrum near the operating point is very large, and the slope will change with the air-gap (or the physical parameter to be measured). The maximum error induced by the optical filter wavelength drift can be described as:

$$\frac{\delta s_{\max}}{\Delta s_{\max}} = \frac{\gamma \frac{4\pi L}{\lambda^2} \delta \lambda}{1.6\gamma} = \frac{4\pi L}{1.6\lambda^2} \delta \lambda. \quad (5-43)$$

In general, the air gap  $L$  is about 10000nm, the wavelength is about 1300nm, the temperature dependence of the optical filter is about 0.02nm/°C. So, the error induced by the drift of the optical filter is about 0.1%/°C.

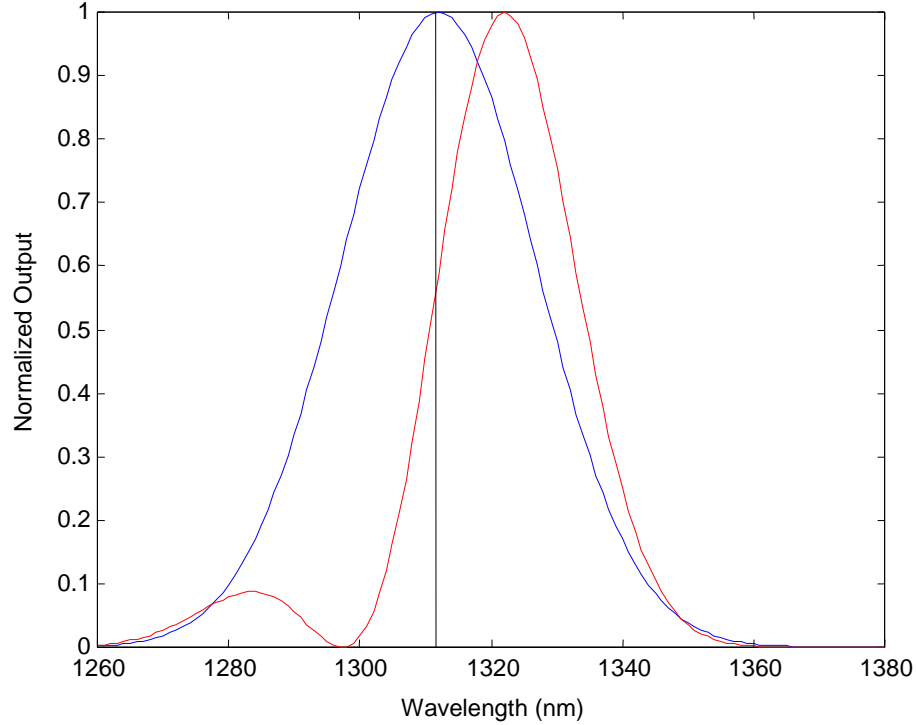


**Figure 5.24. Light spectrum reflected from a Fabry-Perot sensor (Red line, the initial air gap of the sensor head is 12000nm); blue line, that from a polished fiber endface).**

Figure 5.25 shows the experimental results when a Fabry-Perot sensor head was connected in the system. In this case, the temperature characteristics of the sensor path (optical switch was in position one, the SCIIB system was connected with a Fabry-Perot sensor) is different from that of the reference path (optical switch was in position two, the SCIIB system was connected with a polished fiber end-face.) The use of an optical switch makes the temperature dependence even worse. To decrease the temperature dependence of the SCIIB system, another approach is to use a standard temperature sensor to measure the temperature inside the SCIIB system (especially the temperature of the optical filter). Without losing universality, the output of SCIIB system can be simplified as

$$R = \frac{1}{2} \left( 1 + \cos\left(\frac{4\pi L(P)}{\lambda(T)}\right) \right). \quad (5-44)$$

Here a Fabry-Perot pressure sensor head was used ( $L(P)$ ), and the center wavelength of the optical filter  $\lambda(T)$  is a function of temperature. Differentiating the above equation; the change on  $R$  can be expressed as

$$\begin{aligned} \Delta R &= -\frac{4\pi}{\lambda} \sin \frac{4\pi L}{\lambda} \Delta L(P) + \frac{4\pi L}{\lambda^2} \sin \frac{4\pi L}{\lambda} \Delta \lambda(T), \\ &= K_1(P) \Delta L(P) + K_2(P) \Delta \lambda(T) \end{aligned} \quad (5-45)$$

where

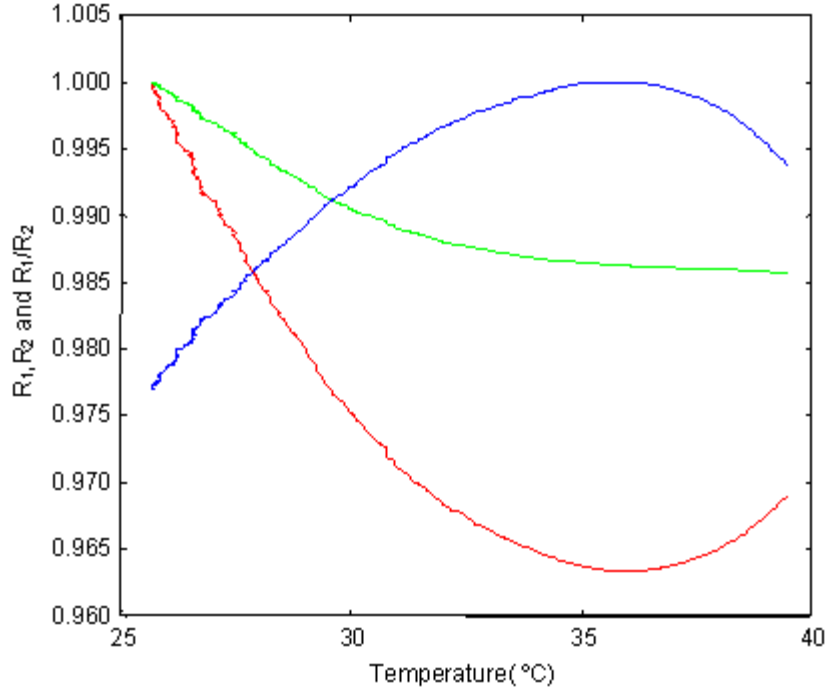


**Figure 5.25. Experimental results from the FABRY-PEROT sensor (Green line—Sensor Path  $R_1$ ; Blue line—Reference Path  $R_2$ ; Red line— $R=R_1/R_2$ ).**

$$K_1(P) = -\frac{4\pi}{\lambda} \sin \frac{4\pi L}{\lambda}$$

$$K_2(P) = \frac{4\pi L}{\lambda^2} \sin \frac{4\pi L}{\lambda}$$

The first item on the right side provides the pressure sensitivity of the SCIIB system; the second item shows how the system output drifts with the temperature. Compared with the center wavelength itself, the wavelength drift of the optical filter is very small, so  $\lambda$  can be treated as a constant. Both  $K_1$  and  $K_2$  are functions of the air gap  $L$  (the pressure to be measured), which means when the pressure changes, the relationship between  $R$  and  $T$  also changes. This makes compensation of the ratio  $R$  complicated. The form of the equation can be changed to

$$\Delta R = K_1 \left( \Delta L - \frac{L}{\lambda} \Delta \lambda \right)$$

$$\Delta P \Leftrightarrow \Delta L \Leftrightarrow \frac{\Delta R}{K_1} \Leftrightarrow -\frac{L}{\lambda} \Delta \lambda \quad (5-46)$$

Compared with  $L$  (10000nm), the change  $\Delta L$  (about 200nm) is pretty small;  $L/\lambda$  can be considered as a constant, so  $\Delta L$  (or  $\Delta P$ ) is linearly dependent on  $\Delta \lambda$  ( $\Delta T$ ). Instead of compensating  $R$  with  $T$ , we can compensate pressure  $P$  with  $T$  directly.

A thermal resistor was placed inside the SCIIB system just beside the optical filter, and the whole system was put inside the electrical oven. A Fabry-Perot sensor outside the oven was connected to the system through 1km of singlemode fiber. The temperature of the oven first was increased to about 40°C, and then decreased to room temperature (about 25°C). Figure 5.26 shows the output of the SCIIB system and the thermal resistor during this period. The relationship of the ratio R and temperature T (here, we use the voltage output of thermal resistor directly) can be determined, as shown in Figure 5.27. To set up the relation between  $\Delta P$  and  $\Delta T$  ( $\Delta V$ ), the calibration curve of the sensor head must be acquired first, as shown in Figure 5.28. The temperature coefficient of the SCIIB system is then be expressed as

$$\frac{\Delta P}{\Delta V} = \frac{\Delta P}{\Delta R} \frac{\Delta R}{\Delta V}. \quad (5-47)$$

Based on the method discussed above, several sensors were tested. Yet, the residual errors were still greater than the requirements. The one-day stability level achieved was only about 0.1%. The residual errors come from several sources: the characteristics of some components will drift with time (aging process); the spectrum and the status of polarization changes induced by fiber bending, etc.

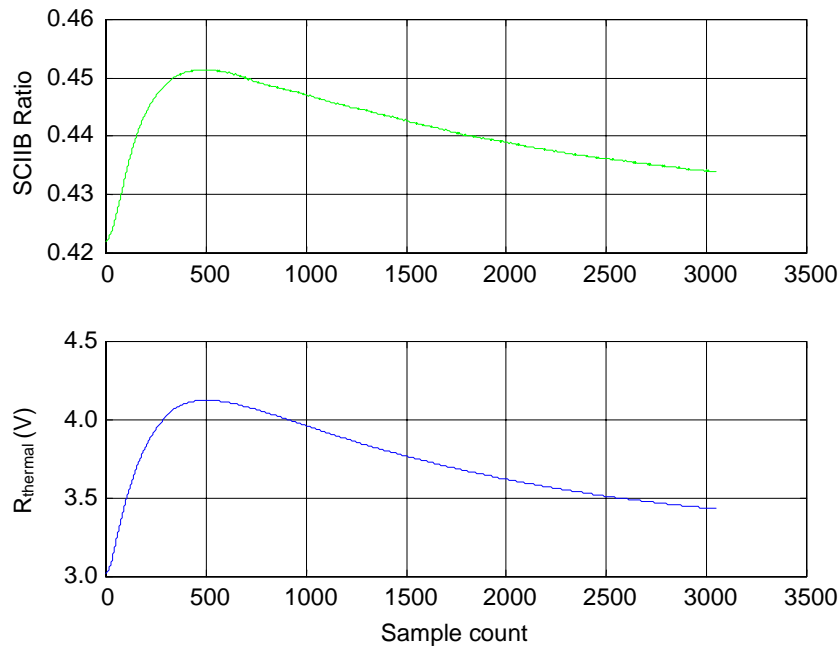


**Figure 5.26. SCIIB system temperature experiment (The X axis is time; The unit of the output from thermal resistor is volts).**

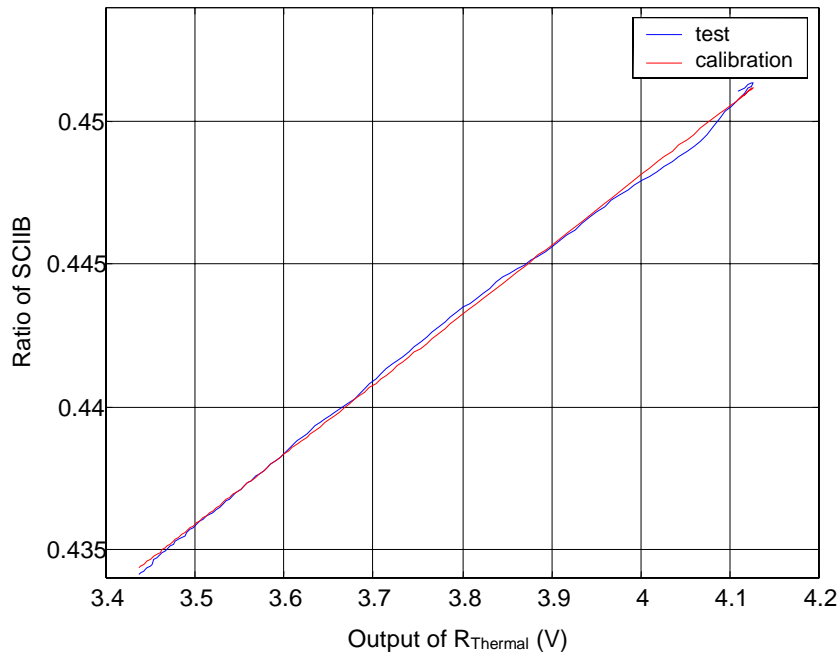


**Figure 5.27. Temperature dependence of the ratio R.**

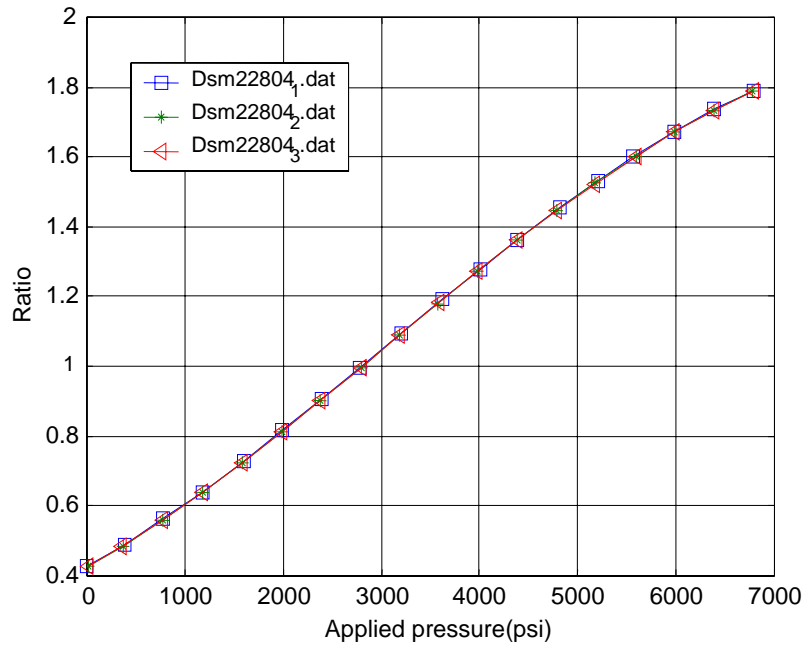


**Figure 5.28. Calibration curve of the sensor head.**

### 5.1.3 Other Proposed Signal Demodulating Structures

In parallel with the optimization of the SCIIB system, other signal demodulating structures were also considered, including the white light interferometer discussed in Section 5.2 and the dual-sensor structure described here. One of the major problems of the SCIIB system is the limited dynamic range, which is only about 200-300nm. If the required accuracy is 0.01%, then the accuracy of the air gap measurement needs to be 0.01nm, which is about one tenth of the size of an atom. A second problem is associated with the optical component performance. Most are sensitive to the spectrum or the state of polarization; the spectrum or polarization change induced by a long singlemode fiber is difficult to control. One possible solution for these problems is the dual sensor configuration shown in Figure 5.29.

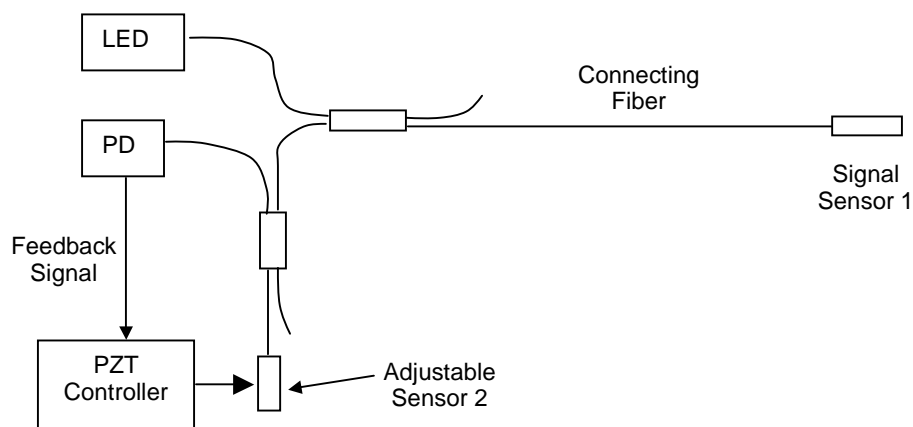


**Figure 5.29. Proposed dual-sensor structure design.**

Two FABRY-PEROT sensors were used in this system; the signal sensor is a normal FABRY-PEROT sensor, which is used to measure the pressure (or temperature) in the oil site. Another sensor, which is located in the electrical box, is used to trace the air gap of the signal sensor. The air gap of the inside sensor is controlled and measured by a commercialized PZT control system. The photodiode is used to measure the interference between Sensor 1 and Sensor 2. To obtain the maximum output from the PD, the two air gaps must be equal. When the air gap of the signal sensor changes, the output of the PD will decrease. Using the feedback signal from the PD, the PZT controller will adjust the air gap of Sensor 2 until it matches Sensor 1. The PZT controller measures Sensor 2's air gap at the balance point. In this system, the dynamic range of the air gap is determined by the PZT system. When the two air gaps are matched to each other, the signal received by the PD is always a global maximum. A commercialized PZT system can reach 1nm repeatability with tens of microns of dynamic range, so the potential accuracy of this system is better than 0.01%. Additional advantages of this structure include insensitivity to changes in polarization and light spectrum and ease of multiplexing. Positive preliminary results were obtained with this structure. However, due the enormous success achieved with the white light system, attention was focused on that area for the remainder of the program.

## 5.2 Signal Demodulation System II – White Light Interferometer

In parallel with the SCIIB system development, another interferometric-based fiber optic sensor system, the white light interferometer, was developed at CPT. The initial intent was to monitor the air gap of the FABRY-PEROT sensor during sensor fabrication. (The operating point of the SCIIB system is determined by the initial air gap of the FABRY-PEROT sensor head. To achieve the maximum dynamic range and sensitivity, the deviation of the air gap from the optimum point should be less than 10nm). During this process, several important breakthroughs were achieved by thoroughly studying the white light system. By combining elaborate hardware design with novel data processing methods, the system reaches sub-nanometer resolution with a 10  $\mu\text{m}$  dynamic range. The white light system was proven to be the best choice for high-resolution, low speed applications. In this section, the development of the white light interferometer system is detailed.

### 5.2.1 Principle of operation

White light or low coherence interferometry is a technique that dates back to 1913 and was reapplied to optical fiber sensing in 1983. In most conventional interferometric systems, high coherence light sources such as single line lasers are used to obtain a large coherence length. For such narrowband light sources, spectral measurements are impossible; only power measurements can be realized. For this kind of system, a tradeoff is required between absolute measurement and a large dynamic range. To achieve absolute measurement, the change in optical length must be limited to half the wavelength, just like in the SCIIB system. By using an fringe counting method, the potential dynamic range can be as large as the coherence length of the light source, but only the relative change of the optical path can be measured. When a long length of optical fiber is involved, the instability induced by the propagation of highly coherent light in the optical fiber also becomes an issue. To realize both absolute measurement and high resolution, the white light interferometer was developed. Instead of a highly coherent laser, a broadband light source, such as an LED, is used in this system. (That's where the terminology "white light" comes from, and in this sense, the SCIIB system also belongs to the white light system family.) Although power detection can still be used, to fully exploit the advantages of the white light source, spectrometer-based detection systems are more popular.

The white light interferometric fiber optic sensor system inherits most of the advantages from conventional interferometer, such as immunity to light source drift and change in transmission loss, high resolution, large dynamic range, etc. On another hand, the use of a long life, low price broadband light source (such as LED) improves the stability of the whole system dramatically. The basic structure of spectrometer-based white light system is shown in Figure 5.30. Similar to the SCIIB system, a Fabry-Perot sensor head is used to measure pressure or temperature. The broadband light source is an 850nm LED with a 60nm bandwidth. This kind of light source encompasses many virtues, such as high stability, long life, high efficiency, small size, low price, etc. A compact spectrometer fabricated by Ocean Optics Inc is used to measure the interference spectrum. The whole system is very compact and robust.

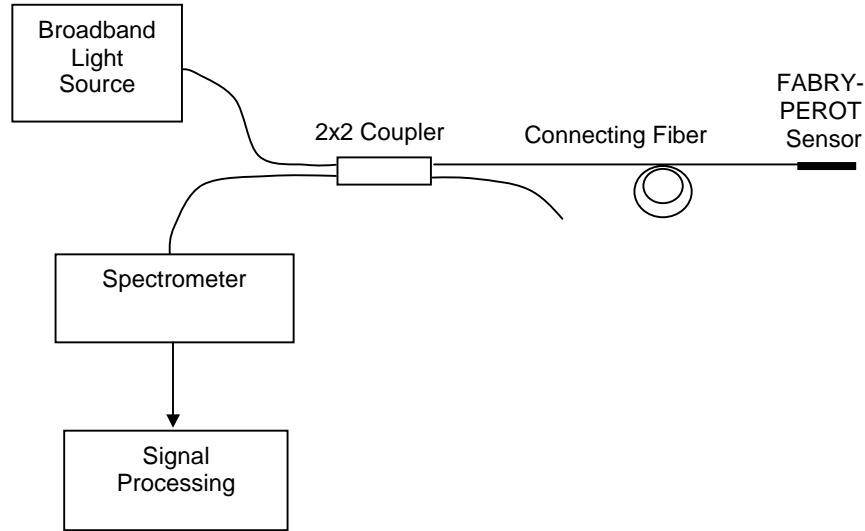


**Figure 5.30. Basic structure of interferometer-based white light system.**

The optical power output from the light source is launched into the connecting fiber through a 2x2 fiber coupler and propagates to the FABRY-PEROT sensor head. The light signal reflected from the sensor head travels back along the same fiber and is launched out to the one dimension CCD based interferometer from the other port of the 2x2 coupler. Then, the measured spectrum is transferred to PC for data processing. To obtain an interference spectrum with high visibility, the air gap cannot be greater than the coherence length of the system. In this system, the coherence length is primarily dependent on the spectral resolution of the spectrometer, the numerical aperture (NA) of the optical fiber and the quality of the FABRY-PEROT sensor head. In general, the coherence length in the white light system is larger than that of the SCIIB system.

The interference spectrum measured by the spectrometer is given by:

$$I(\lambda) = 2I_s(\lambda) \cdot (1 + \gamma \cos(\frac{4\pi G}{\lambda} + \varphi_0)). \quad (5-48)$$

where  $I_s(\lambda)$  is the spectral power distribution of light source,  $\gamma$  is the visibility of the interference spectrum,  $\varphi_0$  is the arbitrary initial phase difference,  $G$  is the air gap, which is determined by the physical parameter (such as pressure or temperature) to be measured. By normalizing Eq. (5-48) with respect to the Gaussian spectrum of the light source, the normalized interference output can be expressed as

$$I_n(\lambda) = 2(1 + \gamma \cos(\frac{4\pi G}{\lambda} + \varphi_0)). \quad (5-49)$$

The value of the air gap  $G$  can be calculated from Eq. (5-49) and then used to demodulate the physical parameter.

### 5.2.2 Novel data processing method

Various methods had been developed to demodulate the air gap  $G$  from the normalized spectrum using Eq. (5-49). Most of these can be grouped into two classes. The first class can achieve high resolution (which primarily depends on the resolution of spectrometer), but the dynamic range of the air gap must be limited in the half wavelength range; the second class can achieve a large dynamic range, yet only a low resolution achieved. The basis of these methods is discussed below.

#### 5.2.2.1 Class One

The first type of demodulation is based on locating a specific point in the interference spectrum (such as peak point or valley point). The value of air-gap can be demodulated from the wavelength of this point. The wavelength  $\lambda_m$  of a peak point in interference spectrum satisfies the equation

$$\frac{4\pi G}{\lambda_m} + \varphi_0 = m2\pi, \quad (5-50)$$

where the spectral order  $m$  is a non-negative integer.

Eq. (5-49) can be transformed into:

$$G = \frac{(m2\pi - \varphi_0)\lambda_m}{4\pi} = \frac{K_m}{2} \lambda_m \quad (5-51)$$

$$K_m = \frac{(2m\pi - \varphi_0)}{4\pi} = m - \frac{\varphi_0}{2\pi}$$

To demodulate the air-gap  $G$  from the wavelength  $\lambda_m$ ,  $K_m$  must be acquired first. The identification of the interference order  $m$  is so difficult that the unambiguous operating range of the air gap is limited to only half of the wavelength. The resolution of measurement result is primarily dependent on the resolution of spectrometer. From Eq. (5-51), the relative error of this system can be described as

$$\left| \frac{\Delta G}{G} \right| \cong \left| \frac{\Delta \lambda}{\lambda} \right|. \quad (5-52)$$

#### 5.2.2.2 Class Two

To realize absolute measurement, at least two special points in the interference spectrum must be used. In fact, there are 2048 pixels in the CCD detector of spectrometer, of which 1000 are located in the spectral range of the light source. The more information that is used, the higher the resolution that can be achieved. Suppose  $\lambda_1$  and  $\lambda_2$  ( $\lambda_1 > \lambda_2$ ) are the wavelengths of two adjacent peak points in the interference spectrum. Their interference orders are  $m$  and  $m+1$ . From Eq. (5-50):

$$\frac{4\pi G}{\lambda_1} + \varphi_0 = m2\pi. \quad (5-53)$$

$$\frac{4\pi G}{\lambda_2} + \varphi_0 = (m+1)2\pi . \quad (5-54)$$

The air gap  $G$  can be demodulated from

$$G = \frac{\lambda_1 \cdot \lambda_2}{2(\lambda_2 - \lambda_1)} . \quad (5-55)$$

Here, the dynamic range is only limited by the coherence of the white light system. In this case, the relative error induced by the spectrometer is

$$\left| \frac{\Delta G}{G} \right| \cong \sqrt{2} \left| \frac{\lambda_2}{\lambda_2 - \lambda_1} \right| \cdot \left| \frac{\Delta \lambda_1}{\lambda_1} \right| . \quad (5-56)$$

Compared to Class 1 (Eq. (5-52)), in Class 2 demodulation the relative error induced by the spectrometer will be enlarged by a factor of  $\sqrt{2} \left| \frac{\lambda_2}{\lambda_2 - \lambda_1} \right|$ . The center wavelength of the light source (LED) is 850nm. In the normal operating range (air-gap 5-15  $\mu\text{m}$ ), this factor  $\sqrt{2} \left| \frac{\lambda_2}{\lambda_2 - \lambda_1} \right|$  is about 15—50. So, this method has a large dynamic range but lower resolution.

### 5.2.2.3 New Algorithm

To combine the advantages of these two types of methods, a novel data processing method, which can realize both the high resolution and a large dynamic range, was developed at CPT. The basic idea is to use two peak points in the interference spectrum to obtain coarse air gap (large dynamic range is achieved); this coarse air gap is then used to determine the order number  $m$  and a rough  $K_m$  of a special peak point. Then, an accurate  $K_m$  will be recovered from the rough  $K_m$ . From Eq. (5-51), the accurate air gap can be calculated from the accurate  $K_m$  and the peak wavelength (high resolution is achieved).

If the coarse  $K_m$  is used directly, high resolution cannot be achieved. The technique used to recover the fine  $K_m$  is discussed here. In the equation  $G=K_m\lambda/2$ , although  $K_m$  is not an integer, for a given peak, it is a constant. And for adjacent peaks, the difference in  $K_m$  is 1. For example, if the  $K_m$  of one peak is 12.34, then, for other peaks, the  $K_m$  will be 13.34, 14.34, 15.34...and 11.34, 10.34, 9.34...

By calibration, the  $K_m$  value for a special peak ( $K_m^0$ ) can be acquired and stored in computer. When the coarse  $K_m$  value for any peak has been acquired, the fine  $K_m$  is then calculated from  $K_m^0$  by adding the integer part in the difference between the coarse  $K_m$  and  $K_m^0$ . The entire process of demodulating air gap  $G$  from the interference spectrum can be separated into two steps: the calibration process and the measurement process.

The calibration process is described as follows. With the white light interferometer system in a stable condition, set the air gap  $G$  to a known value  $G_0$  (or put the FABRY-PEROT sensor head in a given pressure environment). The  $K_m^0$  of a peak in the interference spectrum can be calculated from  $G_0$  and the wavelength  $\lambda_0$  of this peak. As long as the  $K_m^0$  is acquired, the measurement process can be carried out as follows.

1. Use two peak points in the interference spectrum to acquire a rough value of air gap  $G'$ .
2. Select a peak point near the center of interference spectrum and use the wavelength of this peak and the rough  $G'$  from the last step to calculate a rough  $K_m'$ .
3. The accurate  $K_m$  can be calculated from  $K_m'$  and the stored  $K_m^0$  from

$$K_m = K_m^0 + \text{int}(K_m' - K_m^0 + 0.5). \quad (5-57)$$

where function  $\text{int}(\dots)$  indicates the integral portion.

4. The accurate air gap  $G$  can be calculated from the accurate  $K_m$  and the wavelength of this peak by Eq.(5-51).

If the white system operates in a harsh environment, occasionally, an outside disturbance can introduce a large "jump" in the measuring result. The magnitude of these "jumps" are equal to half of the wavelength exactly. These "jumps" in the measured output are due to the inability of the spectral analyzer to resolve adjacent  $K_m$  values. As described in the discussion above, the low resolution  $G'$  value is used to determine the low resolution  $K_m'$  value. An error can occur in the determination of the low resolution  $K_m'$  value due to inaccuracies in the  $G'$  value. If this error is large enough this will result in shifting the  $K_m$  value by an integer number. This shifting of the  $K_m$  value by an integer number results in a calculated change in the air gap of an integer multiple of one half of the wavelength of the light source. When monitoring a physical parameter such as pressure, the observed result is that the pressure detected from the sensor appears to "jump" to a higher or lower value when indeed the real pressure has not changed. This "jump" can occur at any time during the operation of the system and appears in a more or less random fashion. In order to overcome this problem, another data processing method was used to monitor the value of the air gap calculated from the previous time interval. The new air gap value  $G_n$  calculated during the present time interval is compared to the air gap value  $G_0$  from the previous time interval:

$$\Delta G = |G_n - G_0|. \quad (5-58)$$

If the  $\Delta G$  value is larger than one half of the wavelength of the light source used, then the air gap will be modified according to:

$$\begin{aligned} G &= G_n - \frac{\lambda}{2} && \text{when } G_n > G_0 \\ G &= G_n + \frac{\lambda}{2} && \text{when } G_n < G_0 \end{aligned} \quad (5-59)$$

Therefore, when the condition is detected that  $G_n$  differs from  $G_0$  by more than one half of the wavelength, a new air gap  $G$  is calculated based on the formulas above. This new air gap  $G$  is then used to demodulate the physical parameter to be measured. The system checks for this condition during every measurement. In this manner, the jump problem has been completely eliminated.

This novel data processing method was realized in Visual Basic, and applied in the oil field. Its performance was confirmed by the experimental results.

### **5.2.3 Design and implementation**

Both singlemode and multimode white light systems were set up at CPT. A VB program, integrated functions of system control and data processing, were also developed. Details on the system setup and program development are presented in this section.

#### *5.2.3.1 Hardware design and system fabrication*

The most critical part of white light system is the spectrometer. The performance of the entire system, such as resolution and stability, are highly dependent on the performance of spectrometer. In a traditional spectrometer-based system where a cumbersome and expensive spectrometer is used, strict requirements on the environmental conditions exclude the use of this kind of instrument in the field. Here, a compact fiber optic spectrometer (USB2000 manufactured by Ocean Optics, Inc.) was used in the white light system. The input fiber is connected to the USB2000 directly through a SMA connector. Inside the spectrometer, a 1200 line holographic grating is used to diffract the input light on a 2048-pixel CCD array. The electrical signal output from each pixel can be read out serially. After conversion to digital format by a built-in A/D card, the measured spectrum can be transferred into a PC. The interface between the computer and the spectrometer is very flexible; Ocean Optics supports most of the common ports, including USB, ISA, etc. The key features of the USB2000 are listed in Table 5.4 below.

Both singlemode and multimode white light systems were built based on the USB2000 spectrometer. In the multimode system, the light source is an 850nm LED (Honeywell HEF 4857-014). In the singlemode system, a super-luminescent diode (SLED from EG&G Inc.) was used. To satisfy the requirements of different applications, a two-channel multimode system was also developed. Figure 3.2a and b shows the structure of single channel multimode white light system. The two channel multimode white light system is shown in Figure 3.3. The dual channel and single channel multimode systems are shown in Figure 5.32 and Figure 5.31, respectively.

### **5.2.4 Software design and program development**

Advanced computer software was developed to demodulate the air gap from the interference spectral signal. This program is based on the novel data processing method discussed in the previous section. The program is implemented in a combination of Visual Basic and C languages so that both graphic interfaces and high computational speed are achieved and optimized. A block diagram of the program is shown in Figure 5.33, and the program details are described in the remainder of this section.

#### *5.2.4.1 Initialization*

Hardware initialization includes initialization of the spectrometer, temperature measurement system (for compensation), etc. Then most of the important parameters, which are stored on the hard disc, will be restored to memory, including the parameters for setting up spectrometer, the  $K_0$  value, the reference spectrum of the light source, the dark current of the spectrometer, and the calibration curve of the FABRY-PEROT sensor head.

**Table 5.4. Key features of the Ocean Optics USB2000 fiber spectrometer.**

<b>Computer interface:</b>	Universal Serial Bus (RS-232 available on side connector)
<b>Spectrometer channels:</b>	One or two
<b>Integration time:</b>	3 milliseconds-65 seconds
<b>Data transfer rate:</b>	Full scans (2048 wavelengths) into memory every 13 ms OOIBase32 time acquisition approximately every 25 ms
<b>Dimensions:</b>	3.5" x 2.5"x 1.31" LWH 89 mm x 64 mm x 34 mm LWH
<b>Weight:</b>	0.45 lb. (200g) without cable 0.60 lb. with cable
<b>Detector:</b>	2048-element linear silicon CCD array
<b>Effective range:</b>	200-1100 nm
<b>Dynamic range:</b>	$2 \times 10^8$
<b>Sensitivity (estimate):</b>	86 photons/count
<b>Signal-to-noise:</b>	250:1 (at full signal)
<b>Dark noise:</b>	2.5-4.0 (RMS)
<b>Gratings:</b>	Multiple grating choices, optimized for UV, VIS or NIR
<b>Slits:</b>	Optical fiber is entrance aperture
<b>Focal length:</b>	42 mm (input); 68 mm (output)
<b>Resolution:</b>	~ 0.3 nm-10.0 nm FWHM
<b>Stray light:</b>	< 0.05% at 600 nm; < 0.10% at 435 nm; <0.10% at 250 nm
<b>Fiber optic connector:</b>	SMA 905 to single-strand optical fiber (0.22 NA)

**Figure 5.31. Two channel multimode white light system.**

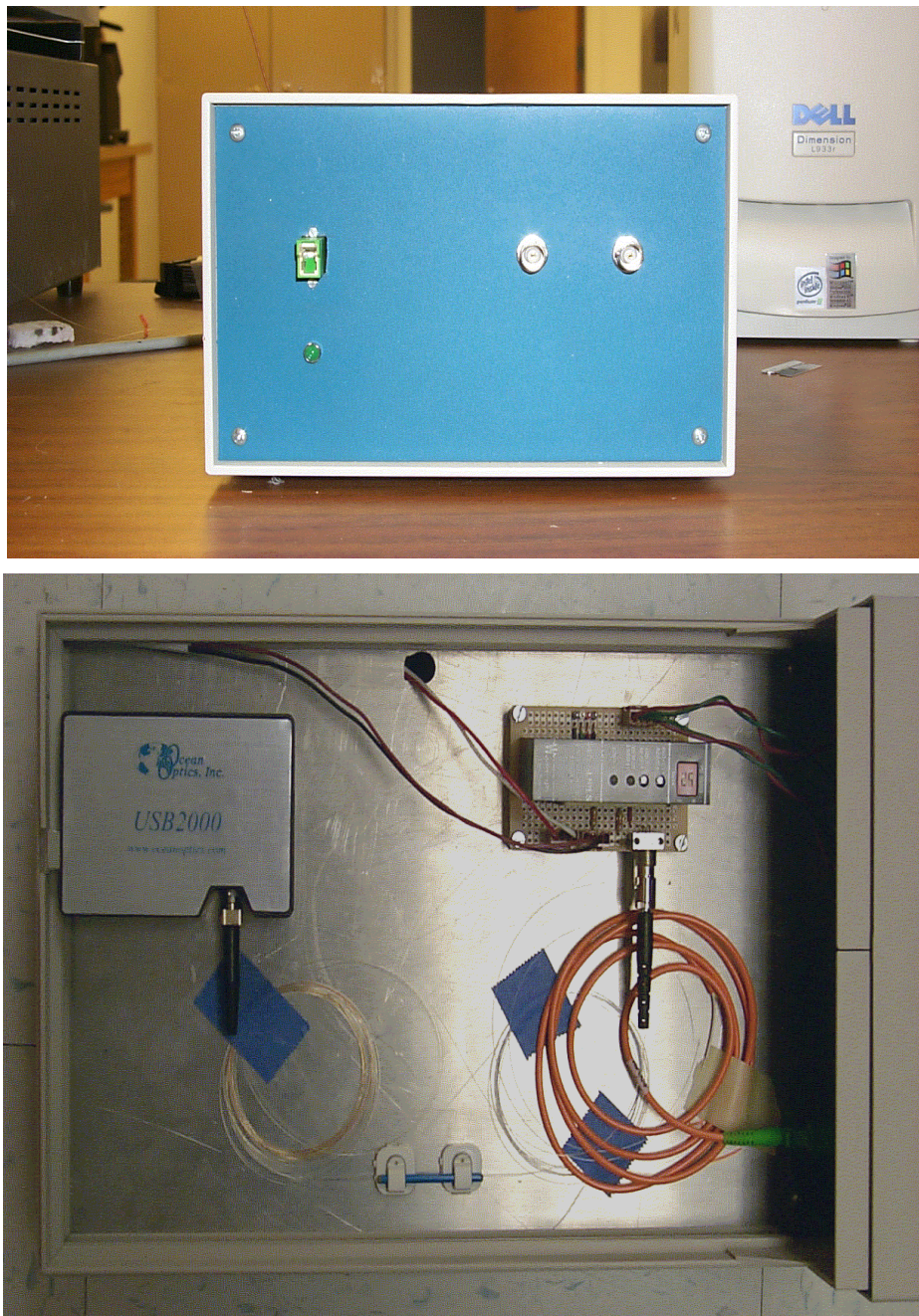


**Figure 5.32. Single channel multimode white light system.**

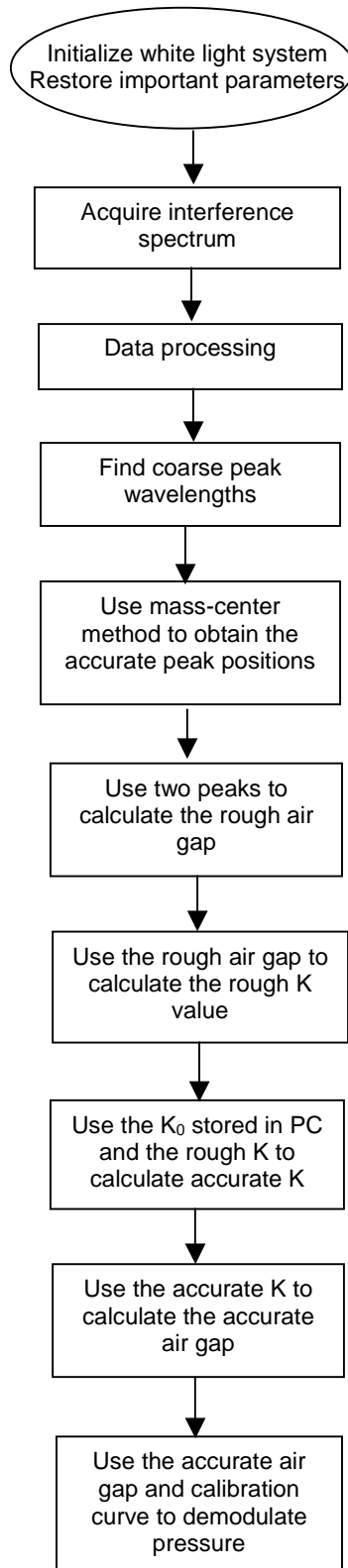


**Figure 5.33. Block diagram of demodulation program.**

#### 5.2.4.2 *Spectrum measurement*

The interference spectrum from the FABRY-PEROT sensor head will be sampled according to the given time interval. Once the received light signal emerges from the optical fiber, it is coupled into the spectrometer through a SMA connector. Once in the spectrometer, the divergent light is collimated by a spherical mirror. Then, a plane grating is employed to diffract the collimated light. A second spherical mirror focuses the resulting diffracted light and an image of the spectrum is projected onto a one-dimensional 2048-pixel linear CCD array. These reverse-biased photodiodes discharge a capacitor at a rate proportional to the photon flux. When the integration period of the detector is complete, a series of switches close and transfer the charge of each pixel to a shift register. After the transfer to the shift register is complete, the switches open, the capacitors attached to the photodiodes are recharged and a new integration period begins. At the same time as the light energy is being integrated, the spectrum data is read out of the shift register by a built-in A/D card. Finally, the spectral data is sent to the PC through an USB port.

#### 5.2.4.3 *Data processing*

To demodulate the pressure (or temperature) signal from the interference spectrum accurately, an advanced data processing algorithm was developed and realized in Visual Basic. This part is the core of the whole program, and will be discussed in several sub-steps:

##### Pre-processing

The original spectral data from the spectrometer is a 1x2048 array, which is composed of the received light signals of the 2048 pixels of CCD detector. To recover the interference spectrum, the calibration curve of the CCD is used to calculate the real wavelength from the serial number of array. To remove the dark current noise of the CCD detector and other background noise, a dark spectrum stored in the PC is deducted from the measured spectrum. The dark spectrum was acquired when the light source was powered off. Figure 5.34 shows the spectrum after this step.

##### Smoothing and Normalization

In Figure 5.34 noise is apparent in the received spectrum. To improve the signal-to-noise ratio (SNR), a boxcar algorithm was developed to filter and smooth the raw data. The spectrum after smoothing is shown in Figure 5.35, where the spectrum is automatically truncated according to its signal level. This ensures that only the high SNR region of the spectrum is included in the calculations. Then the measured spectrum will be normalized by the Gaussian profile reference spectrum of the light source (Figure 5.36).

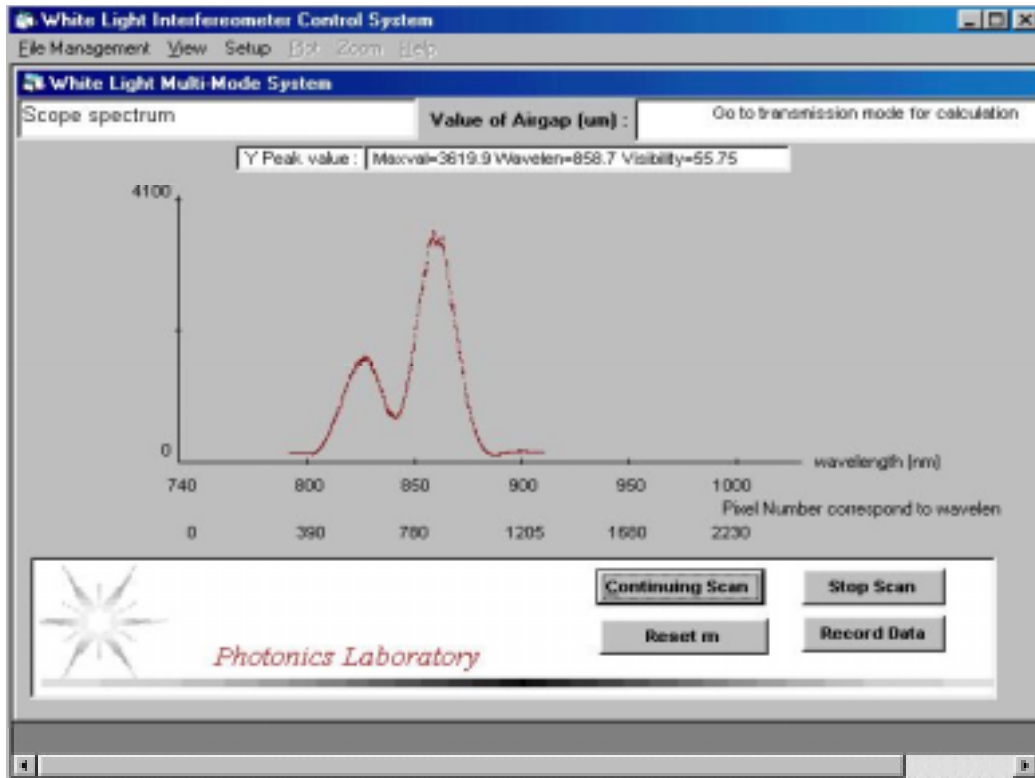


Figure 5.34. The interference spectrum after pre-processing.

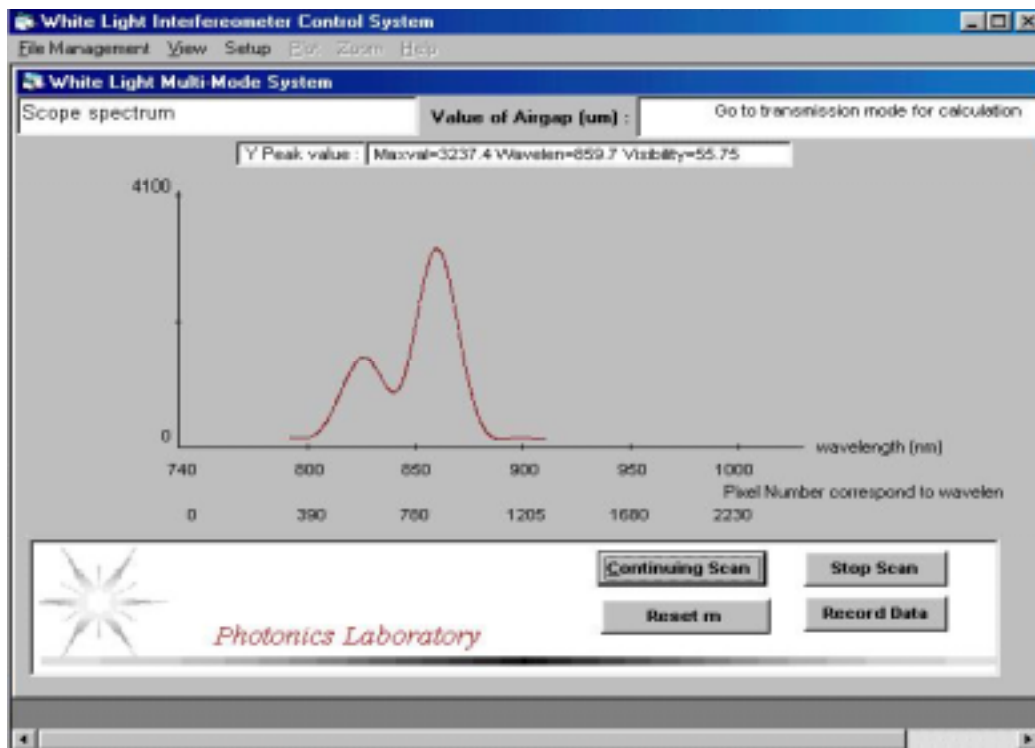


Figure 5.35. The interference spectrum after smoothing.

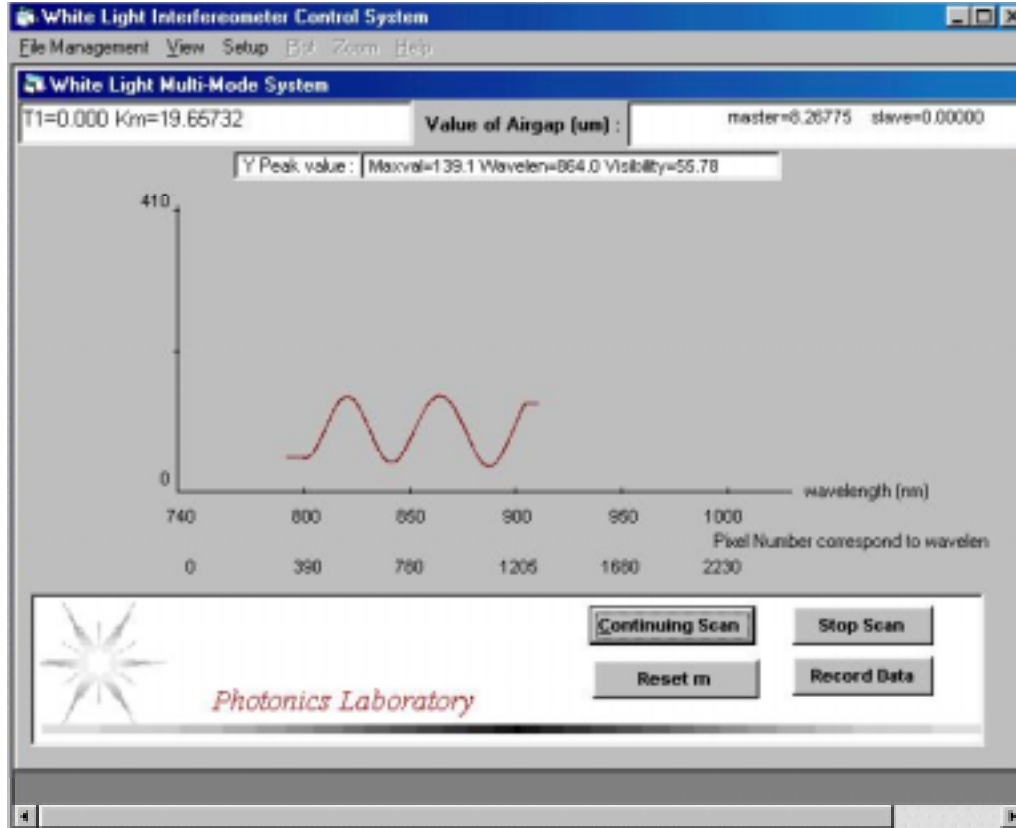
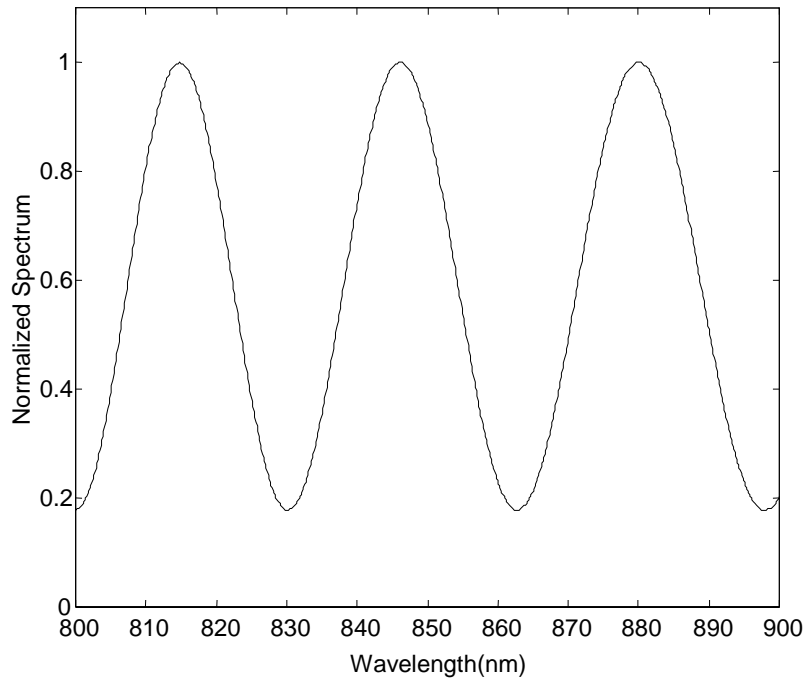


Figure 5.36. Normalized interference spectrum.

An important parameter of the boxcar smoother is the window width, which must be selected very carefully. An unsuitable window width may induce deformation of the interference spectrum. Suppose the measured spectrum is  $\{f(i), i=1, 2, \dots, 2048\}$ , then the boxcar smoothing process can be described as:

$$f_s(i) = \frac{1}{2w+1} \sum_{j=-w}^{j=w} f(i+j). \quad (5-60)$$

where  $w$  is the window width. Obviously, the larger the window width of the filter is, the better the performance that can be achieved. On the other hand, a large window width will cause two problems. First, the visibility of the spectrum will decrease when the window width is increased due to the averaging arithmetic. Second, because the interference spectrum is not a symmetric function of wavelength, the average process will induce the deformation of interference spectrum and shift of peak positions. Figure 5.37 shows the simulated results for a small window width ( $w=5$ ; air gap  $G=11\mu\text{m}$ ). In this case, no obvious deformation is observed, and a high visibility was achieved.



**Figure 5.37. Simulated result for small window width ( $w=5$ ).**

In comparison, Figure 5.38 shows the simulated result for a large window width ( $w=80$ ;  $G=11$ ). The visibility of interference spectrum decreases substantially and obvious deformation can be observed. Figure 5.39 shows the measured results when a large window width was used ( $w=61$ ), the result is very similar to the simulated results shown in Figure 5.38. To get the best performance and prevent the deformation of the interference spectrum, the window width needs to be optimized for each different CCD detector, light source and air gap of the FABRY-PEROT sensor. The basic principles are: 1) the more CCD pixels per unit wavelength space, the larger the window width that can be used; 2) the smaller the FABRY-PEROT sensor air gap (which means the space between adjacent peaks is large), the larger the window width can be.

#### Peak location

Demodulation of the air gap is based on the peak positions in the interference spectrum. The technique for peak location is described here.

The first step is to find the coarse locations of the peaks and valleys by a smart comparison algorithm. The basic idea is to find all the local maximum points within a specific range in the interference spectrum. The size of the searching range, which is defined as the window size of peak searching, must be large enough to eliminate the influence of noise. On the other hand, to avoid missing some peaks, the window size must be smaller than the space between adjacent peaks. An FFT algorithm is used to automatically estimate the optimum window size for peak searching. After the coarse position of the peaks has been found, a mass-centroid algorithm is applied to find the accurate peak positions. The basic theory of the

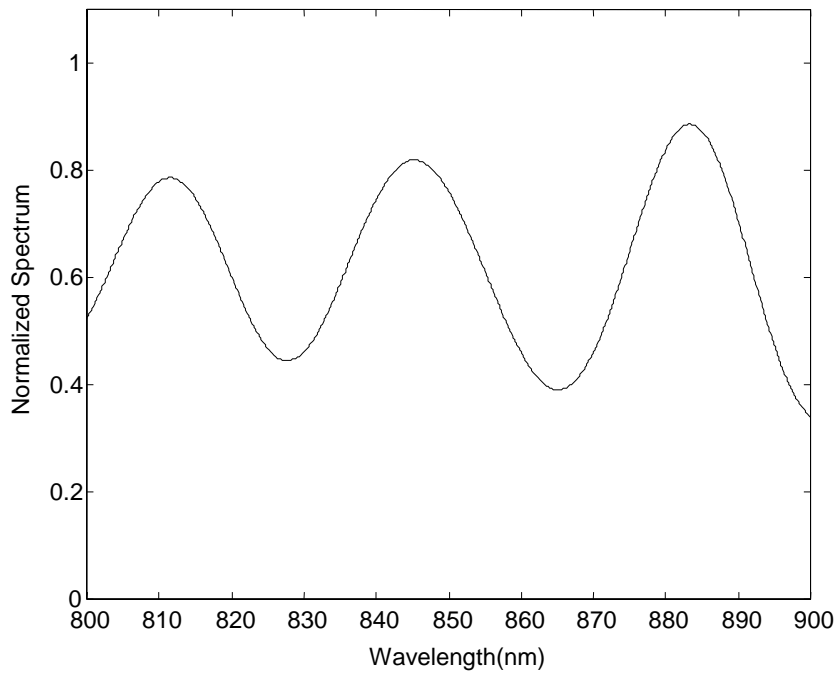


Figure 5.38. Simulated result for large window width ( $w=80$ ).

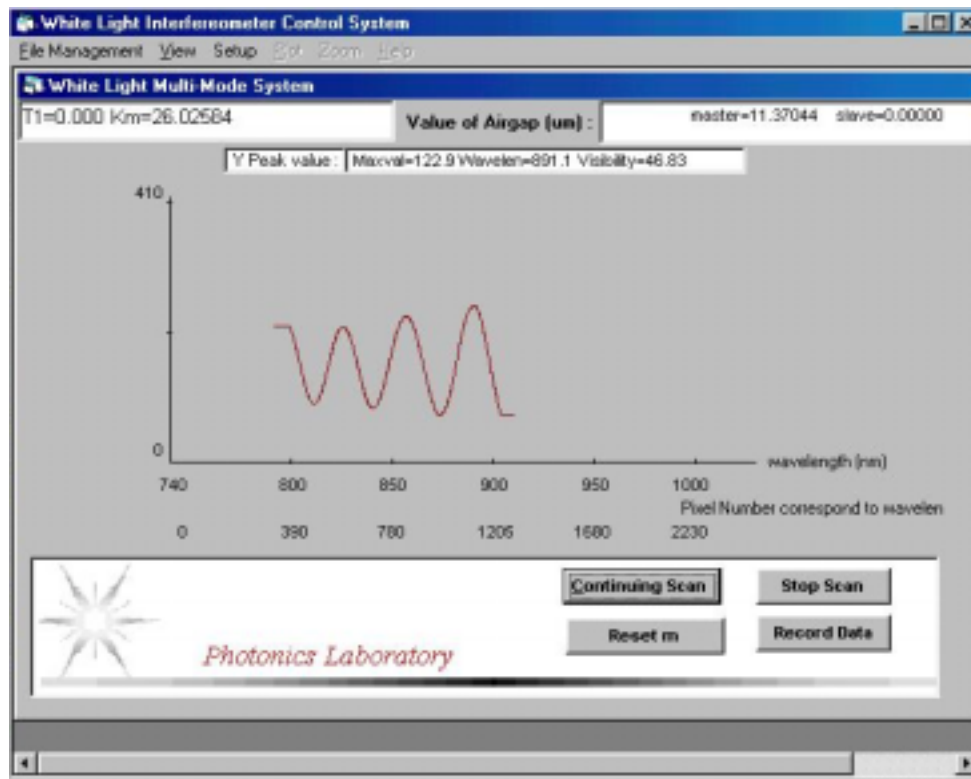


Figure 5.39. Measured result when a large window width was used.

mass-centroid algorithm is shown in Figure 3.11. If the function  $Y(x)$  is symmetry around its peak position, then the peak position coincides with the  $x$  coordinate of the centroid of  $Y(x)$ .

As shown in Figure 5.40, the peak position  $X_0$  can be calculated from

$$X_0 = \frac{\int xf(x)dx}{\int f(x)dx}. \quad (5-61)$$

From the equation  $I_n(\lambda) = 2(1 + \cos(\frac{4\pi G}{\lambda} + \varphi_0))$ , around the peak point, the spectrum is a symmetrical function of  $k=1/\lambda$ . Therefore, the spectrum  $y(\lambda)$  must be changed into  $k$ -space first (from  $\{y_i, \lambda_i\}$  to  $\{y_i, k_i\}$ ).

Starting from the normalized spectrum  $\{y_i, k_i\}$ , the accurate peak positions can be calculated from the coarse peak positions:

$$\begin{aligned} k_i &= \frac{1}{\lambda_i} \\ k_m^p &= \frac{\sum y_i k_i (k_i - k_{i-1})}{\sum y_i (k_i - k_{i-1})}. \\ \lambda_m^p &= \frac{1}{k_m^p} \end{aligned} \quad (5-62)$$

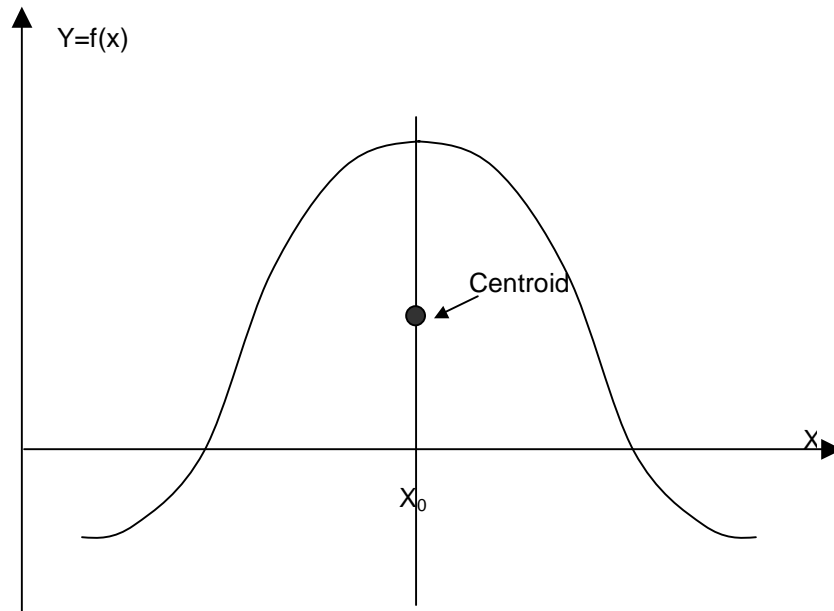


**Figure 5.40. The mass-centroid method.**

### Demodulation of the measured physical parameter

Once the peak positions were determined, the physical parameter to be measured can be demodulated. A coarse air gap will be calculated using two peak positions, and then the coarse  $k$  value for a specific peak will be determined. From the  $K_0$  value stored in the PC, the accurate  $k$  value will be determined, which in turn is used to calculate the accurate air gap. The current air gap will be compared with the previous air gap measurement value to judge if a "jump" happened during this process. If it does happen, the measurement results will be modified by a suitable value. Finally, using the calibration curve, the pressure (or temperature) will be demodulated from the accurate air gap.

#### **5.2.5 White light system performance**

The multimode white light system has been used as the signal demodulation system for pressure, temperature and flow sensors. Here, some common results are discussed. Other characteristics of the white light system, such as repeatability, long-term stability, etc, will be discussed with a specific sensor in the following chapters.

##### *5.2.5.1 Large dynamic range and linearity*

The major advantage of the white light system is the large dynamic range. Figure 5.41 shows the testing results from a Fabry-Perot temperature sensor. During this experiment, the signal demodulating system was kept in a stable environment; the FABRY-PEROT sensor head was put into an electrical oven. While the temperature of electrical oven increased from room

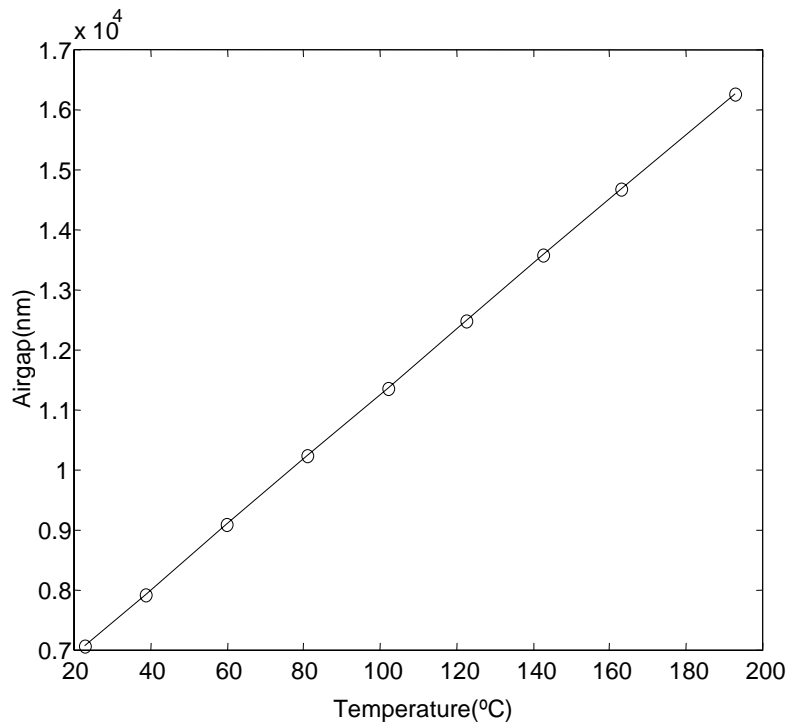


**Figure 5.41. Testing results from the FABRY-PEROT temperature sensor.**

temperature to about 200°C, the air gap of the FABRY-PEROT sensor head increased from 7 $\mu\text{m}$  to about 16 $\mu\text{m}$ , giving a dynamic range of about 9 $\mu\text{m}$ . Compared with the 200nm dynamic range of SCIIB sensors, the dynamic range was increased about 45 times. Figure 5.41 also shows very good linearity. In fact, as long as the coefficient of thermal expansion (CTE) of the material is a constant, the measurement results will have a linear relationship with the temperature.

#### 5.2.5.2 High resolution

One characteristic of the interferometric-based sensor is the high resolution. Figure 5.42 shows the testing results for a pressure sensor over 30 seconds. The sample rate is about 5 Hz. During this experiment, the whole system (white light and FABRY-PEROT sensor) was kept in a stable environment (both temperature and pressure). The resolution of the sensor system is usually interpreted by the standard deviation of a series of air gap measurements. It is common to use twice the standard deviation as the direct measure of resolution. In Figure 5.42, the standard deviation is about 0.015nm, which gives a resolution of about 0.03nm. This is the resolution limit of the white light system. In field application, due to various noise sources (such as temperature fluctuation, mechanical vibration, etc), it's very difficult to reach this limit.

#### 5.2.5.3 Temperature characteristics

The temperature dependence of the white light system comes from two sources: the LED and the spectrometer. Their contributions will be discussed separately as follows.

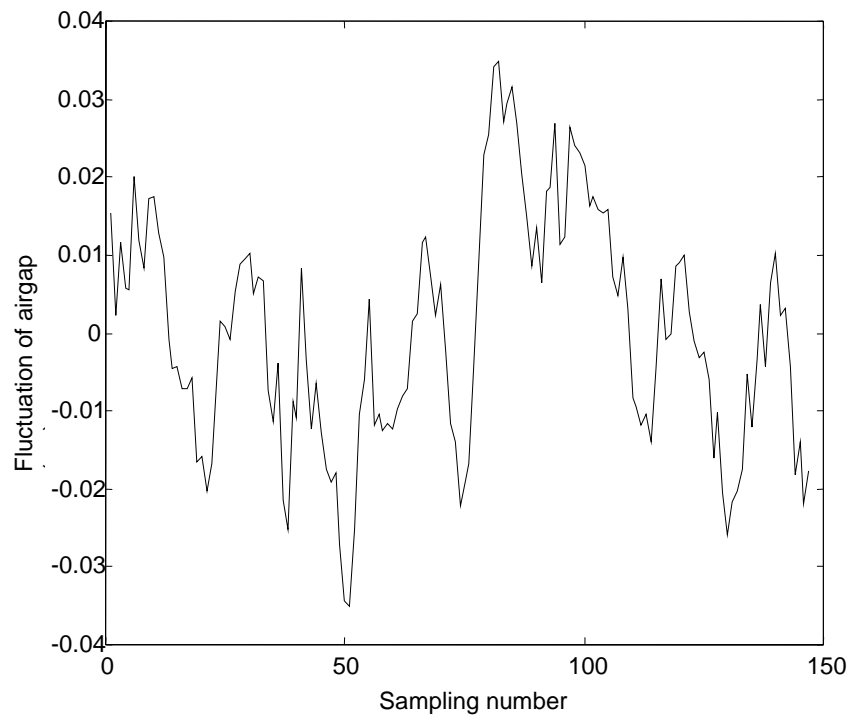


**Figure 5.42. Short term fluctuation of the white light system.**

LED

Although the spectrum of the LED had been measured and stored in the PC as the reference spectrum, when the ambient conditions change, the spectrum of LED may drift. The center wavelength of the LED will shift to a longer wavelength determined by the material characteristics as the temperature increases. Suppose the reference spectrum was acquired at temperature  $T_0$ , and the central wavelength at that temperature is  $\lambda_0$  then, the reference spectrum can be described as

$$R(\lambda) = I_0 \exp\left(-\frac{(\lambda - \lambda_0)^2}{w^2}\right), \quad (5-63)$$

where  $w$  is the spectral width of the light source. When the temperature increases to  $T$ , the center wavelength of the LED will shift to  $\lambda_T$ . Since no method can be used to acquire the spectrum of LED in real time, the reference spectrum acquired at temperature  $T_0$  will be used to normalize the interference spectrum acquired at temperature  $T$ . The normalized spectrum  $N(\lambda)$  calculated in this way can be expressed as

$$N(\lambda) = \frac{\exp\left(-\frac{(\lambda - \lambda_T)^2}{w^2}\right)}{\exp\left(-\frac{(\lambda - \lambda_0)^2}{w^2}\right)} \left(1 + \gamma \cos\left(\frac{4\pi G}{\lambda}\right)\right). \quad (5-64)$$

The simulated curve  $N(\lambda)$  is shown in Figure 5.43. Here the air gap  $G$  is supposed to be  $9.2\mu\text{m}$ , the spectral width  $w$  is  $27\text{nm}$ , the visibility of the interference spectrum  $\gamma$  is  $0.5$ , and the shift of central wavelength is  $5\text{nm}$ . Figure 5.44 shows the measured result of a Fabry-Perot sensor when the temperature was increased to about  $45^\circ\text{C}$  (the reference spectrum was acquired at  $25^\circ\text{C}$ ). The theoretical analysis and the experimental result match very well. Obviously, since the reference spectrum acquired at a different temperature, the peak positions in interference spectrum shifted.

Suppose the LED center wavelength shift is

$$\delta = \lambda_T - \lambda_0 = a\Delta T \ll \lambda_0. \quad (5-65)$$

Then

$$\frac{\exp\left(-\frac{(\lambda - \lambda_T)^2}{w^2}\right)}{\exp\left(-\frac{(\lambda - \lambda_0)^2}{w^2}\right)} \approx \left(1 + \frac{2(\lambda - \lambda_0)}{w^2} \delta\right). \quad (5-66)$$

So Eq. (5-64) becomes

$$N(\lambda) = \left(1 + \frac{2(\lambda - \lambda_0)}{w^2} \delta\right) \cdot \left(1 + \gamma \cos\left(\frac{4\pi G}{\lambda}\right)\right). \quad (5-67)$$

The peak position shift  $\Delta\lambda$  can be acquired by differentiating the last equation.

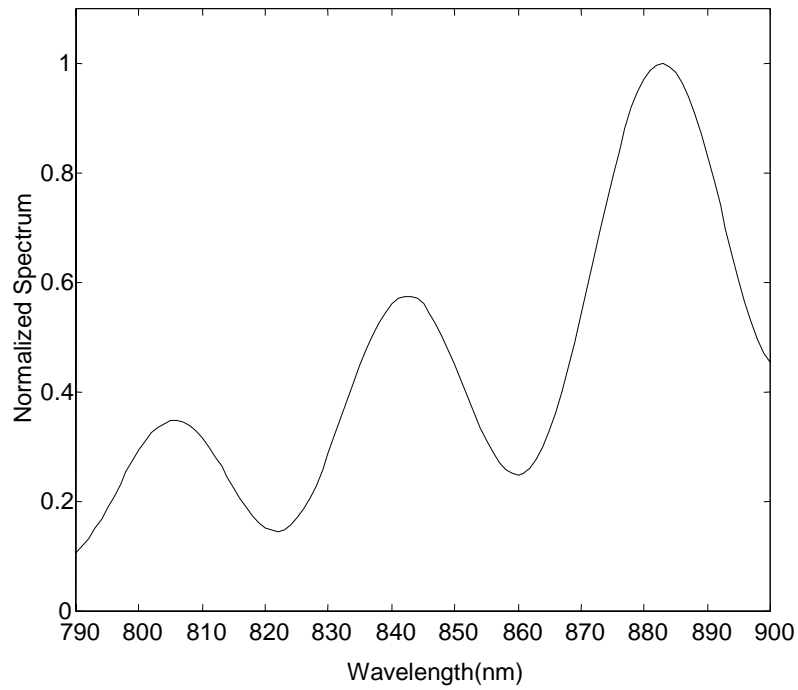


**Figure 5.43 Simulated normalized spectrum.**

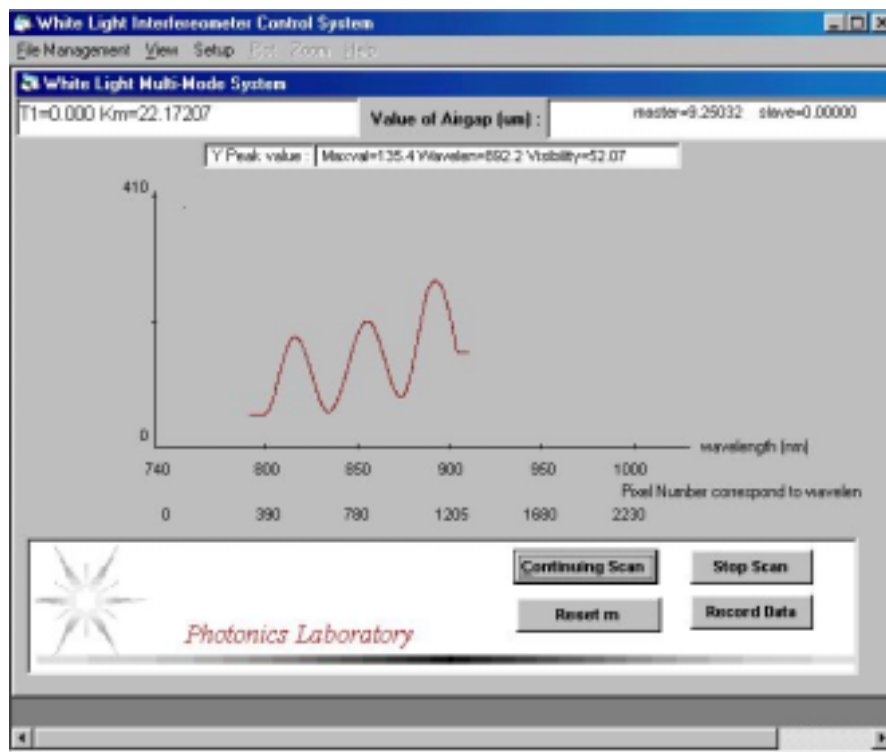


**Figure 5.44. Measurement results of the normalized spectrum at 45°C.**

)

$$\frac{\partial N}{\partial \lambda} = \frac{2\delta}{w^2} + \frac{4\pi G \gamma}{\lambda^2} \sin \frac{4\pi G}{\lambda} + \frac{2\delta}{w^2} \gamma \cos \frac{4\pi G}{\lambda} + \frac{2(\lambda - \lambda_0)\delta\gamma}{w^2} \cdot \frac{4\pi G}{\lambda^2} \cdot \sin \frac{4\pi G}{\lambda} = 0 \quad (5-68)$$

$$\Delta\lambda = \frac{(1 + \gamma)\lambda^4}{8\pi^2 \gamma G^2 w^2} \cdot \delta$$

Using  $G = m\lambda/2$ , the error in air gap  $\Delta G$  induced by peak position shift  $\Delta\lambda$  is

$$\Delta G_L = \frac{(1 + \gamma)\lambda^3}{8\pi^2 \gamma G w^2} \cdot \delta_L = \frac{(1 + \gamma)a\lambda^3}{8\pi^2 \gamma G w^2} \cdot \Delta T. \quad (5-69)$$

In general, the temperature coefficient of an LED ( $a$  in Eq. (5-69)) can be treated as a constant; when the air gap  $G$  is a fixed number, the air gap error induced by the light source temperature change is linearly dependent on the temperature change.

The temperature dependence of the light source was measured experimentally. During this experiment, the light source was kept in an electric oven; the spectrometer and other parts were kept in the room environment. The temperature of the oven was increased to about 50°C, and kept at that temperature for about 2 hours. Then the temperature was decreased to room temperature slowly (in about 3 hours). During the temperature decreasing process, a thermocouple was used to sample the temperature in the oven, and the spectrum of the LED was sampled by the Ocean Optics card. Figure 5.45 shows the test results. The temperature coefficient of the LED is about 0.27nm/°C. For a regular FABRY-PEROT sensor ( $G = 10000\text{nm}$ ,  $\gamma = 0.6$ ) the temperature characteristics induced by the shift of LED central wavelength is about 0.77nm/°C.

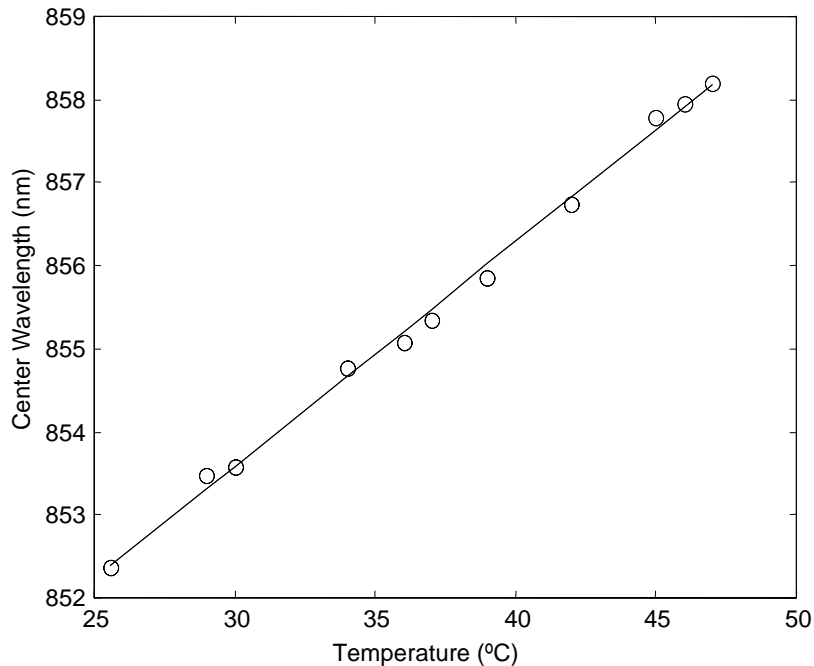


**Figure 5.45. Relationship between center wavelength of the LED and temperature.**

### Spectrometer

Although the spectrometer was set up on a temperature-regulated bench, the residual temperature dependence is still critical for high-resolution measurement. Suppose the wavelength drift of spectrometer is  $\delta_s$ . Obviously, the peak positions in the interference spectrum will also shift this amount. On the other hand, similar to the LED, the wavelength shift will induce the deformation of normalized spectrum. So the total air gap error induced by the spectrometer is

$$\Delta G_s = \left( \frac{G}{\lambda} + \frac{(1+\gamma)\lambda^3}{8\pi^2\gamma G w^2} \right) \cdot \delta_s = b \cdot \left( \frac{G}{\lambda} + \frac{(1+\gamma)\lambda^3}{8\pi^2\gamma G w^2} \right) \cdot \Delta T. \quad (5-70)$$

The gross temperature dependence of the white light system can be expressed as

$$\begin{aligned} \Delta G &= \Delta G_L + \Delta G_s \\ &= \frac{(1+\gamma)\lambda^3}{8\pi^2\gamma G w^2} \delta_L + \left( \frac{G}{\lambda} + \frac{(1+\gamma)\lambda^3}{8\pi^2\gamma G w^2} \right) \cdot \delta_s \\ &= \left[ a \cdot \frac{(1+\gamma)\lambda^3}{8\pi^2\gamma G w^2} + b \cdot \left( \frac{G}{\lambda} + \frac{(1+\gamma)\lambda^3}{8\pi^2\gamma G w^2} \right) \right] \cdot \Delta T \end{aligned} \quad (5-71)$$

From the last equation, the temperature coefficient of the white light system is a function of the air gap  $G$ . That means for FABRY-PEROT sensors with a different air gap, or for the same sensor under different pressure (or temperature), the temperature coefficient of the white light system will be different. To realize temperature compensation, the air gap dependent temperature coefficient  $K(G)$  must be determined experimentally. As long as  $K(G)$  is determined, the compensation steps are as follows.

1. The rough air gap  $G'$  (without temperature compensation) is acquired.
2. Use  $G'$  to determine  $K(G)$ :  $K(G) \approx K(G')$ .
3. Use  $K(G)$  and the temperature acquired by a thermocouple to calculate the accurate air gap  $G$ :  $G = G' + K(G') \Delta T$

## **5.3 Comparison Between the SCIIB System and the White Light System**

Both the SCIIB system and the white light system have their advantages and disadvantages. Compared to the white light system, the major advantage of the SCIIB system is the high speed. In the case where very high frequency response is not an important issue, such as pressure, temperature and flow measurement, the white light system has superiority over the SCIIB system. The main advantages of the white light system over the SCIIB system are discussed in this section.

### **5.3.1 Dynamic range**

The most important advantage of the white light system is the large dynamic range. Different from the SCIIB system, the operating range of the white light system is not limited to a half wavelength. In fact, the dynamic range of the white light system is only limited by the

coherence length and the structure of the sensor head. By choosing a large gauge length or suitable material, the sensitivity of the sensor head can be increased dramatically.

In the multimode white light system, the lower limit of the air gap is decided by the spectral width of the light source. From the data processing method discussed above, at least two peak points are needed to demodulate the air gap from the interference spectrum. For the 850nm LED used in the multimode white light system, the effective spectral range (the range in which a high signal noise ration can be realized) is about 80nm, so the minimum air gap of the FABRY-PEROT sensor is about

$$G_{\min} = \frac{\lambda_1 \lambda_2}{2\Delta\lambda} \approx 4.5 \mu m . \quad (5-72)$$

In actual application, the lower limit of the air gap was set to 5 $\mu$ m.

The upper limit of the air gap is decided by the coherence length of the white light system. To achieve high-resolution measurement, high visibility of the interference spectrum is needed. Because the spectrometer has a high wavelength resolution (<1nm), the coherence length determined by this factor is pretty large:

$$L_c \approx \frac{\lambda^2}{\Delta\lambda} \approx 700 \mu m . \quad (5-73)$$

So, in the working range (usually smaller than 20 $\mu$ m), this factor can be neglected. A more important factor is the large numerical aperture (NA) of the multimode fiber. There are numerous modes propagating in a multimode fiber, and different fiber modes take different light paths. Obviously, the shortest path in a Fabry-Perot sensor is  $P_{\min}=2G$  and the longest one is about  $P_{\max}=2G/\cos\theta$  ( $\theta=\sin^{-1}(NA)$ ). Roughly, when the path difference is larger than  $\lambda/2$ , the visibility was considered as too low to achieve high-resolution measurement. The NA of multimode fiber used in this system is about 0.15, so the upper limit of the air gap is

$$\begin{aligned} \frac{2G_{\max}}{\cos\theta} - 2G_{\max} &= \frac{\lambda}{2} \\ G_{\max} &= \frac{\lambda \cos\theta}{4(1-\cos\theta)} \approx 19.2 \mu m \end{aligned} \quad (5-74)$$

By choosing a suitable initial air gap and suitable materials for the sensor head, the dynamic range of the FABRY-PEROT sensor can be limited to 5—18  $\mu$ m. Comparing with the 200nm dynamic range of the SCIIB system, it has increased more than 50 times. That's the main advantage of the white light system over the SCIIB system.

### 5.3.2 Insensitivity to the change of the polarization status

As discussed in Section 5.1, some optical components in the SCIIB system are polarization dependent. Even though a fiber optic depolarizer is connected in this system, the error induced by the change of the polarization status is still as high as 0.5% when the fiber is bent and flipped. In the white light system, the grating of the spectrometer is also a strong polarizer; it polarizes light along the vertical axis of the spectrometer. Yet, all the CCD pixels

receive the diffractive light from the same grating, so the polarization dependence of all pixels will be same. When the polarization status changes, the outputs from 2048 pixels will change by the same scale, so the shape of the interference spectrum will not change. The white light system is therefore insensitive to the change of polarization status.

### ***5.3.3 Demands on the Geometrical Parameters of the FABRY-PEROT Sensor***

The white light system demodulates the air gap from the interference spectrum directly. Many physical parameters, such as pressure, temperature, etc, have a linear relationship with the air gap change, which means the white system will have a linear output in the whole dynamic range. The sensitivity is decided by the materials for the sensor head and the gauge length of the FABRY-PEROT sensor. It's not necessary to set the initial gap at a very accurate value. Yet, in the SCIIB system, to fully use the limited linear range, the initial air-gap must be set at an accurate value. This makes the sensor fabrication for the SCIIB system much more difficult than that for the white light system.

Both the SCIIB system and the white light system have their special advantages. In general, for high-resolution applications, the white light system is the best candidate; when the measurement speed becomes an important issue, the SCIIB system is a good choice. In this project, for pressure, temperature and flow measurement, the white light system was employed.

## 6.0 Automated Sensor Fabrication System

Prior to this program, the method used in fabricating extrinsic Fabry-Perot interferometer (FABRY-PEROT) sensors was limited to epoxy bonding of two fibers (with their endfaces cleaved) inserted into a capillary tube with the proper inner diameter. Although extensive research has been conducted to find high performance epoxies to fabricate FABRY-PEROT sensor probes, the fabricated sensors generally failed to provide satisfactory performance in terms of mechanical strength and thermal stability due to the viscoelastic nature of all epoxies and due to the low decomposition temperatures. Another constraint of the epoxy-based sensors is that the maximum operating temperature is limited to temperature below about 300°C due to decomposition and for sensors which undergo a mechanical load, even room temperature is too high to avoid the viscoelastic creep. Because epoxies have a relatively high coefficient of thermal expansion (CTE) which is significantly different from that of the fibers and the tube, epoxy bonded sensors are usually very sensitive to temperature changes, which makes it difficult to use those sensors to measure parameters other than temperature. Upon heating, large thermal stresses are generated in the bonding region due to the CTE mismatch. Control of the sensor initial cavity length (a critical factor in the sensor manufacturing) and the bonding area are very difficult with epoxy bonding because of the relatively long curing time of the epoxy. Furthermore, due to the viscoelastic nature of the polymer, epoxy bonding will also degrade the frequency response of the FABRY-PEROT sensor in case of high frequency signals need to be measured.

Telecommunication optical fibers are usually made by doping very small amounts of germania into pure silica glass. Fused silica capillary tubes of various sizes are commercially available. In contrast to the well-defined melting points of crystalline materials, silica glass is an amorphous material. As the fused silica glass is heated, the viscosity continuously drops to the point at which the article is no longer able to support its own weight. For the fused silica capillary tubes used in sensor fabrication, at a temperature of about 1500°C, it becomes soft enough that it begins to deform around the optical fiber when heated rapidly with a CO<sub>2</sub> laser. This softening of the fused silica capillary tube allows the use of thermal fusion techniques to bond the fiber and the capillary tube together. By locally heating the fiber and tube assembly to a temperature above which the glass is softened sufficiently, the tube and the fiber can flow into each other and locally join to form a solid bond.

A major research task of the program was to develop an automated sensor fabrication system. The sensor fabrication system uses a high-energy carbon dioxide (CO<sub>2</sub>) laser to provide the heating power and a white light spectrum interferometer measurement system to monitor the cavity length of the sensor in real-time during fabrication. This system allows the automatic fabrication of a large quantity of high performance sensors at a low cost.

## 6.1 System Configuration

As shown in Figure 6.1, the automated SCIIB sensor fabrication system includes three sub-systems: the carbon dioxide (CO<sub>2</sub>) laser heating sub-system, the white light fiber optic interferometric air gap monitoring sub-system, and the micropositioning sub-system. A high-energy CO<sub>2</sub> laser is used as the heating source. It generates high-energy optical pulses at a wavelength of 10.6 μm. When the silica glass material is exposed to the CO<sub>2</sub> laser output, it absorbs the optical energy and converts it to thermal energy, which allows the silica glass materials to be heated locally up to very high temperatures. The white light fiber optic interferometric system is used to allow accurate on-line monitoring of the SCIIB sensor air gap. Several ultra-precise micropositioning stages are also used in the system to allow precise movement of the two fibers in three dimensions. A computer is used to control and coordinate these three sub-systems so that the CO<sub>2</sub> laser output power, the motion of the stages and the sensor air gaps can be automatically and precisely controlled during the sensor fabrication process. Figure 6.2 shows the picture of the automated SCIIB sensor fabrication system.

## 6.2 CO<sub>2</sub> Laser Sub-System

The CO<sub>2</sub> laser used in the system is a SYNRAD, Inc Model 48-2. The wavelength emitted by the laser is 10.6 μm, and the maximum output optical power under continuous mode operation is 25 W. The original beam diameter of the laser output is 3.5 mm. After using a germanium lens with a focal length of 2.5 inches, a spot size of about 100 μm in diameter can

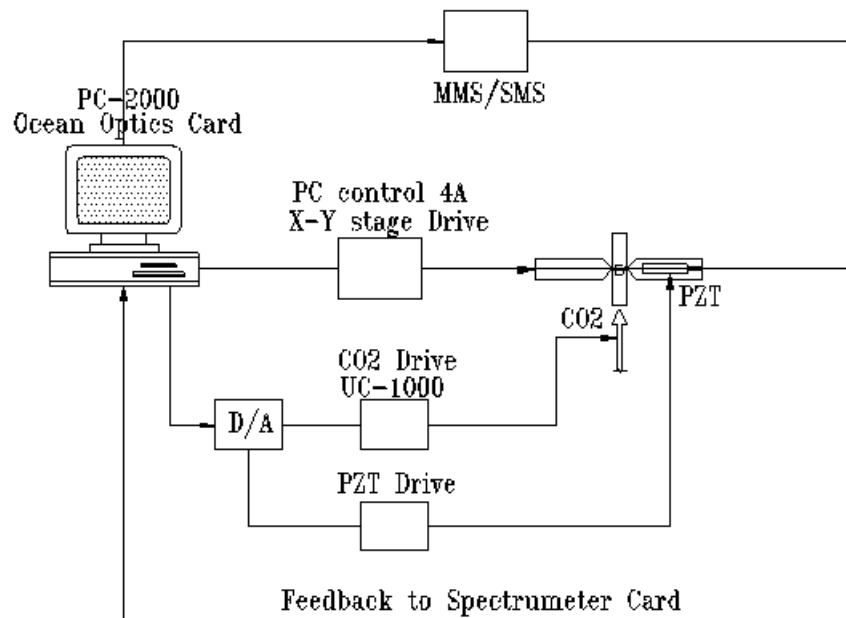


Figure 6.1. Schematic of the automated sensor fabrication system.



**Figure 6.2. Automated SCIIB sensor fabrication system.**

be achieved at the focal point, which results in a divergence angle of about 4 milliradians. The laser can also be used to generate short optical pulses that are externally modulated through a controller, producing a minimum pulse duration of about 200  $\mu$ s.

### 6.3 CO<sub>2</sub> Laser Sub-System

The CO<sub>2</sub> laser used in the system is a SYNRAD, Inc Model 48-2. The wavelength emitted by the laser is 10.6  $\mu$ m, and the maximum output optical power under continuous mode operation is 25 W. The original beam diameter of the laser output is 3.5 mm. After using a germanium lens with a focal length of 2.5 inches, a spot size of about 100  $\mu$ m in diameter can be achieved at the focal point, which results in a divergence angle of about 4 milliradians. The laser can also be used to generate short optical pulses that are externally modulated through a controller, producing a minimum pulse duration of about 200  $\mu$ s.

The control of the CO<sub>2</sub> laser output involves two parts: the power level control and the lasing duration control. The power level control can be accessed by externally applying a 0-10 V voltage signal (corresponding to 0-25 W output power) and the pulse duration can be controlled by inputting a standard TTL gating signal to enable or disable the laser output. Because it is necessary to precisely control the heating time and the temperature during the sensor fabrication, we designed and implemented a special circuit to allow computer programmable control of the CO<sub>2</sub> laser. The block diagram of the CO<sub>2</sub> laser control subsystem is given in Figure 6.3. By properly programming the DIO-24 interface card (National Instruments), the power control signal is sent out to the D/A circuit, which converts the digital signal to an analog output from 0 to 10 volts at a resolution of 16 bits. The laser enabling or disabling signal is also converted to a TTL gating signal through the same circuit.

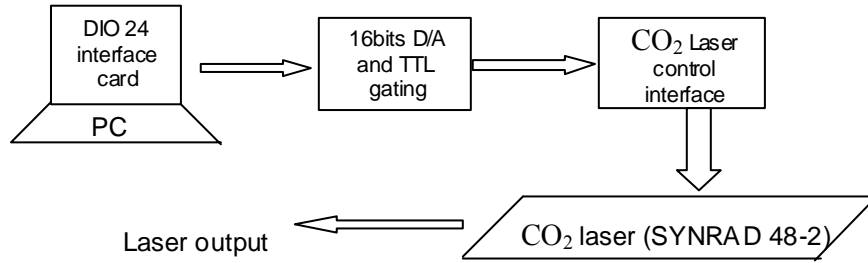


**Figure 6.3. Block diagram of the CO<sub>2</sub> laser control subsystem.**

### 6.3.1 Mechanical strength improvements

To improve the mechanical strength of the sensor probe, a mirror subassembly was designed and incorporated into the system. In the initial design, the output beam from the CO<sub>2</sub> laser heated the capillary tube and fiber assembly from one direction, which resulted in nonuniform temperature increases in the fused silica capillary tube. Many sensors fabricated were found either not completely sealed or with too many residual stresses after fabrication. Improvement in the mechanical strength of the sensor probe was achieved by adding a set of copper mirrors to the fabrication stage, as shown schematically in Figure 6.4. Two mirrors (made by polishing precisely fabricated copper plates) were placed underneath the sensor assembly. The angle between the two copper mirrors was set to be 120°. The CO<sub>2</sub> laser beam was also aligned to input to the assembly at an angle of 60°. Therefore, the input beam and the two reflected beams from the mirrors heat the sensor assembly at the three evenly distributed directions. Experiments were also conducted to find the optimal CO<sub>2</sub> laser power and the duration. With the mirror set described above, the sensor assembly can be bonded uniformly to minimize the residual stresses.

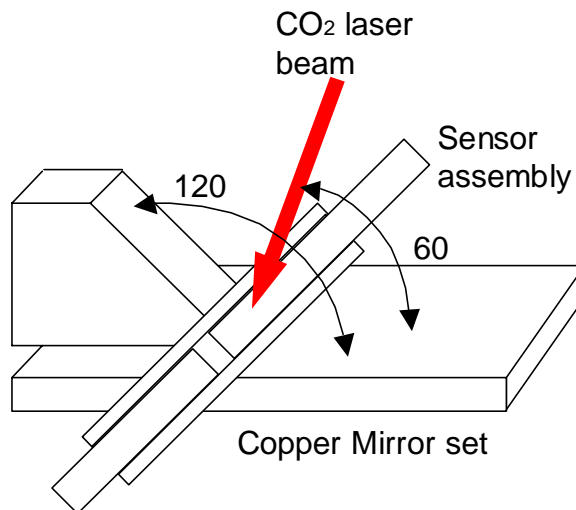


**Figure 6.4. Schematic of the copper mirror set in sensor fabrication system.**

## 6.4 White Light Fiber Optic Interferometer Sub-System

This sub-system is the main part of the automatic sensor fabrication system. It allows on-line monitoring of the length of the SCIIB sensor air gap with a very high accuracy. The measurement of air gap length is achieved by demodulating the interference spectrum of the sensor output as described in the section below. The spectrum is obtained through a computer-interfaced spectrometer. In order to retain the design flexibility to be able to fabricate both multimode and singlemode SCIIB sensors, two white light interferometric air gap monitoring systems were constructed. The two systems share the same spectrometer but use different sources and fibers.

### 6.4.1 Principle of white light interferometric air gap monitoring

The basic principle of the white light interferometric air gap monitoring can be illustrated using Figure 6.5. When the sensor is fabricated, two fibers with cleaved endfaces are inserted into a capillary tube. The partially reflected optical waves at these two endfaces will generate an interference signal that is transmitted back to the spectrometer through a 2x2 fiber coupler.

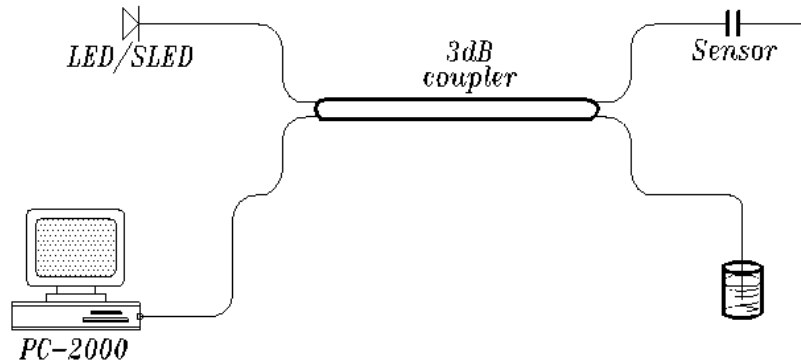


**Figure 6.5. Basic principle of the white light interferometric air gap monitoring system.**

If we assume that the white light source (LED or SLED) has a Gaussian spectral power distribution given by

$$I_s(\lambda) = I_0 \exp\left[\frac{-(\lambda - \lambda_0)^2}{(\Delta\lambda)^2}\right], \quad (6-1)$$

where  $\lambda_0$  is the central wavelength,  $I_0$  is the peak value, and  $\Delta\lambda$  is the source spectral width. The output interference signal is then given by

$$I_s(\lambda) = I_0 \exp\left[\frac{-(\lambda - \lambda_0)^2}{(\Delta\lambda)^2}\right], \quad (6-2)$$

where the factor  $\gamma$  takes into account the decreased visibility due to the numerical aperture of the fiber as well as other attenuating effects, and where  $\varphi_0$  is the arbitrary initial phase difference between the two interference signals. If we normalize the interference spectrum given by Eq. (6-2) with respect to the source spectrum, we have the normalized interference output expressed as

$$I_n = 2 \left[ 1 + \gamma(L) \cos \left( \frac{4\pi L}{\lambda} + \varphi_0 \right) \right], \quad (6-3)$$

It is shown in Eq. (6-3) that the spectrum output by the sensor is modulated by a sinusoidal function due to the interference. Because the interference spectrum is a function of the sensor air gap length  $L$ , the successful demodulation of this spectral signal can render an accurate and absolute measurement of the sensor air gap length.

A simple case can be considered in which two different spectral components of the source ( $\lambda_1$  and  $\lambda_2$ ) are utilized. These two wavelength components arrive at the spectrometer with different phases, which can be expressed as

$$\varphi_{1,2} = \frac{4\pi L}{\lambda_{1,2}} + \varphi_0. \quad (6-4)$$

Thus the phase difference between these two spectral components is given by

$$\Delta\varphi = \varphi_1 - \varphi_2 = \frac{4\pi L(\lambda_2 - \lambda_1)}{\lambda_1 \cdot \lambda_2}. \quad (6-5)$$

Rewriting Eq. (6-5), we have

$$L = \frac{\Delta\varphi \cdot \lambda_1 \cdot \lambda_2}{4\pi(\lambda_2 - \lambda_1)}. \quad (6-6)$$

If the phase difference of these two spectral components are known, the absolute value of the sensor air gap length  $L$  can be calculated by Eq. (6-6). Although it is not easy to measure the phase difference of two spectral components, there exist a few special points with a fixed phase relationship. For example, the phase difference between two adjacent peaks (or valleys) is  $2\pi$ . Therefore, by detecting the spectral locations of the peaks or valleys in the interference spectrum, we can obtain the cavity length  $L$  by applying Eq. (6-6).

#### **6.4.2 Implementation of multimode and singlemode white light subsystems**

The spectrometer used in the white light subsystem is a fiber optic PC plug-in spectrometer (PC2000 manufactured by Ocean Optics, Inc.). The PC-2000 spectrometer card uses a 600-line holographic grating to diffract the input light to a CCD array, and interfaces with the computer using a 12 bit A/D through the ISA bus. The blaze wavelength is 850 nm, and the best efficiency is from 750 nm to 950 nm, which covers the whole light source spectrum of interest. The resolution of this spectrometer is approximately 0.3 nm, and the highest data acquisition speed is 1000 kHz.

#### 6.4.2.1 Multimode white light air gap monitoring system

The configuration of the multimode white light air gap monitoring system is shown in Figure 6.6. It uses an LED with center wavelength of 850 nm and spectral width of 74 nm as the source. The fiber used is a standard multimode graded index 62.5/125 $\mu$ m telecom fiber. A picture of the system is shown in Figure 6.7.

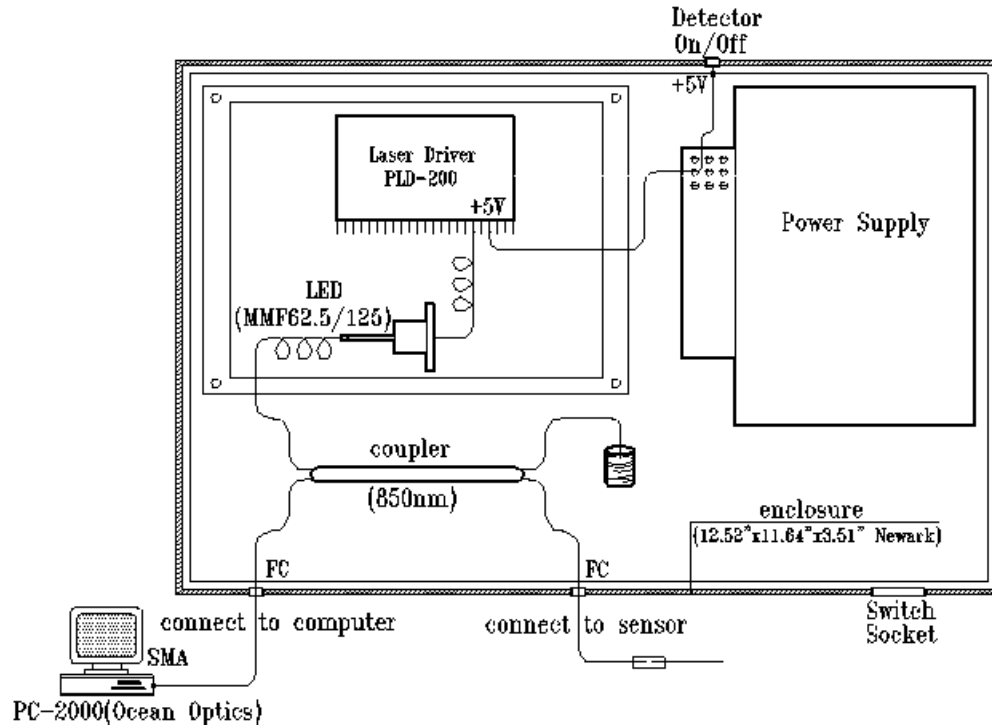


Figure 6.6. Configuration of the multimode white light air gap monitoring system.



Figure 6.7. Picture of the multimode white light air gap monitoring system.

#### 6.4.2.2 Singlemode white light air gap monitoring system

The configuration of the singlemode white light air gap monitoring system is shown in Figure 6.8. It uses a SLED with center wavelength of 1310 nm and a spectral width of 40 nm as the source. The fiber used inside the system is a standard 9/125  $\mu\text{m}$  singlemode telecom fiber. A picture of the system is shown in Figure 6.9.

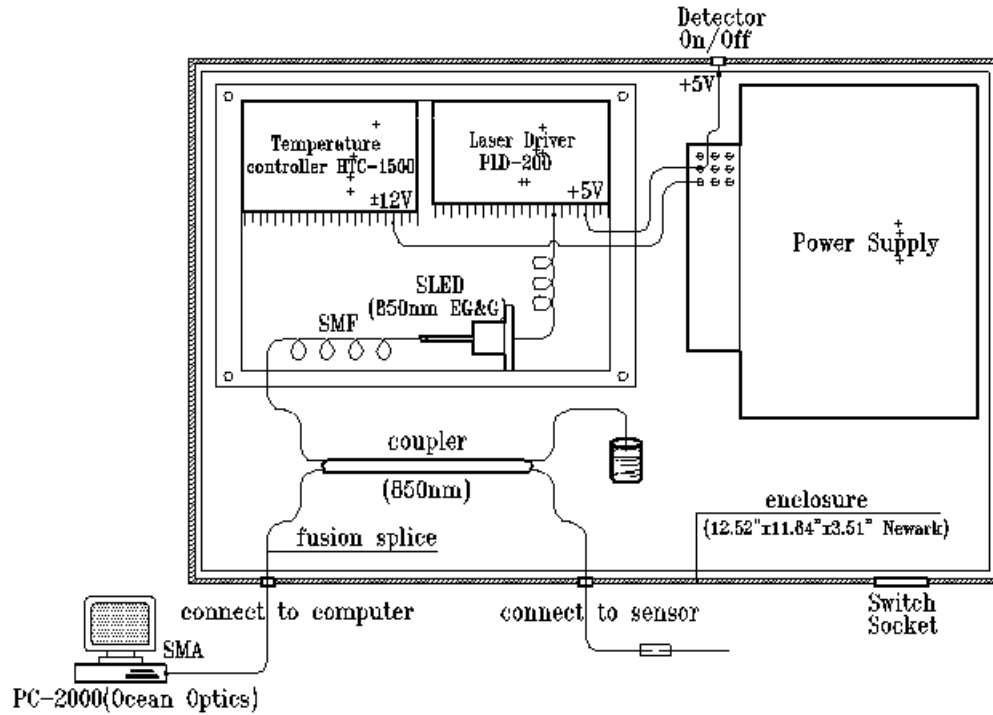


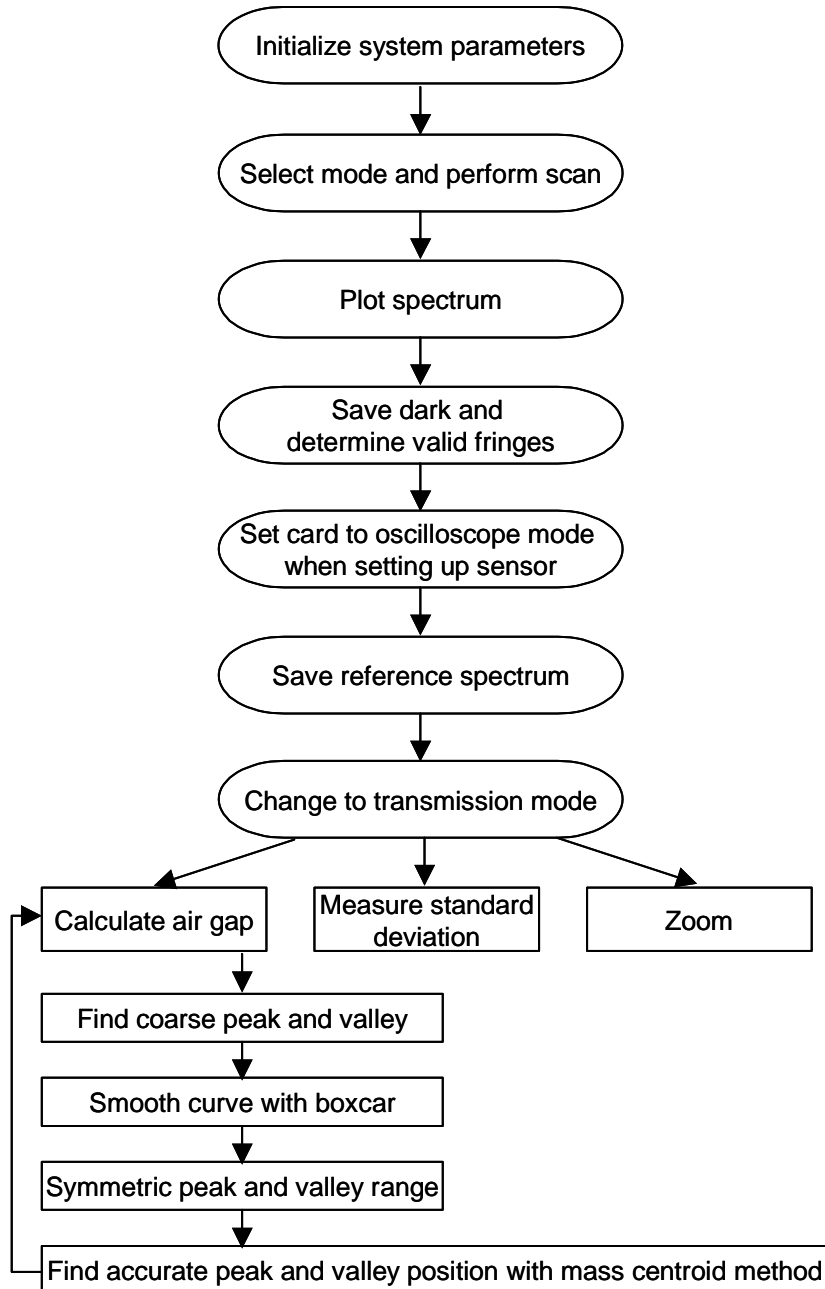
Figure 6.8. Configuration of the singlemode white light air gap monitoring system.



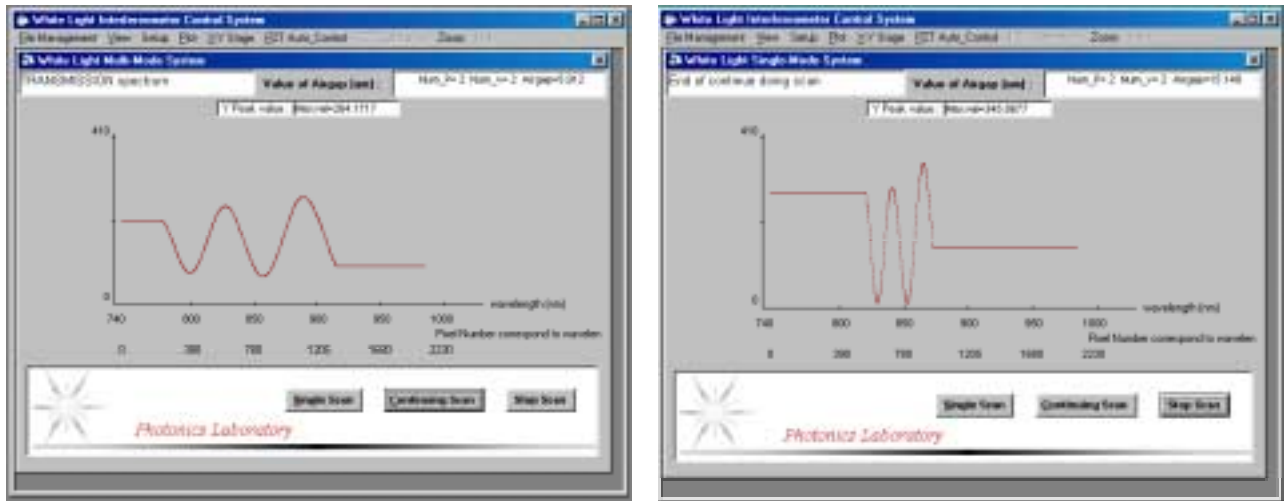
Figure 6.9. Picture of the singlemode white light air gap monitoring system.

### 6.4.3 Software design of white light sub-system

The software discussed in Section 5.2 was initially developed to monitor the air gap length during sensor fabrication. A block diagram of the monitoring software is shown in Figure 6.10. The graphical interfaces of the designed software are shown in Figure 6.11. The major functions of this software are described in this section.



**Figure 6.10. Block diagram of air gap monitoring software.**



(a) Multimode

(b) Singlemode

**Figure 6.11. White light air gap monitoring software under operation.**

#### 6.4.3.1 Initialization

The program begins with the system parameter initialization, including initialization of the spectrometer, initialization of the system configuration, and initialization of the system constants necessary for the air gap calculation. The program automatically saves all the parameters of the last experiment. However, each individual parameter can also be changed manually during the operation.

#### 6.4.3.2 Pre-processing

The main purpose of this part is to improve the signal-to-noise ratio (SNR) of the system and improve the air gap length measuring accuracy.

- 1) The dark spectrum is saved to allow only pure spectral data to be processed after the subtraction algorithm.
- 2) The original spectrum of the light source is saved as the reference so that the interference spectrum can be normalized to eliminate the distortions induced by the source spectrum.
- 3) A boxcar algorithm is developed to filter and smooth the raw data so that the noise of the spectrometer is minimized.
- 4) The interference spectrum is automatically truncated according to its signal level. This ensures that only the high SNR region of the spectrum is included in calculations of the air gap length.

#### 6.4.3.3 Demodulation

This part includes the most important functions of the software.

- 1) The saved dark spectrum is subtracted from the input spectrum, and the saved reference spectrum is used to normalize the interference spectrum so that the source spectrum effects are eliminated.

- 2) Coarse locations of the peaks and valleys are found by a smart comparison algorithm. These coarse locations are used as reference marks in the demodulation.
- 3) An FFT algorithm is used to automatically estimate the window size of the interference spectrum. This allows an optimal number of data points to be used in the signal demodulation.
- 4) A mass-centroid algorithm is applied to find the interference peaks (or valleys) and the corresponding wavelengths.
- 5) The final air gap length is calculated according to Eq. (6-6).

### 6.5 Micropositioning Subsystem

During the sensor fabrication, the fibers and capillary tube must be kept precisely aligned, the sensor air gap must be accurately adjusted to the preset value, and the bonding distance, which determines the sensor effective gauge length, also needs to be precisely controlled. Therefore it was necessary to design a fiber positioning system for the sensor fabrication to accurately position the fibers and tubes. The computer controlled micromotion fiber and tube positioning system is illustrated in Figure 6.12. The two fibers are positioned on two V-grooves using magnets, and the V-grooves are fixed to a 3-dimensional translation stage, respectively. Between the two translation stages, a supporting block with another V-groove on top is used to position the capillary tube. All the V-grooves are specially designed and manufactured to hold the fibers or the capillary tube tightly. After installation, the three V-grooves are precisely aligned to fall in a straight line so that there is no offset angle during

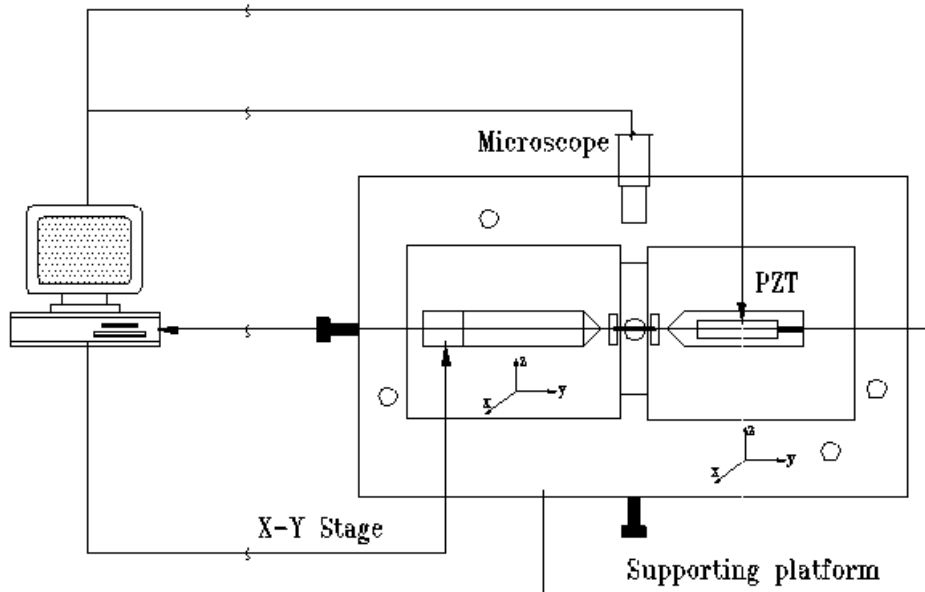


**Figure 6.12. Computer controlled micro-motion fiber and tube positioning system.**

sensor fabrication. Fibers can be inserted into the central capillary tube by moving the two translation stages in three dimensions. To allow precise adjustment of the sensor air gap length, another small PZT-actuated stage is used to move the target fiber with ultra-high resolution along z-direction. The movement of the stage is controlled by the central computer through a PZT driver and a 16 bit D/A circuit. In order to control the sensor gauge length, a big translation stage is used to move the whole setup in two directions with respect to the CO<sub>2</sub> laser beam. After the tube is bonded to the lead-in fiber, this stage can precisely position the second bonding point with respect to the CO<sub>2</sub> laser beam. A video microscope system is used to help the aligning procedure and to monitor the whole sensor fabrication process. A picture of the sensor fabrication stage system is shown in Figure 6.13.

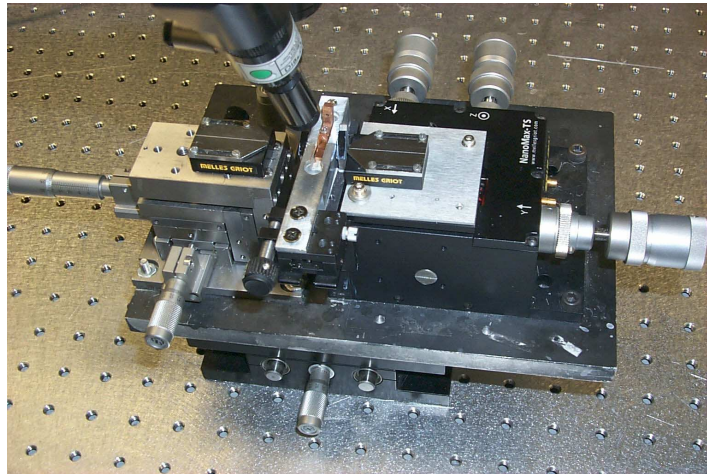


**Figure 6.13. Micropositioning stage system.**

## 6.6 System Testing Results

A number of tests and experiments were conducted using the implemented automatic sensor fabrication system. The main purpose of these tests is two-fold: 1) to verify the design and to check out the functions of each subsystem, 2) to fabricate SCIIB sensors for further evaluation.

### 6.6.1 White light subsystem performance test and results

The purpose of designing the white light subsystem is to realize on-line monitoring of the sensor air gap length during sensor fabrication. There are a few key performance characteristics that required testing before it could be used. These include the accuracy, dynamic range, and frequency response of the air gap measurement.

#### 6.6.1.1 Standard deviation

The standard deviation of the white light subsystem air gap measurement was determined by using a fiber optic extrinsic Fabry-Perot interferometric (FABRY-PEROT) sensor with a fixed air gap. Using the white light system, we measured the FABRY-PEROT sensor air gap 100 times. Based on the measurement results, we can calculate the standard deviation of the white light system. Actually, this function is built in the software so that we can perform the

standard deviation measurement at anytime. The standard deviation of the multimode system was calculated to be  $\sigma=0.003\mu\text{m}$ . The standard deviation for the singlemode system was found to be  $\sigma=0.02\mu\text{m}$ .

#### 6.6.1.2 Frequency response

Using the software, the sensor air gap length can be calculated in less than 0.1 second. The corresponding frequency response of the system is higher than 10 Hz. The average fabrication time of the SCIIB sensor is about 20 seconds, therefore the frequency response of the white light system is high enough for our applications.

#### 6.6.1.3 Dynamic range

The multimode system can measure sensor air gap lengths from 4  $\mu\text{m}$  to 20  $\mu\text{m}$ , and the singlemode system can measure from 8  $\mu\text{m}$  to 70  $\mu\text{m}$ . The standard deviation of the sensor air gap measurement is constant over the whole dynamic range. The typical initial air gap is about 6  $\mu\text{m}$  for multimode and 15  $\mu\text{m}$  for singlemode; therefore, the dynamic ranges of the white light system for both systems are large enough.

### 6.6.2 CO<sub>2</sub> laser power calibration

The CO<sub>2</sub> laser is used as the heating source during the sensor fabrication. It is important to control the laser output power and exposure duration to ensure solid bonding between fibers and tube. Laser power that is too large and exposure time that is too long can result in degradation of the optical properties of the optical fiber and the too much built-in stress at the bonding region. On the other hand, laser power that is too weak or exposure time that is too short can result in incomplete bonding.

The CO<sub>2</sub> laser output is quite nonlinear when it is controlled through the external analog port. To achieve precise control of the output power, we conducted a calibration experiment for the CO<sub>2</sub> laser. The laser output power was measured using a power meter. The results are plotted in Figure 6.14. Based on the calibration data, the CO<sub>2</sub> laser power can be accurately mapped to the external control voltages. Thereafter, precise control of the laser output power can be realized through curve-fitting method.

### 6.6.3 PZT Stage calibration

The final fine adjustment of the sensor air gap is achieved by moving the PZT stage. The movement of the PZT stage is controlled by the computer programs through a 16 bit D/A circuit and a PZT driver. However, the relationship between the PZT displacement and the external control voltage is not linear. In order to adjust the air gap to a preset value at a ultra-high accuracy, the PZT stage movement was calibrated with respect to the input control voltages. The calibration was conducted by using the white light interferometer and an extrinsic Fabry-Perot interferometric (FABRY-PEROT) sensor. First we implemented a Fabry-Perot micro-displacement sensor with one fiber sealed to the tube, and the other fiber fixed to the PZT stage. When the PZT stage moves, it generates an interferometric displacement signal through the FABRY-PEROT sensor. At the same time, this interferometric signal was measured by the white light interferometric air gap monitoring system. Relating the PZT control voltage to the white light interferometer output, the PZT stage can be precisely calibrated. Figure 6.15 shows the PZT calibration results. By using curve-fitting method, we can control the PZT stage movement with a very high accuracy by referring to the stored calibration data.

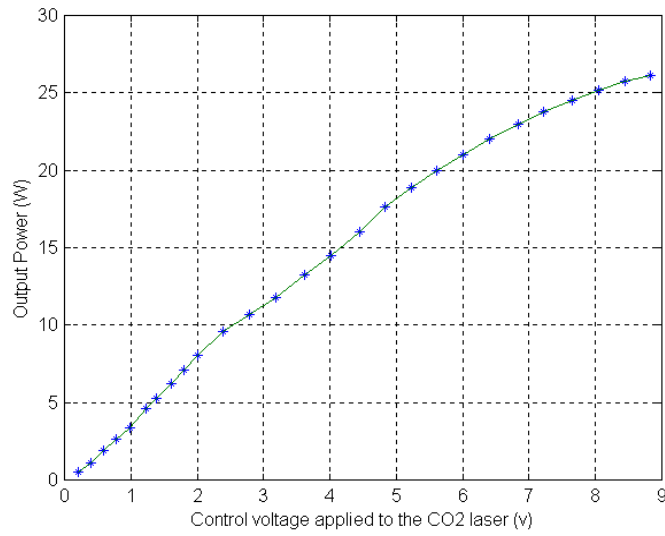


**Figure 6.14. CO<sub>2</sub> laser output power calibration results.**

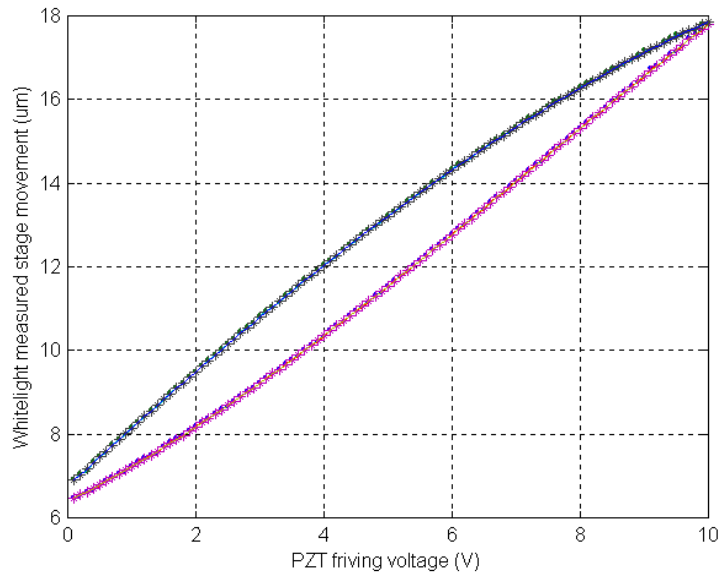


**Figure 6.15. PZT stage movement calibration results.**

## 6.7 Fabrication Procedure Optimization

### 6.7.1 CO<sub>2</sub> laser power and exposure time optimization

Thermal bonding is the most important step in SCIIB sensor fabrication. When the tube and fiber assembly are exposed to CO<sub>2</sub> laser light, the optical energy is converted to thermal energy which results in an increase in temperature at the exposure area. If the temperature reaches the softening point of the glass material (about 1500°C), the tube and the fiber start to flow and join together. After the cooling, a solid bond is formed at the CO<sub>2</sub> laser exposure area. In order to achieve the best optical and mechanical performance of the fabricated sensor, the CO<sub>2</sub> laser exposure time and the power level must be set to their optimal values. There are a few points that must be considered in choosing the exposure time and the power level. First, to avoid excess residual stress from building in the bonding area, the increase and the decrease of the temperature should not be too fast. This results in an optimal design of the temperature increasing and the decreasing slope. Second, the glass materials should not be overheated; otherwise the gravity will bend the fiber, which results in a large optical power loss at the bonding region. Therefore, the laser power needs to be set to an optimal level. Third, there is an optimal time duration in which the glass materials are soft and fluid. A review of fiber optic fusion splicer design reported in the technical literature suggests that the duration at which the glass is softened should be limited to a few seconds. Based these considerations, we designed our CO<sub>2</sub> laser power and exposure time curve as shown in Figure 6.16. This design allows 2 seconds of preheating time, 3 seconds of heating time and 10 seconds of annealing time. The total fabrication time is about 15 seconds.

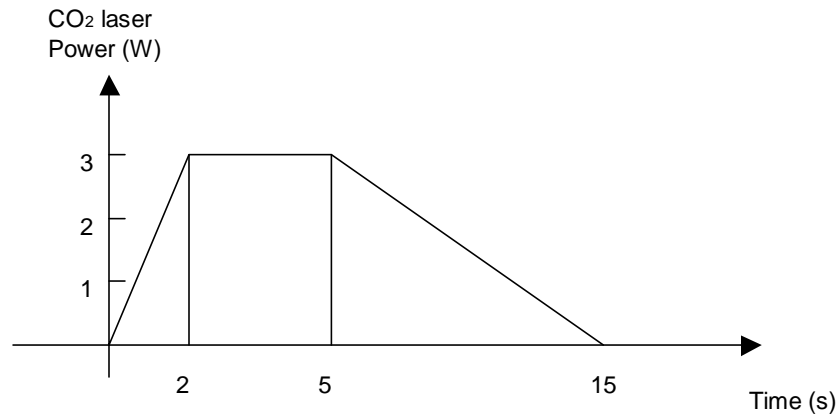


**Figure 6.16.** CO<sub>2</sub> laser power level and exposure time.

### 6.7.2 SCIIB sensor fabrication and results

After numerous experiments, we finalized all the parameters involved in SCIIB sensor fabrication. The final setup allows the tube and fiber assembly to be positioned 7.5 cm away from the CO<sub>2</sub> laser focal point. For multimode SCIIB sensors, the full laser power is 2.9 W, and for singlemode sensors the full laser power is 3.1 W. The sensor bonding region has a

typical size of 300  $\mu\text{m}$ . The sensor gauge length can be chosen from 0.8 mm to 5 mm. The initial gap can be adjusted to any value with an accuracy of 0.02  $\mu\text{m}$ . The bonding points have been tested to show good strength, and the sensor fabrication has a very good repeatability.

### 6.7.3 Repeatability improvements

To improve the repeatability of sensor fabrication, several measures were taken, including improvement of the measurement accuracy of the whitelight interferometric cavity length monitoring system, addition of a PZT stage system to tune the initial cavity length precisely, and a computer program to control the adjustment of the initial cavity length after sensor is bonded.

Initial tests demonstrated an accuracy of 0.02 $\mu\text{m}$  for singlemode whitelight system and 0.002  $\mu\text{m}$  for the multimode whitelight system. This is however not high enough to meet the sensor fabrication requirements. The mass centroid algorithm described in Section 5.2 was implemented to realize a large improvement in peak locating. Also, the peak or valley tracking algorithms were added to the system which dramatically improved the wavelength resolution of the system. The current accuracy of the whitelight system has been tested to be 0.001 $\mu\text{m}$  for singlemode fiber sensors and 0.0005  $\mu\text{m}$  for multimode fiber sensors. This is more than one order of magnitude improvement.

In addition to the improvement of the accuracy of the whitelight system, a high resolution PZT stage was also incorporated to the sensor fabrication system. With the completion of the driving circuits, and the computer control algorithms, the PZT stage allowed us to tune the sensor cavity length after the capillary tube and fiber was bonded together. By reheating the assembly with 80% of the CO<sub>2</sub> laser power required for bonding, and by controlling the PZT stage to pull the fiber with a resolution of 2nm, SCIIB sensors can now be fabricated repeatedly with the initial cavity lengths adjusted exactly to the starting point of the linear region.

## 6.8 Performance of Fabricated Sensors

Hundreds of SCIIB sensor probes have been made using the developed fabrication system. Fibers used to fabricate the sensor probe are carefully cleaned and cleaved using a York fiber cleaver. The capillary tube is also cleaned and cleaved to the desired length. With the help of the microscope, two fiber ends prepared by the cleaver are then inserted into the capillary tube and held on the positioning stages. By adjusting the micropositioning stage system, the two fibers are moved to the preset positions where the desired initial sensor cavity length is obtained. By moving the two-dimensional translation stage underneath the micropositioning stage system, the fiber and capillary tube assembly is brought to the center of the laser spot. The CO<sub>2</sub> laser emits light to heat the assembly with its power level and duration controlled by the computer program. After one side of the sensor is fused, the fiber and capillary assembly is then move to the other side to perform the same fusion process.

Figure 6.17 shows a photograph of a typical sensor probe imaged by the microscope. In the picture, we can clearly see the sensor cavity formed by the fiber endfaces and the two fusion points. So far, the shortest sensor gauge length that can be fabricated with the system is 0.5mm for the single-mode fiber-based sensor and 0.7mm for the multimode fiber-based sensor, respectively. It is very difficult to further reduce the sensor gauge length because the fiber endfaces can be damaged resulting from the too close fusion point.

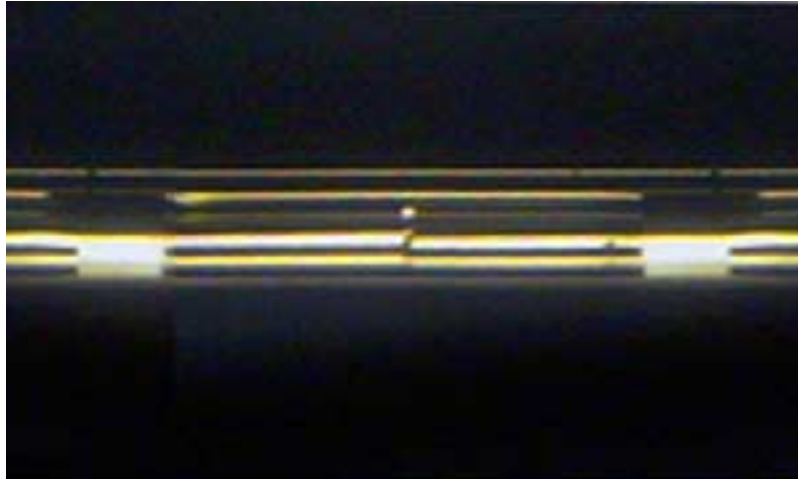


**Figure 6.17. Micrograph of the SCIIB sensor probe (Gauge length: 1.5mm, initial cavity length: 25.74 $\mu$ m).**

The sensor probes were expected to have high mechanical strength and sustain high pressures. This section describes experiments conducted to evaluate the sensor's survivability and temperature dependence.

### **6.8.1 Survivability of the sensor probe**

Before the sensors can be used in harsh environments, they must be tested to ensure a complete sealing at the two fusion points because an imperfect sealing would result in the intrusion of the outside medium and degradation of the sensor performance. More than one hundred sensors were first tested in a high pressure (>3000 psi) and high temperature (>200°C) water environment. Only two sensors were found to leak water into the cavities during the test. The majority of the sensors successfully survived the test. This made us believe that the controlled thermal bonding method could provide sensor probes strong enough to survive in harsh environments.

### **6.8.2 SCIIB sensor annealing**

The capillary tube and glass fibers are fused together in a very short time period during the sensor fabrication process. It is a reasonable concern that residual stresses might build up in the bonding regions due to the very large temperature difference. These residual stresses, when released slowly, will cause a sensor to drift from its original calibrated operating point. Therefore, the sensor must be properly annealed to release the built-in stresses prior to sensor calibration.

Sensor annealing was performed using an electrical furnace at a temperature of 600°C for 24 hours. During the annealing process, the temperature was increased and decreased slowly to avoid further stress build up. In order to see how the annealing affects the sensor performance, five sensors were annealed twice under the same experimental conditions, and the cavity lengths of the five sensors were monitored using the whitelight interferometer during the entire annealing process. The recorded changes in cavity length are listed in Table 6.1.

**Table 6.1. Sensor cavity length change before and after annealing.**

Sensor index	Gauge Length (mm)	Cavity length before annealing ( $\mu\text{m}$ )	Cavity change first annealing (nm)	Cavity change second annealing (nm)
1	0.7	20.0872	-37.2	2.7
2	1.0	39.6614	-15.8	3.3
3	1.0	29.1794	-68.4	*
4	1.0	20.4749	-32.2	1.9
5	0.7	21.3901	-13.1	3.4

\*The sensor was broken after the first annealing because of mishandling.

As shown in the table, the changes in sensor cavity lengths after the second annealing became very small compared to the first one, which indicate that the annealing process did improve the stability of the sensor. Although the sensors used in the experiment were chosen with different parameters (gauge lengths and initial cavity lengths) in hope to demonstrate the regularity of the annealing effect on the sensors, the results shown in Table 6.1 did not indicate an obvious relationship between the sensor parameters and changes in cavity lengths except that all the sensors showed a decrease in their cavity lengths after the annealing process. Nevertheless, the experiment indicated that the annealing process did cause a large change in sensor cavity length with respect to the linear range of operation (about 200nm). Therefore, the sensor annealing was proven to be necessary to assure the performance of the sensor.

### 6.8.3 Temperature dependence of the SCIIB sensor probe

The theoretical analysis discussed above showed that the temperature sensitivity depends on the sensor gauge length, the initial cavity length, and the CTEs of the fiber and the capillary tube. It is possible to design the sensor according to the temperature model to have very small or even zero temperature sensitivity. The actual CTEs of the fiber and the tube can deviate from the nominal values due to the small difference in the chemical composition among the materials used by different manufacturers. It is very difficult to determine the actual temperature dependence of the sensor probe just by referencing the nominal CTEs due to the extremely high accuracy required. The actual temperature dependence of the sensor probe therefore has to be measured experimentally.

### 6.8.3.1 Multimode SCIIB sensor probe

The experimental set-up included an electric furnace with a maximum temperature of 1100°C and an Omega CN76000 thermometer to read the temperature with an accuracy of 0.1°C. The multimode sensor probe and the thermocouple were put side by side in the furnace, and the temperature was increased from room temperature (30°C) to 810°C in steps of 10°C. Both the SCIIB sensor output and the thermometer output were recorded for comparison. The capillary tube used to fabricate the multimode sensor was made of fused silica purchased from Polymicro Technologies, Inc. The inner diameter of the tube is 130 μm, and the outer diameter is 365 μm. The sensor had an effective gauge length of 0.7 mm, and the initial cavity length of 5.160 μm. The sensor output versus the increase of the temperature is plotted in Figure 6.18.

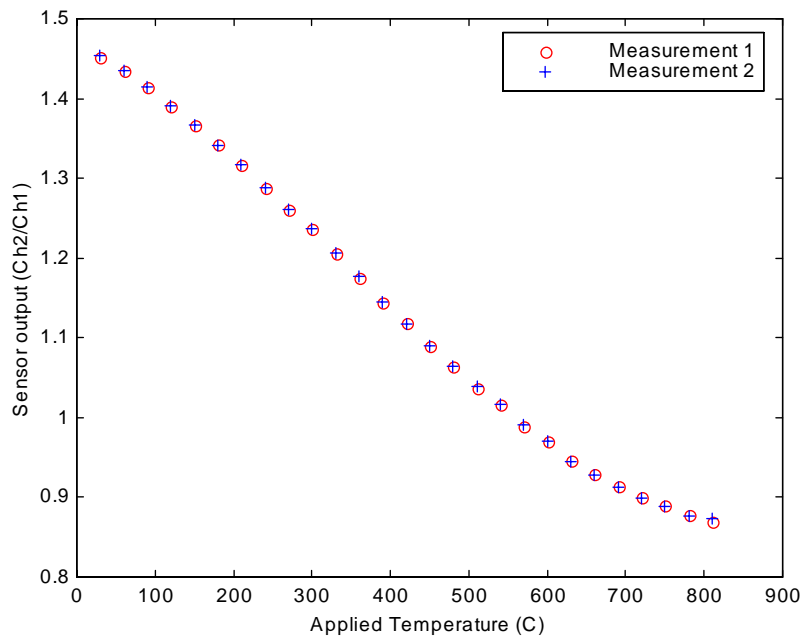


**Figure 6.18. Multimode SCIIB sensor temperature sensitivity test result**

As shown in Figure 6.18, the SCIIB system output was estimated to cover about 70% of the change from the peak to the valley of an interference fringe when the temperature changed from 30°C to 810°C. It was known that half of the interference fringe corresponded to a sensor cavity length change of a quarter of the central wavelength. Therefore, with the source central wavelength of 850 nm, the temperature sensitivity of the multimode sensor could be estimated by the following equation.

$$s_{t,m} = \frac{70\% \times \frac{1}{4} \times 850[\text{nm}]}{(810 - 30)[^\circ\text{C}] \times 0.7[\text{mm}]} = 2.7 \times 10^{-7} \left[ \frac{1}{^\circ\text{C}} \right] \quad (6-7)$$

Although the temperature sensitivity given in Eq. (6-7) is only an estimation, the result agrees with what the temperature model predicts. The experimental results indicate that the

multimode fiber-based sensor probe has a large temperature dependence compared to its linear operating range. This is mainly due to the large CTE of the fiber which results from the large quantity of dopants used to increase the core refractive index and fill the relatively large core. The large difference between the CTE of the fiber and that of the fused silica tube makes the multimode fiber-based sensor probe have a large temperature dependence. When the multimode fiber-based sensor is used for pressure measurement in harsh environments where the temperature variation could be large, the large temperature dependence can introduce an unacceptable error to the final result.

### 6.8.3.2 Singlemode fiber SCIIB sensor probe

Singlemode fibers have a smaller core diameter and refractive index difference compared to multimode fibers. The smaller amount of dopants in single-mode fibers makes the singlemode fiber have a CTE very close to that of fused silica, and hence less temperature dependence compared to the multimode fiber sensor. To determine the actual temperature sensitivity of the singlemode fiber-based sensor probe and also in hopes of finding an optimal design of the sensor probe to achieve zero temperature dependence, we fabricated five singlemode fiber sensors and measured their temperature sensitivity experimentally. The experiments were conducted using the same electrical furnace for the sensor annealing. Because the temperature sensitivity of the single-mode sensor is very low, it is almost impossible to increase the temperature high enough to cover one-half interference fringe as we did for the multimode fiber sensor. Whitelight interferometry was thus used to measure the sensor cavity length. Figure 6.19 shows the recorded sensor cavity lengths measured as

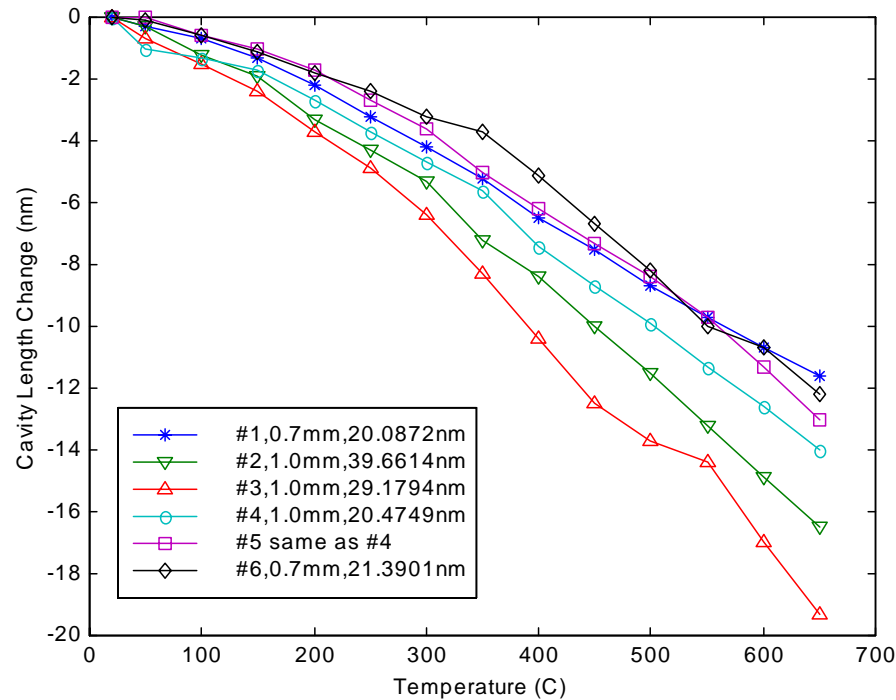


**Figure 6.19** Temperature sensitivity test results of singlemode sensor probes.

the temperature inside the furnace increased from room temperature up to 650°C in steps of 50°C. All the sensors showed a decrease in the cavity length as the temperature increased. Also, it was found that a shorter gauge length resulted in smaller temperature sensitivity.

Although efforts were made to find the exact CTEs of the fiber and the capillary tube by solving the linear equations formed by the experimental data, the results conflicted with each other. The reason was believed to be that the accuracy of the whitelight interferometry was not high enough compared to the required resolution. In order to provide meaningful data for the equation solving to find the actual CTEs, a more accurate method for displacement measurement must be used. Nevertheless, the experimental data did provide some information on the temperature dependence of the sensor. For example, a sensor with a gauge length of 0.7mm (corresponding to 4000psi pressure measurement range), and an initial cavity length from 20  $\mu\text{m}$  to 30  $\mu\text{m}$  will have a temperature sensitivity of 0.02nm/°C (or  $2.86 \times 10^{-8}/^\circ\text{C}$ ), which is an order of magnitude lower compared to that of the multimode fiber sensors.